SIMULATION-BASED OPTIMIZATION AND ARTIFICIAL INTELLIGENCE TECHNIQUES FOR MACROMECHANICAL AND MICROMECHANICAL CHARACTERIZATION OF SOFT BIOLOGICAL TISSUES

A Dissertation
Submitted to the Graduate Faculty
of the
North Dakota State University
of Agriculture and Applied Science

By

Mohammadreza Ramzanpour

In Partial Fulfillment of the Requirements
for the Degree of
DOCTOR OF PHILOSOPHY

Major Department:
Mechanical Engineering

April 2021

Fargo, North Dakota

North Dakota State University
Graduate School

Title

SIMULATION-BASED OPTIMIZATION AND ARTIFICIAL INTELLIGENCE TECHNIQUES FOR MACROMECHANICAL AND MICROMECHANICAL CHARACTERIZATION OF SOFT BIOLOGICAL TISSUES

By

Mohammadreza Ramzanpour

The Supervisory Committee certifies that this ***disquisition*** complies with North Dakota State University's regulations and meets the accepted standards for the degree of

DOCTOR OF PHILOSOPHY

SUPERVISORY COMMITTEE:

Dr. Ghodrat Karami
Chair

Dr. Mariusz Ziejewski

Dr. Chad Ulven

Dr. Kalpana S. Katti

Approved:

05/04/2021
Date

Dr. Alan Kallmeyer
Department Chair

ABSTRACT

Traumatic brain injury (TBI) is a serious health and socioeconomic issue which affects thousands of lives annually in the United States. Computational simulations play an important role in better understanding of the TBI and on how it happens. Having accurate material properties of the brain tissue and the elements of the brain will help with more accurate computational simulations. Material characterization is therefore the line on which lots of research have been conducted. In recent years, the emerge of data driven approaches has led to better and more accurate soft tissue characterization. In this dissertation, a metaheuristic search optimization method together with simulation-based optimization framework, and artificial intelligence-based approaches have been employed for macromechanical and micromechanical characterization of brain tissue. First, a constrained particle swarm optimization (C-PSO) technique has been established for soft tissue characterization that overcomes the shortcomings of the classical optimization methods. Through the application of the inherent constraints in the hyperelastic and visco-hyperelastic models, it became possible to reduce the time complexity of this optimization algorithm. Subsequently, the developed constrained optimization method was employed to create simulation-based optimization frameworks for characterizing the micro-level constituents of human brain white matter including axons and extracellular matrix using the hyperelastic and visco-hyperelastic constitutive models. This simulation-based optimization framework helps the researchers to go around the complexities involved with the experimental techniques on micro-level characterization of soft tissues. The final part of this dissertation is devoted to the development of the machine learning and deep learning techniques for classifying the tissue stiffness out of the finite element (FE) simulation results. Through the training of a regularized logistic regression and deep learning convolutional neural networks, it became possible to correctly predict more than 91% of the cases of tissues with high stiffness. The tissues with high stiffness are usually indicative of the pathology and hence are important from medical perspective. The outcome of this part of the work could be useful for qualitative description of the soft biological tissue stiffness and pathology diagnosis which can be used as an alternative to the inversion algorithms.

ACKNOWLEDGEMENTS

I want to express my gratitude toward Dr. Ghodrat Karami for his great helps during my education, his immense knowledge, kindness, and support which without them, the completion of this dissertation would not be possible.

Special thanks to Dr. Mariusz Ziejewski for his continuous support and kindness which was of a great help in continuation of my endeavors in my PhD degree.

I wish to thank Dr. Chad Ulven and Dr. Kalpana Katti for their time and contributions as committee members.

I appreciate the Department of Mechanical Engineering at North Dakota State University and Dr. Allan Kallmeyer for their support.

Thanks to the Department of Animal Science for providing the animal brain samples.

I am happy to acknowledge my friends and colleagues, Dr. Rahil Ashtari, Dr. Mohammad Hosseini-Farid, Dr. Mojtaba Ahmadi, Dr. Jamileh Shojaeiarani, Babak Jahani, and Amin Vedadi for their companionship and creating a good working atmosphere.

Last but not the least, I am grateful to my dear parents, dear sisters Dr. Maryam, Dr. Melika, and Neda and my lovely nephew Amirali for all their encouragements and supports.

DEDICATION

I am honored to dedicate this dissertation to my dear parents,

Esrafil Ramzanpour and Mahmonir Makani.

I love you and thank you for your unconditional love and support in all stages of my life!

TABLE OF CONTENTS

LIST OF TABLES

LIST OF FIGURES

1. INTRODUCTION

In this chapter, the ongoing research in TBI and the efforts for biomechanical modeling of this problem will be presented. In particular, the characterization of soft tissues which plays a vital role within the context of TBI simulation will be described. The dissertation objectives defined for addressing the issues in the field of soft tissue characterization will be explained and finally, the organization of the dissertation and its structure will be discussed.

1.1. Overview

Annually 1.5 million cases of traumatic brain injury (TBI) occur in the United States [7]. Just in year 2013, 56000 TBI related deaths were recorded in the United States which accounts for 2.2% of overall death statistics [8]. The annual indirect financial burden of TBI is estimated to be approximately 2.8 billion dollars [9]. All of this reiterate the importance of TBI and why it is needed to be studied. The emerging use of computational methods such as FE in simulation of TBI plays an important role in better understanding of TBI and how it happens. There are many factors contributing to the accuracy of the FE simulations, from which the following factors can be mentioned:

- Inclusion of different human head organs such as skull, cerebrospinal fluid (CSF), pia mater, brainstem, and brain tissue in the FE model.
- Geometrical implementation of the human head organs. Ideally, they must be very close to actual human anatomy.
- Inclusion of gender and age contributing factors to the TBI analysis and their implementation in the FE model.
- Material characterization and the right choice of constitutive model for different organs of the human head including brain tissue.

Each of the above items, has been a separate topic for research in which many efforts have been made to improve the FE simulations from that perspective. Mao et al. [10] used computed tomography and magnetic resonance imaging to develop an average male head model. Different

head organs such as cerebrum, cerebellum, brainstem, corpus callosum, ventricles, and thalamus were included in their developed human head FE model. Subsequently, they have used different criteria such as brain pressure [11,12], brain motion [13], and facial bone response [14] for validating their developed FE model by comparing 35 different simulations against experimental tests. In another work, Tse et al. [15], developed two sets of human head FE model with the one including the soft tissues (1.3M elements) and the another, excluding the soft tissues (0.4M elements). For the evaluation phase, they used intracranial pressure (ICP) and relative intracranial motion data of conducted experimental tests [11–13]. Linear elastic and linear viscoelastic constitutive models were used for description of different organs and soft tissues. Using of computed tomography and magnetic resonance imaging, they were able to provide subject-specific models.

For each of the organs included in the human head FE model, it is necessary to develop appropriate constitutive models and to use right material properties for them. While many of the organs (usually the non-soft ones) are modelled as linear elastic materials, certain components such as brain cannot be accurately described with the linear constitutive models. Brain is an ultra-soft tissue which exhibits large deformation under loading. Since the origin of the TBI can be traced back to the deformation in the brain at the time of the TBI-inducing incident, it is of the utmost importance to increase the accuracy of the mechanical behavior description of brain by finding the most precise constitutive parameters. This task can be challenging due to the high level of nonlinearity in those models including the hyperelastic and visco-hyperelastic models. Other than brain, these nonlinear models have been used for characterizing different organs of the head including pia mater [16], dura mater [17], brainstem [18], and cranial bone [19]. Numerous studies have been conducted for material characterization of brain tissue and researchers have attested on the complexity of brain characterization compared to other tissues [20–22]. The attempts on brain tissue characterization is not limited to the macro-level scale and studies have been performed down to the micro-level as well. Diffuse axonal injury (DAI) is a form of injury which is directly related to the micro-level constituents of the brain white matter and hence motivated the researchers to put a vast effort for micromechanical and multi-scale characterization of human brain tissue [23–25].

Besides the computational techniques, researchers use different experimental methods including, but not limited to, uniaxial loading, biaxial loading, and indentation tests. Another useful technique is the magnetic resonance elastography (MRE). Through the measurement of small vibra-

tions in the tissue, it is possible to calculate the stiffness of the tissue given that certain parameters of the tissue like density and Poisson's ratio is known. The vibration is either induced into the tissue through mechanical actuators or generated by natural phenomena like cardiac cycle or respiration. MRE provides physicians with a powerful tool for diagnosing the over-stiffed tissue which could help them in diagnosing potential pathologies.

1.2. Objectives

In this dissertation, it is first tried to identify the problems and the gaps in the field of brain tissue characterization and then coming up with approaches for attacking those problems.

As mentioned, the choice of constitutive model is important in the accuracy of the TBI FE simulations. For the soft tissues, and specially the brain, those constitutive models are usually highly nonlinear. Commonly, the material parameters of the tissues are found using experimental tests and subsequent fitting of them with their corresponding constitutive equations. Mostly in the literature, this task of curve fitting is done using classical optimization techniques, many of them being gradient based. These gradient-based optimization techniques are prone to yield the local minimum of the curve fitting optimization problem which in turn, could lead to misleading results. Moreover, while simulation-based optimization has been used for soft tissue characterization, to the author's best knowledge, no specific study has been done to improve their time complexity. These optimization techniques are commonly performed in the cases where the constitutive model and/or the simulation conditions make the analytical solution impossible. Usually, thousands of simulations are carried on for finding the right material parameters. Hence, the second part of this dissertation is aimed at developing a search optimization technique for finding the best material parameters in a most accurate way, and subsequently, coming up with strategies and approaches that could reduce the time complexity of it.

The problem of DAI in TBI-related injuries asks for a deep investigation on the micro-level constituents of the brain white matter including axons and extracellular matrix (ECM). The DAI happens when the axons are deformed and usually cut off during the incidents. DAI is the most common form of the TBI. Due to the difficulty in performing micro-level experimental tests, the researchers have widely exploited the computational FE techniques. Different loading scenarios with different constitutive models have been the topics of studies in this field. Noticing the gap

for time-dependent characterization of those micro-level constituents and lack of the load-agnostic characterization, led to the third and fourth part of this dissertation.

While MRE is a powerful tool at the physicians' disposal for finding the stiffness of soft biological tissues, the inversion algorithms used for generating the stiffness field map out of the displacement field could be challenging as certain material parameters (depending on the choice of constitutive model) are needed to be known such as density and Poisson's ratio. Usually, the average values are begin used for different patients and hence a room for error in the stiffness measurement should be anticipated. Moreover, the pathologic tissues usually exhibit higher stiffness compared to the healthy ones. Therefore, since in many cases the MRE is used for pathology detection, the exact value of the tissue stiffness is not vital to be known and the qualitative comparison of the stiffness could be sufficient for decision making. To resolve both mentioned problems, a data-driven modeling approach is developed by employing artificial intelligence (AI) techniques including machine learning and deep learning methods. In these approaches, data from numerous FE simulations are used to learn the stiffness of the model. The fifth part of this dissertation is focused on this study.

1.3. Dissertation structure

Based on what explained, the main content of this thesis can be structurally visualized in Figure 1.1. The main objectives of this dissertation are shown on the leftmost side of Figure 1.1 and their corresponding parts (chapters) of this dissertation are shown on the right side. The final part of this dissertation is focused on concluding the previous parts of the dissertation and providing some insights for possible future works.

The content of this dissertation is based on and adapted from the following published peer-reviewed journal papers and peer-reviewed conference proceeding papers:

- [25] Ramzanpour, Mohammadreza, Mohammad Hosseini-Farid, Jayse McLean, Mariusz Ziejewski, and Ghodrat Karami. "Visco-hyperelastic characterization of human brain white matter micro-level constituents in different strain rates." Medical & Biological Engineering & Computing 58, no. 9 (2020): 2107-2118. (Chapter 4)

- [26] Ramzanpour, Mohammadreza, Mohammad Hosseini-Farid, Mariusz Ziejewski, and Ghodrat Karami. "A constrained particle swarm optimization algorithm for hyperelastic and visco-hyperelastic characterization of soft biological tissues." International Journal for Com-

putational Methods in Engineering Science and Mechanics 21, no. 4 (2020): 169-184. (Chapter 2)

- [27] Ramzanpour, Mohammadreza, Mohammad Hosseini-Farid, Mariusz Ziejewski, and Ghodrat Karami. "Microstructural hyperelastic characterization of brain white matter in tension." In ASME International Mechanical Engineering Congress and Exposition, vol. 59407, p. V003T04A009. American Society of Mechanical Engineers, 2019. (Chapter 3)

- [28] Ramzanpour, Mohammadreza, Mohammad Hosseini-Farid, Mariusz Ziejewski, and Ghodrat Karami. "Particle swarm optimization method for hyperelastic characterization of soft tissues." In ASME International Mechanical Engineering Congress and Exposition, vol. 59469, p. V009T11A028. American Society of Mechanical Engineers, 2019. (Chapter 2)

- [29] Ramzanpour, Mohammadreza, Mohammad Hosseini-Farid, Jayse McLean, Mariusz Ziejewski, and Ghodrat Karami. "A Logistic Regression Analysis for Tissue Stiffness Categorization Through Magnetic Resonance Elastography." In ASME International Mechanical Engineering Congress and Exposition, vol. 84522, p. V005T05A043. American Society of Mechanical Engineers, 2020. (Chapter 5)

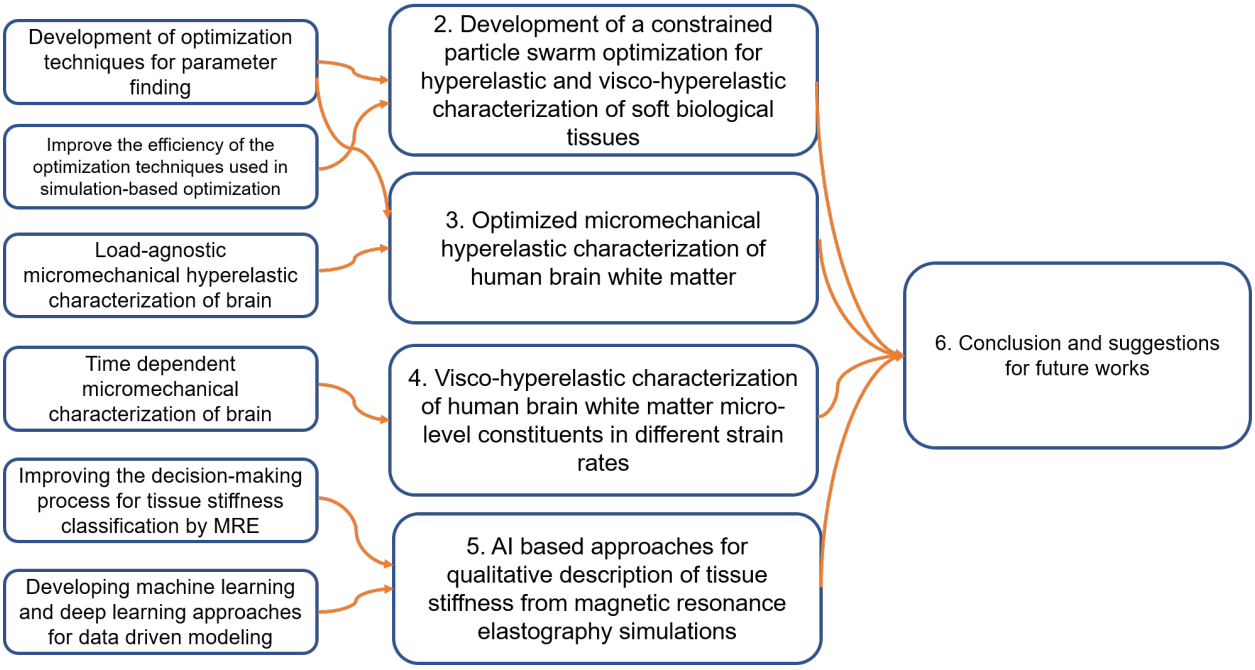

Figure 1.1. The structure of this dissertation. The objectives in the left are correlated to the chapters of this dissertation.

2. DEVELOPMENT OF A CONSTRAINED PARTICLE SWARM OPTIMIZATION FOR HYPERELASTIC AND VISCO-HYPERELASTIC CHARACTERIZATION OF SOFT BIOLOGICAL TISSUES

2.1. Introduction and literature review

Hyperelastic constitutive models are used for describing the behavior of the materials showing elastic response under very large deformation. These models are widely used for characterization of soft biological tissues including blood vessel [30,31], liver [32,33], and brain [34–36]. Among these tissues, the brain is one of the most important yet most complicated organ of the human body [20]. The ongoing research for characterizing the behavior of brain tissue is a fundamental step for increasing the accuracy of computational and numerical studies including finite element simulations which are used for a better understanding of traumatic brain injury (TBI) [37–41]. The most common methods for characterization of brain tissue can be categorized into direct in-vitro uniaxial and multiaxial testing, and in-vivo methods including MRE [42–44]. However, the mentioned in-vivo methods can be and have been performed under in-vitro conditions as well [45], the complexity and high cost of those methods remains as a barrier for their wide usage and hence, most of the studies employ the uniaxial or multiaxial testing for this purpose. Many of the conducted studies in the field of brain material characterization have used the uniaxial testing under different loading conditions of tension, compression, and shear [1, 28, 46]. Moreover, most of the soft biological tissues including brain, shows a time-dependent behavior [47–49]. The brain tissue exhibits a relaxing behavior i.e., the reduction in the stress of the tissue over the time when subjected to constant deformation. This time-dependent behavior of brain tissue has been widely modeled in the literature by the means of linear viscoelastic or nonlinear visco-hyperelastic constitutive models [1, 47, 50–53].

The material in this chapter was co-authored by Mohammadreza Ramzanpour, Mohammad Hosseini-Farid, Mariusz Ziejewski, and Ghodrat Karami. The content of this chapter was published in International Journal for Computational Methods in Engineering Science and Mechanics, 21(4), 169-184. Mohammadreza Ramzanpour was mainly responsible for experimental data collection, analysis, algorithm development, and the conclusions advanced here. The other co-authors helped in proof-reading the paper. Ghodrat Karami supervised the project.

Strain energy functions are used to interpret the experimental data for the use in the mathematical constitutive modeling and numerical finite element simulations. Numerous strain energy functions have been developed for this purpose and it is an active field of research, especially in biomaterial characterization [22, 54–56]. Some constitutive models and characterizations are developed based on the macro or micromechanical structure of a specific material [2, 57] and therefore, they are most appropriate for those kinds of materials. Moreover, based on the application and the conditions of testing, a specific material model or parameter may be observed to be more efficient and accurate for describing its behavior [58].

Upon the selection of the suitable strain energy function for the material, another important step is required and that is the search for material model parameters. Mostly in the literature, the iterative finite element-based optimization [27, 59–61], Levenberg-Marquardt algorithm (LMA) [62, 63], and trust region reflective algorithm (TRF) [64] have been used for finding the hyperelastic and visco-hyperelastic parameters. However, this problem can still be challenging due to the high nonlinearity of the involved constitutive models. Gradient based minimization algorithms like LMA can be fast on convergence, however on the downside, they are prone to get stuck in local minimum due to the bad initial guess which in some cases can lead to parameters highly deviated from the actual expected result. As later will be shown in this article, in some cases such as visco-hyperelastic models, these gradient based optimization algorithms are unable to do the curve fitting. To overcome all these hindrances, alternative optimization methods including metaheuristic search optimization methods can be useful in this regard. Moreover, these algorithms also known as black-box optimization methods are commonly used for iterative finite element-based optimization which are unavoidably time consuming [18, 65]. Based upon the desired accuracy and the complexity of the finite element model, several hundreds or thousands of simulations are required for completing the optimization procedure to obtain the material properties [66]. Hence, any effort to improve the efficiency of these optimization algorithms by reducing the required number of iterations for convergence, can be beneficial in decreasing the time complexity of the material characterization procedure.

In this part of the dissertation, the application of constrained particle swarm optimization (C-PSO) algorithm for deriving the hyperelastic and visco-hyperelastic parameters of the bovine brain tissue will be investigated. Since numerous studies have confirmed the effect of strain rate on

the material properties of the brain tissue [4,67–69], the uniaxial compression tests are conducted at different strain rates, so that the developed C-PSO algorithm can be checked against the variation of the mechanical response caused by the change in strain rate of deformation. Thereafter, a comparison is made with the results obtained by the gradient-based optimization methods. Finally, different modifications that can be applied on the C-PSO algorithm to find out the fastest and most efficient approach will be investigated.

2.2. Methodology

In this section, first, the process of performing experimental tests on the bovine brain tissue will be explained. Thereafter, different constitutive models which will be used for describing the mechanical response of the brain will be delineated. Finally, the C-PSO method will be explained and the appropriate optimization problem for finding the material parameters of the constitutive models will be established.

2.2.1. Unconfined compressive uniaxial tests on bovine brain tissue

Bovine brain samples were obtained from Animal Science Department at North Dakota State University few hours postmortem. The samples were maintained in phosphate-buffered saline (PBS) to avoid dehydration and consequent changes in the physical structure of brain samples. The brain samples were cut with cylindrical shaped surgical scalpels and the respective height and diameter of each sample were recorded as well. Great care was taken for the extraction of the samples regarding their orientation to eliminate the need for orientational dependency analysis of the brain material properties. To perform uniaxial unconfined compression test, the BOSE 3200 electro-force machine (BOSE Corporation, Bloomington MN, USA) was used. The upper and lower platens were lubricated with oil to minimize the friction of the samples with platens, therefore, satisfying the required conditions for the uniaxial unconfined compression loading. The test setup is shown in Figure 2.1.

The samples were subjected to approximately 30% deformation with the deformation speed of 1, 10, and 1000 mm/s, and then relaxed under constant deformation for the time of approximately 100 to 120 seconds. For each deformation speed, 10 samples were tested, and the average response was calculated for further analyses. The description of each of the test cases are presented in Table 2.1.

(a) (b) (c)

Figure 2.1. The steps for preparing the brain samples including (a) separating the right and left lobes, (b) cutting the samples with sharp cylindrical tool, and (c) placing the samples in the lubricated platens of the BOSE 3200 electro-force machine for unconfined compression tests.

Table 2.1. Unconfined uniaxial relaxation compression test specification and samples geometrical details.

Height	Diameter	#Samples	Deformation speed	Strain rate	Max strain	Relaxation time
10 mm	25 mm	10	1 mm/s	0.1 s^{-1}	-0.3	120 s
14 mm	25 mm	10	10 mm/s	0.7 s^{-1}	-0.3	110 s
14 mm	25 mm	10	100 mm/s	7 s^{-1}	-0.3	105 s

The sample relaxation data obtained from this experimental setup representing force and displacement of the sample for the strain rate of 0.1 s^{-1} is shown in Figure 2.2. As can be seen, first, the sample is deformed and compressed up to 3 mm corresponding to the nominal strain value of -0.3, and then the sample will be held at this displacement to be relaxed. In the relaxation phase, the induced force in the sample begins to reduce. The relaxation phase of the test must be interpreted in a time-dependent manner. The averaged time-force diagram of the relaxed phase of the test corresponding to the strain rate of 0.1 s^{-1} is shown in Figure 2.3. As it can be seen, due to the small change of force in the course of the time, and the high sensitivity of the load cell in the device, the data is noisy and therefore, appropriate smoothing methods should be applied to the data for noise reduction. Here, the Savitzky-Golay filter [70] with the degree of 3 and window length of 51, was used for the purpose of data smoothing. This filter is commonly used for the signal processing and filtering the data acquired from sensors [71].

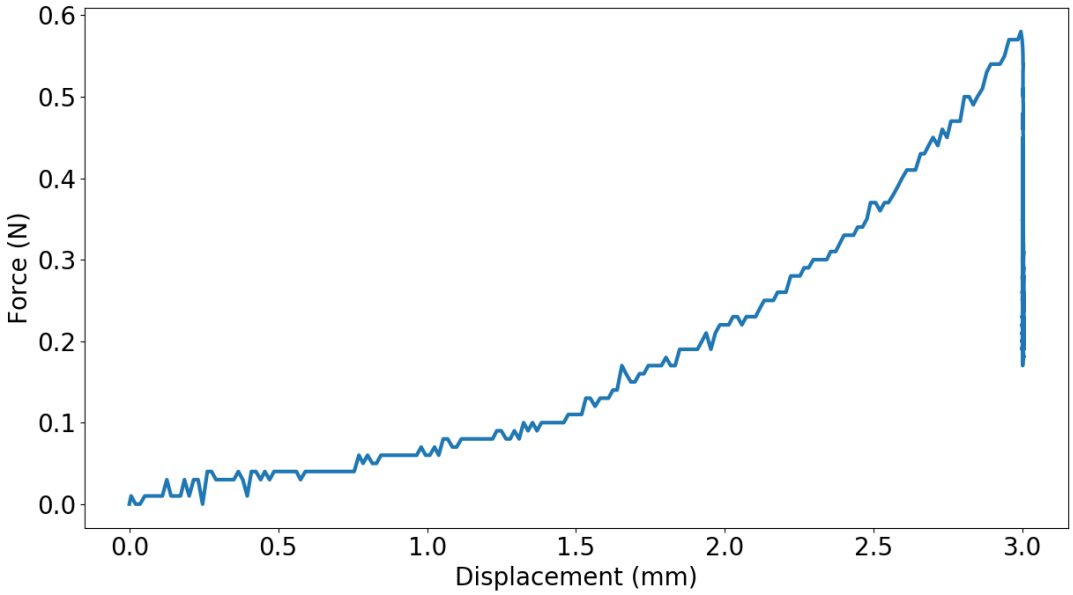

Figure 2.2. Sample relaxation test data for brain samples with the deformation speed of 1 mm/s corresponding to strain rate of 0.1 s^{-1}. The displacement will be held constant at 3 mm and the sample begins to relax thereafter.

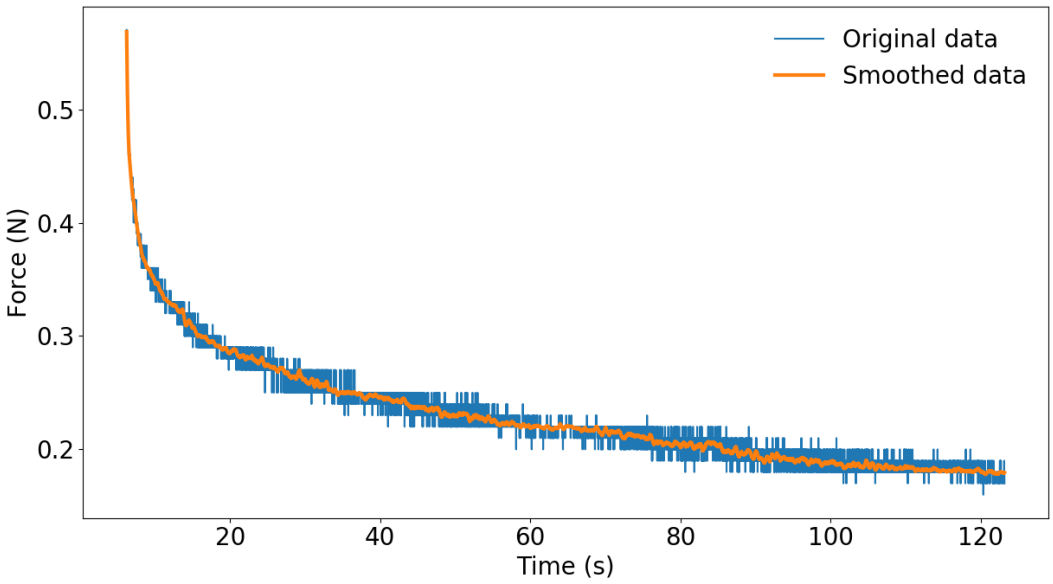

Figure 2.3. The time-force response of the brain sample in the relaxation phase of the test with the strain rate of 0.1 s^{-1}. The data is noisy as the relative change of force is small with respect to time.

2.2.2. Hyperelastic and visco-hyperelastic constitutive modeling

Different hyperelastic models are considered in this study for hyperelastic characterization of brain tissue. Neo-Hookean, Ogden, Mooney-Rivlin and Yeoh model can be named as hyperelastic

models among which Neo-Hookean model is the simplest one, mostly appropriate for characterization of rubber like solid materials [72] and is rarely used for soft biological tissues. Therefore, the Neo-Hookean model is just studied for checking the accuracy of the C-PSO and LMA methods.

The first step for constitutive hyperelastic modeling is to identify and formulate the deformation based on the loading mode. The deformation gradient depends on the loading mode being uniaxial, planar, or biaxial. As in our study, the experimental test is uniaxial unconfined compression, the deformation gradient can be written as the following:

$$F = \begin{bmatrix} \lambda & 0 & 0 \\ 0 & \frac{1}{\sqrt{\lambda}} & 0 \\ 0 & 0 & \frac{1}{\sqrt{\lambda}} \end{bmatrix} \tag{2.1}$$

In the above equation, F is the deformation gradient and $\lambda = 1 + \epsilon$ with ϵ standing for the nominal strain value. The λ is also known as the stretch which is commonly used in nonlinear constitutive modeling.

The Neo-Hookean model [73] for incompressible materials in uniaxial loading condition can be stated as the following:

$$\sigma = \mu \left(\lambda^2 - \frac{1}{\lambda} \right) \tag{2.2}$$

As can be speculated from equation (2.2), the only controlling parameter is μ, also known as the initial shear modulus which must be a positive value.

The Ogden hyperelastic model [74] is expressed based on the applied principal stretch values. The principal stress for the Ogden model is given by the following:

$$\sigma = \sum_{i=1}^{N} \frac{2\mu_i}{{\alpha_i}^2} \left({\lambda_1}^{\alpha_i} + {\lambda_2}^{\alpha_i} + {\lambda_3}^{\alpha_i} - 3 \right) \tag{2.3}$$

where N denotes the number of terms used in the Ogden model. $\lambda_i,\ (i = 1, 2, 3)$ refer to the principal stretch values, μ is the initial shear modulus, and α is the Ogden model parameter. Therefore, the explicit stress-stretch equation for Ogden model in the uniaxial loading condition will be stated as

the following:

$$\sigma = \sum_{i=1}^{N} \frac{2\mu_i}{\alpha_i} \left[\lambda^{\alpha_i} - \left(\frac{1}{\sqrt{\lambda}} \right)^{\alpha_i} \right] \tag{2.4}$$

Using the one-term Ogden model, equation (2.4) can be rewritten as the following:

$$\sigma = \frac{2\mu}{\alpha} \left(\lambda^{\alpha} - \lambda^{-\frac{\alpha}{2}} \right) \tag{2.5}$$

The one-term Ogden model has been shown to be very effective in hyperelastic characterization and has been shown to be dominant over other hyperelastic models specifically when needed to be calibrated for different loading modes [1].

Due to the elasticity assumption in hyperelastic models, it is vital to investigate the behavior of hyperelastic models in low strain values i.e., $\lambda \to 1$ or $\epsilon \to 0$. Limit analysis of the hyperelastic constitutive models in low strain values can be performed to check if any constraints are needed to be held in the equation or not. Performing the limit analysis of the Ogden one-term model stated in equation (2.5) for low strain values gives the following:

$$\lim_{\lambda \to 1} \frac{2\mu}{\alpha} \left(\lambda^{\alpha} - \lambda^{-\frac{\alpha}{2}} \right) = \frac{2\mu}{\alpha} \left(\frac{1}{2} \alpha \epsilon \right) = \mu \epsilon \tag{2.6}$$

For obtaining the equation (2.6), the following identity equation is used:

$$\lim_{\lambda \to 1} \lambda^{\alpha} = \lim_{\epsilon \to 0} (1 + \epsilon)^{\alpha} = 1 + \alpha \epsilon \tag{2.7}$$

For equation (2.6) to be valid, it is obvious that the following constraint must be imposed on the model:

$$\mu > 0 \tag{2.8}$$

Following the study of Ogden model in small strain values, it possible to find an educated guess of the initial shear modulus μ of the material. At small strains $\lambda \to 1$, the following equation holds:

$$\left(\frac{d\sigma}{d\lambda} \right)_{\lambda \to 1} = \left[\frac{2\mu}{\alpha} \left(\alpha \lambda^{\alpha - 1} + \frac{\alpha}{2} \lambda^{\frac{-\alpha}{2} - 1} \right) \right] = 3\mu \tag{2.9}$$

which suggest the gradient of the stress with respect to the stretch at the beginning of the deformation will be approximately three times greater than that of the initial shear modulus.

The Mooney-Rivlin is another hyperelastic constitutive model which is an extension of the Neo-Hookean model [75]. For the uniaxial loading condition, the stress-stretch equation can be written as the following:

$$\sigma = 2\left(\lambda^2 - \frac{1}{\lambda}\right)\left(c_{10} + \frac{c_{01}}{\lambda}\right) \tag{2.10}$$

The limit analysis of the Mooney-Rivlin model stated in the above equation for small strain values gives the following result:

$$\lim_{\lambda\to 1}\sigma = \lim_{\lambda\to 1}\left[2\left(\lambda^3 - 1\right)\left(c_{10} + c_{01}\right)\right] = \lim_{\varepsilon\to 0}\left[6\left(c_{10} + c_{01}\right)\varepsilon\right] \tag{2.11}$$

To make the above equation compatible with the linear elasticity, the term $6\left(c_{10} + c_{01}\right)$ must give an approximate measure of the Young's modulus which therefore, results in the following constraint:

$$c_{10} + c_{01} > 0 \tag{2.12}$$

Moreover, another constraint can be extracted from the Mooney-Rivlin model based on the Drucker stability criterion. Drucker stability criterion [76] states that irrespective of the material deformation, the internal energy must increase, formulated as the following for the uniaxial loading:

$$d\sigma.d\epsilon > 0 \tag{2.13}$$

The equation (2.13) states that the sign of $d\sigma$ is the same as the sign of $d\epsilon$. As $d\lambda$ have the same sign as $d\epsilon$, the equation (2.13) can be justified to be equivalent of $d\sigma/d\lambda > 0$. Therefore, applying Drucker stability criterion on equation (2.10), deducts the following:

$$\frac{d\sigma}{d\lambda} = 2\left(2\lambda + \frac{1}{\lambda^2}\right)\left(\frac{-c_{01}}{\lambda^2}\right) > 0 \tag{2.14}$$

Looking into the above equation, the only variable involved in the Drucker stability of the Mooney-Rivlin model is the c_{01} parameter. Knowing that always $\lambda > 0$ concludes the following:

$$c_{01} < 0 \tag{2.15}$$

Equations (2.12) and (2.15) are the constraints that can be applied for Mooney-Rivlin characterization, however, it can be shown that one of the constraints, equation (2.12) is guaranteed to be satisfied, given the right experimental data is provided in the optimization process for curve fitting.

The Yeoh hyperelastic model [77] is defined based on the Helmholtz free energy. While this model is more accurate compared to the Neo-Hookean model, it avoids some of the stability issues encountered with Mooney-Rivlin model. The uniaxial stress for Yeoh model is described as:

$$\sigma = 2\left[c_{10} + 2c_{20}(I_1 - 3) + 3c_{30}\left(I_1 - 3\right)^2\right]\left(\lambda^2 - \frac{1}{\lambda}\right) \tag{2.16}$$

where I_1 is the first stretch invariant and from equation (2.1), can be found to be $I_1 = \lambda + 2/\sqrt{\lambda}$. Again, performing limit analysis for low strain values leads us to the following result:

$$\lim_{\lambda \to 1}\left(I_1 - 3\right) = \lim_{\lambda \to 1}\left(\frac{\lambda^{1.5} + 2}{\lambda^{0.5}} - 3\right) = \lim_{\epsilon \to 0}\frac{3}{4}\epsilon^2 > 0 \tag{2.17}$$

From the above equation, in low strain values, the Yeoh model dilutes down to the Neo-Hookean model and therefore, the following constraint must be imposed on the model:

$$c_{10} > 0 \tag{2.18}$$

As a matter of fact, the stability of Yeoh model is guaranteed if $c_{i0} > 0 \;\; (i = 1, 2, 3)$. However, since negative c_{20} value will result in better fitting and better capturing of nonlinearity of the mechanical response, it is a good practice to reduce the absolute value of c_{20} and increase the absolute value of c_{10} [78].

Soft materials such as brain, exhibit a time varying decaying stress being held under constant deformation. This phenomenon can be seen in Figure 3. For the time-dependent modeling of relaxation tests, the most common method employed in the literature is the use of expansion Prony

series parameters. Miller et al. [52] proposed the following strain energy function for time-dependent modeling of soft biological tissues by using the convolution integral based on the Ogden hyperelastic strain energy function:

$$W = \frac{2}{\alpha^2} \int_0^t \left[\mu(t-\tau) \frac{d}{d\tau} \left({\lambda_1}^\alpha + {\lambda_2}^\alpha + {\lambda_3}^\alpha - 3 \right) \right] d\tau \tag{2.19}$$

Where t is the time, α is the Ogden model parameter, and μ denotes the relaxed shear modulus calculated based on the following equation:

$$\mu = \mu_0 \left[1 - \sum_{i=1}^{n} q_i \left(1 - \exp(-t/\tau_i) \right) \right] \tag{2.20}$$

which μ_0 is the instantaneous shear modulus, q_i is the relaxation coefficient, and τ_i is the characteristic time. The quantity n denotes the number of terms to be used in the Prony series. While using more terms, results in better fitting and more accurate characterization, it adds to the complexity of the model. Usually, two terms should be enough for good characterization of relaxation tests.

The equation (2.20) is highly non-linear and finding the coefficients q and τ for fitting the experimental data is a challenging task. Moreover, the following relations must be held between the coefficients:

$$\sum_{i=1}^{n} q_i < 1 \tag{2.21}$$

$$\tau_i - \tau_j < 0 \quad , \quad \text{for each } i < j \tag{2.22}$$

The above constraint in equation (2.22) can be written in the following form as well:

$$\tau_i - \tau_{i+1} < 0 \ , \quad i = 1, 2, ..., n-1 \tag{2.23}$$

Based on the number of terms used in the Prony series, either of equations (2.22) or (2.23) may be more convenient to be used in the constrained optimization problem.

While stress values can be measured in different forms, in this part of the study, the first Piola-Kirchhoff stress is employed which uses the measure of force in deformed state (current) and

the stretch is calculated based on the initial configuration of the brain samples. The height and diameter of the brain samples are recorded before the tests which will be used for calculating their reference configuration area. The height and diameter of brain samples were recorded to be 10 mm and 25 mm, respectively.

2.2.3. Constrained optimization and curve fitting

Every constrained optimization problem can be formulated as the following:

$$\min_{x} \ f(x), \ x \subseteq \mathbb{R}^n \tag{2.24}$$

where $f(x)$ is the objective function, and x is a solution to the problem which is a vector defined in the $\mathbb{R}^n$ space with the n denoting the number of variables involved in the problem. The optimization process may be constrained with one or multiple linear or nonlinear inequality constraints stated as the following:

$$g_i(x) \leq 0 \quad i = 1, 2, ..., m \tag{2.25}$$

where m denotes the number of constraints imposed on the problem. It should be noted that the constraints in the form of $g(x) \geq 0$ can be stated as $-g(x) \leq 0$. Moreover, the equality constraints such as $g(x) = 0$ can be stated as two inequality constraints of $g(x) \geq 0$ and $g(x) \leq 0$. These two inequality constraints can be again stated and reformulated into equation (2.25). Therefore, every constrained optimization problem can be structured in the form of equations (2.24) and (2.25).

In the constrained optimization problems, the search space can be divided into two subspaces including constraint-satisfying and constraint-unsatisfying subdomains. The constraint-satisfying domain satisfies all the imposed constraints on the problem while the constraint-unsatisfying subdomain violates one or multiple stated constraints. The penalty function approach assigns a penalty to the potential solution vectors if the constraint is not satisfied. By defining the following cost function, our original constrained optimization problem can be unraveled by solving series of unconstrained optimization problem [79]:

$$J(x) = f(x) + h(k)H(x) \tag{2.26}$$

where $f(x)$ is the original optimization objective function, $h(k)$ is the dynamic penalty coefficient dependent on the iteration number k of the solution method, and $H(x)$ is the constraint violation value. In this paper the $h(k) = k\sqrt{k}$ is assigned for the dynamic penalty coefficient. The constraint violation value can be defined as the following:

$$H(x) = \sum_{i=1}^{m} \varphi_i(x)^2 \tag{2.27}$$

where $\varphi(x)$ can be defined as the following:

$$\varphi_i(x) = \max\left[0,\, g_i(x)\right] \tag{2.28}$$

Up to this point, the solution strategy of the optimization problem is completely defined and formulated . The curve-fitting problem can be converted into a least square optimization problem. Supposedly, there are x_{data} and y_{data} values consisting of N points and it is desired to fit them into a function $\psi(x)$. The optimization problem for curve fitting can be defined as the following:

$$\min_{args} f(\text{args}) = \frac{1}{N} \sum_{i=1}^{N} \left[\psi(\text{args}, x_{\text{data},\,i}) - y_{\text{data},\,i}\right]^2 \tag{2.29}$$

Different equality and inequality constraints can be imposed on equation (2.29) as well. The variable *args* refers to the arguments (coefficients) of the constitutive model. The quantities x and y are independent and dependent variables where in our analysis, and they could stand for the stretch -stress for hyperelastic and time-stress quantities for the visco-hyperelastic models, respectively.

2.2.4. Particle swarm optimization

The particle swarm optimization (PSO) algorithm tries to imitate the social behavior of human beings or groups of insects or birds called swarm. As an analogy, every action of human beings are influenced by two main factors, first, our cognitive understanding which is mostly based on our past experience and second, social communication meaning that humans are inclined to do the actions experienced by others which have produced the best results. PSO in n-variable optimization problem or the $\mathbb{R}^n$ search space, assigns several particles (agents) randomly assigned in the n dimensional space of the problem. Moreover, each particle has its own initial random velocity,

which will project its movement in the swarm evolution. Each particle location and velocity are shown by x_p and v_p, respectively which represent the state of the particles. Each particle changes its location and velocity based on the best state it has seen and the global best state that the whole swarm has experienced depending on the define topology of the algorithm. It should be noted that the global best state uses the "global" topology by considering all the particles. In this part, the hybrid weighted and constricted PSO formulated as the following is used:

$$v_i^{k+1} = \chi \left(\omega_k v_i^k + c_1 r_1 (x_{*i}^k - x_i^k) + c_2 r_2 (x_g^k - x_i^k) \right) \tag{2.30}$$

$$x_i^{k+1} = v_i^{k+1} + x_i^k \tag{2.31}$$

where k denotes the iteration number of the algorithm, x_{*i} and x_g stands for the best position experienced by the particle i and the best global position experienced by the whole swarm, respectively. c_1 and c_2 represents the cognitive and social coefficients of the algorithm which balances the movements of the particles based on their personal best seen position and global best experienced one. r_1 and r_2 are uniformly generated random numbers between 0 and 1.

The equation (30) takes advantage of both constricted PSO and weighted PSO. The constriction factor χ relaxes the velocity change of each particle to avoid the possible divergence. The constriction factor is suggested to be found from the following equation [80]:

$$\chi = \frac{2}{\left| 2 - c - \sqrt{c^2 - 4c} \right|} \tag{2.32}$$

where $c = c_1 + c_2 > 4$. In most of the conducted studies, it has been suggested to use $c_1 = c_2 = 2.05$ which the constriction factor ends up being $\chi = 0.729$ [81]. Using the constriction factor enables us to ignore the assignment of velocity threshold on the particles. The inertial weight is used for controlling the velocity of particles based on the velocity of previous iterations. The adjustment of inertia weight can lead to better global exploration or local exploration of the swarm. Higher inertia weight allows for sharper changes of the velocity, therefore, leading to higher global discovery ability while lower inertia weight is conducive to better local search. As a result, it is rational to improve global search ability of the swarm at the initial iterations of the PSO by setting high inertia weight

ω, while decreasing it gradually since the PSO hopefully reaches closer to the convergence in higher iteration numbers. Therefore, a common way of setting the inertia weight is to vary it based on the iteration number k as the following [82]:

$$\omega_k = \omega_{\max} - (\omega_{\max} - \omega_{\min}) \frac{k}{k_{\max}} \tag{2.33}$$

which $k_{\max}$ stands for the maximum number of iterations, $\omega_{\max}$ and $\omega_{\min}$ represents the maximum and minimum inertia weight coinciding with the first and last iterations of the PSO. $\omega_{\max}$ and $\omega_{\min}$ can be tuned specifically for each problem and in this study, we have set $\omega_{\max}$ and $\omega_{\min}$ equal to 1.2 and 0.1, respectively.

2.3. Results and discussion

In this section, the developed C-PSO algorithm will be used for hyperelastic and visco-hyperelastic characterization of bovine brain tissues based on the experimental tests. The constraints of the hyperelastic and visco-hyperelastic model identified in the previous section will be used as constraints in C-PSO algorithm. Thereafter, the obtained results of C-PSO will be compared to that of the traditional LMA and TRF for hyperelastic and visco-hyperelastic models, respectively. The "curve_fit" function from "scipy.optimize" package [83] in Python is used for curve fitting with LMA and TRF methods.

2.3.1. Hyperelastic curve fitting

The unconfined compression relaxation tests were done for different strain rates of 0.1, 0.7, and 7 s^{-1} to see its effect on the material properties of the brain tissue and more importantly, check the performance of the optimization algorithm in these different cases. The averaged ramp part of the relaxation tests visualized in terms of stretch-stress as shown in Figure 4, are used for hyperelastic characterization of bovine brain in different strain rates. The nominal stress is used for calculating the induced stress in samples.

The data shown in Figure 2.4 for different strain rates are fitted to the hyperelastic constitutive models by LMA and C-PSO methods. The number of particles in C-PSO method were set to be 10 times of the number of coefficients of each hyperelastic model which will be 20, 20, and 30 particles for Ogden, Mooney-Rivlin and Yeoh models, respectively and maximum number of iterations were set as 100. The lower and upper bound of all the coefficients were set in the

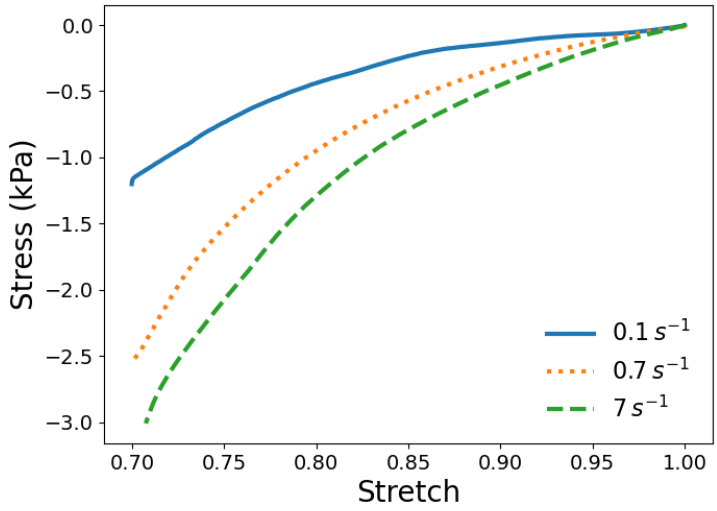

Figure 2.4. The ramp phase of the unconfined compression test on bovine brain sample at three different strain rates of 0.1, 0.7, and 7 s^{-1}. The data is smoothed with Savitzky-Golay filter.

Table 2.2. The obtained hyperelastic material properties by LMA and C-PSO methods for the strain rate of 0.1 s^{-1}. R^2 denotes the coefficient of determination serving as a measure of accuracy for the fitted data.

	Ogden	Mooney-Rivlin	Yeoh	Neo-Hookean
LMA	$\mu = 0.3489$ kPa $\alpha = -7.1094$ $R^2 = 99.72\%$	$c_{10} = 1.3190$ kPa $c_{01} = -1.2747$ kPa $R^2 = 99.54\%$	$c_{10} = 0.1786$ kPa $c_{20} = 2.4941$ kPa $c_{30} = 0.0118$ kPa $R^2 = 99.89\%$	$\mu = 0.8745$ kPa $R^2 = 83.78\%$
C-PSO	$\mu = 0.3489$ kPa $\alpha = -7.1094$ $R^2 = 99.72\%$	$c_{10} = 1.3190$ kPa $c_{01} = -1.2747$ kPa $R^2 = 99.54\%$	$c_{10} = 0.1933$ kPa $c_{20} = 2.1116$ kPa $c_{30} = 2.5149$ kPa $R^2 = 99.87\%$	$\mu = 0.8745$ kPa $R^2 = 83.78\%$

range of -100 to 100. For the LMA method, the initial guess for all the hyperelastic models and all the coefficients were assigned as 0.1. The summary of the obtained results is presented in Table 2, Table 3, and Table 4. As it can be seen, with the increase in the strain rate of the deformation, the bovine brain tissue shows stiffer response which in turn leads to the higher shear modulus in its hyperelastic characterization. The final resultant nominal stress for the strain rates of 0.7, and 7 s^{-1} are approximately 2 and 2.5 times greater than that of the $0.1s^{-1}$ strain rate, respectively. To avoid redundancy in data presentation, the fitted data with the obtained parameters are shown only for the strain rates of 0.1, and 7 s^{-1} in Figure 5 and Figure 6. As can be seen, the acquired hyperelastic parameters for Ogden and Mooney-Rivlin model through C-PSO method is the same as those of LMA method and moreover, the high coefficient of determination shows good accuracy

Table 2.3. The obtained hyperelastic material properties by LMA and C-PSO methods for the strain rate of 0.7 s^{-1}. R^2 denotes the coefficient of determination serving as a measure of accuracy for the fitted data.

	Ogden	Mooney-Rivlin	Yeoh	Neo-Hookean
LMA	$\mu = 0.7836$ kPa $\alpha = -6.8127$ $R^2 = 99.97\%$	$c_{10} = 2.5869$ kPa $c_{01} = -2.4224$ kPa $R^2 = 99.55\%$	$c_{10} = 0.4687$ kPa $c_{20} = 3.6660$ kPa $c_{30} = 9.2159$ kPa $R^2 = 99.96\%$	$\mu = 1.8624$ kPa $R^2 = 86.11\%$
C-PSO	$\mu = 0.7836$ kPa $\alpha = -6.8128$ $R^2 = 99.97\%$	$c_{10} = 2.5869$ kPa $c_{01} = -2.4224$ kPa $R^2 = 99.55\%$	$c_{10} = 0.4251$ kPa $c_{20} = 4.8298$ kPa $c_{30} = 1.4005$ kPa $R^2 = 99.93\%$	$\mu = 1.8624$ kPa $R^2 = 86.11\%$

Table 2.4. The obtained hyperelastic material properties by LMA and C-PSO methods for the strain rate of 7 s^{-1}. R^2 denotes the coefficient of determination serving as a measure of accuracy for the fitted data.

	Ogden	Mooney-Rivlin	Yeoh	Neo-Hookean
LMA	$\mu = 1.1822$ kPa $\alpha = -5.9725$ $R^2 = 99.97\%$	$c_{10} = 2.9894$ kPa $c_{01} = -2.6397$ kPa $R^2 = 99.87\%$	$c_{10} = 0.6349$ kPa $c_{20} = 6.1608$ kPa $c_{30} = -3.0706$ kPa $R^2 = 99.98\%$	$\mu = 2.5026$ kPa $R^2 = 90.39\%$
C-PSO	$\mu = 1.1822$ kPa $\alpha = -5.9725$ $R^2 = 99.97\%$	$c_{10} = 2.9835$ kPa $c_{01} = -2.6316$ kPa $R^2 = 99.53\%$	$c_{10} = 0.6437$ kPa $c_{20} = 5.9179$ kPa $c_{30} = -1.3934$ kPa $R^2 = 99.98\%$	$\mu = 2.5026$ kPa $R^2 = 90.39\%$

of the fitted results. The obtained shear modulus through LMA and C-PSO for the Neo-Hookean model is similar as well, but it does not give a good fit to the data as the low coefficient of determination and the illustration in Figure 2.5 and Figure 2.6 suggest. The inaccuracy of the Neo-Hookean model was expected since it only has one tunable parameter, and it is not appropriate for soft biological tissues where high nonlinearity is associated with. However, it can be easily verified that the obtained response by C-PSO and LMA method is the global minimum of the problem and no better solution can be acquired. Looking into the Yeoh model, the parameters found with these two algorithms exhibit a high value of R^2, but the parameters are clearly far from each other and the LMA algorithm slightly performs better as the higher coefficient of determination suggest.

The other point that should be mentioned is the accuracy of the LMA results while this method does not consider the constraints of hyperelastic models stated in equations (1.8), (1.12), and (1.15). Looking into the constraints and the hyperelastic constitutive equations, it can be

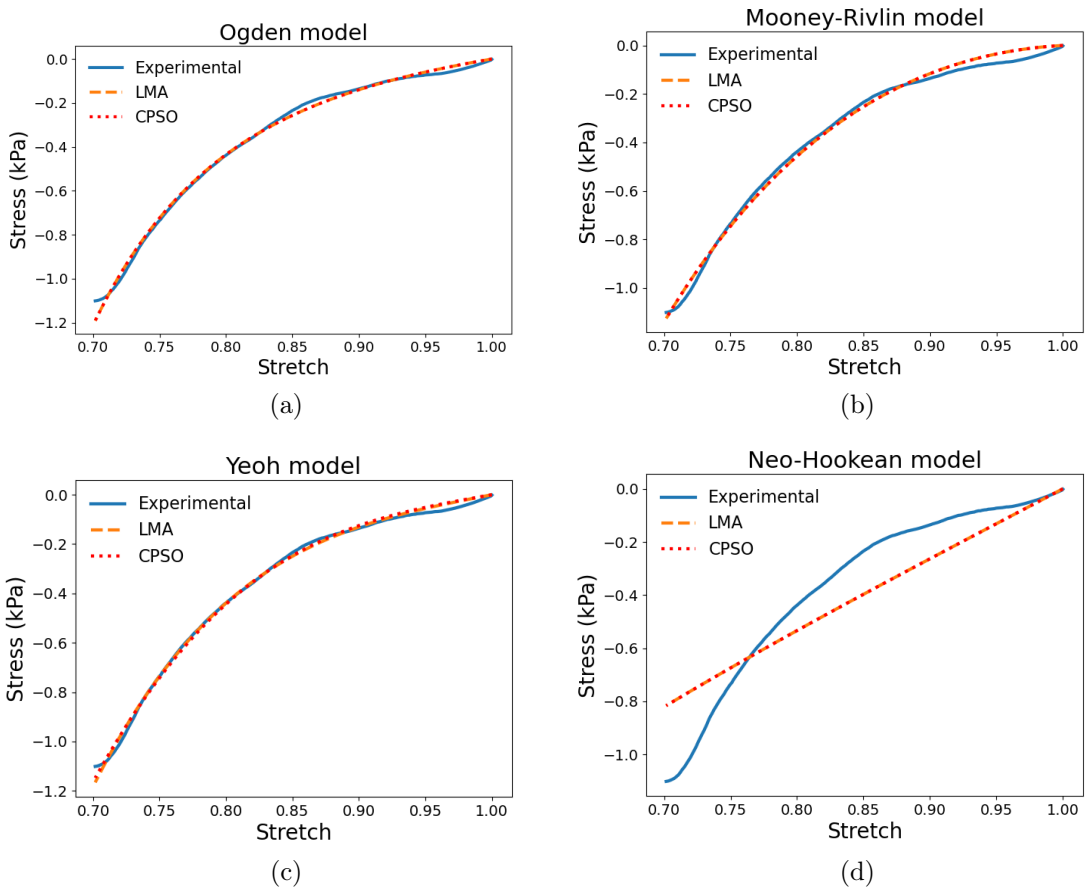

Figure 2.5. The visualized representation of fitted hyperelastic models into experimental data, including (a) Ogden, (b) Mooney-Rivlin, (c) Yeoh, and (d) Neo-Hookean model for the strain rate of 0.1 s^{-1}.

perceived that all those constraints are in accordance with the respective hyperelastic models. This comes from the fact that for the uniaxial test, the resultant stress will be positive for positive strain values and negative for negative strain values. Therefore, for the case of compression where $\lambda < 1$, the term $\lambda^2 - 1/\lambda$ in the Mooney-Rivlin model becomes negative. This implies that the other term which is $c_{10} + (c_{01}/\lambda)$ must be positive which is in total accordance with the constraint of the model stated in equation (1.12), since λ is always positive. Same reasoning can be justified for the constraints (1.8) and (1.15) of the Ogden and Yeoh models. Therefore, the unconstrained optimization will give the same result as that of the constrained optimization. However, in some situation, the LMA is observed to be highly dependent to initial guess and may not give appropriate result [28]. To discuss further, as an example, if the Ogden hyperelastic model with the parameters $\mu = 0.61\,kPa$ and $\alpha = -30.5$ is used to create a stress-stretch data in the stretch range of 1 to 1.1,

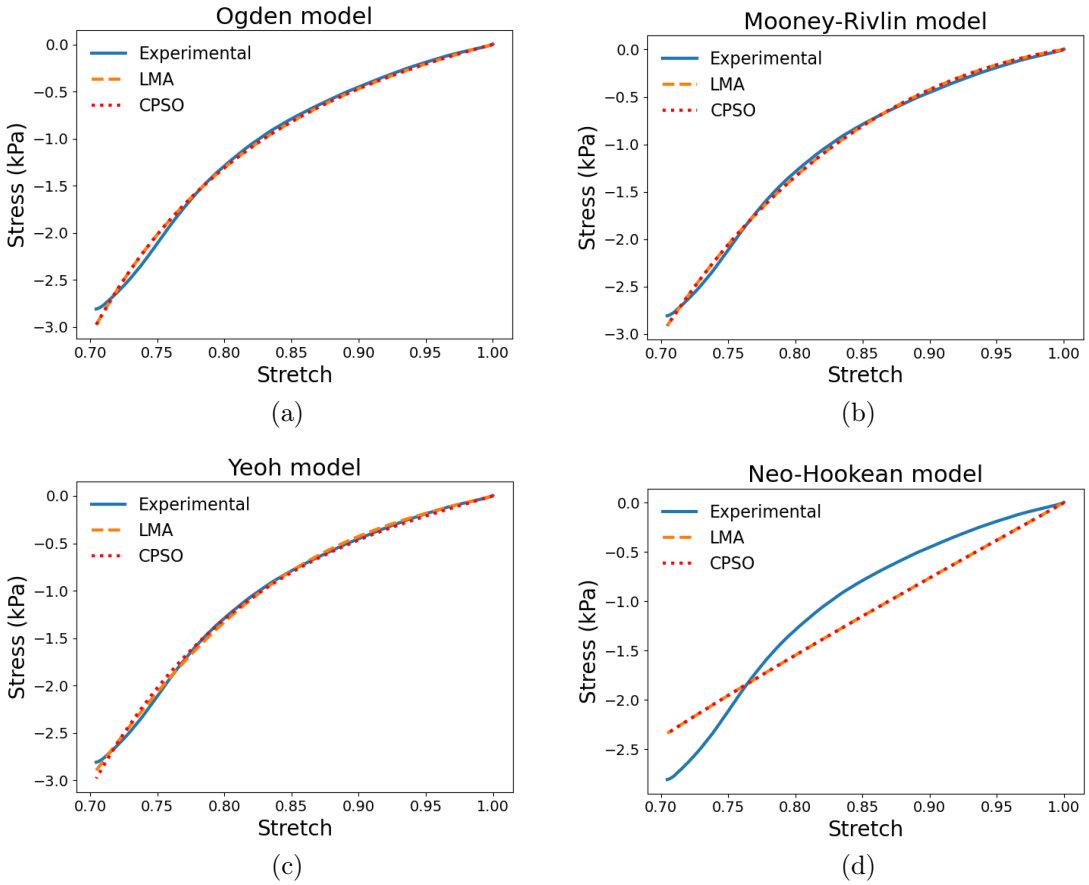

Figure 2.6. The visualized representation of fitted hyperelastic models into experimental data, including (a) Ogden, (b) Mooney-Rivlin, (c) Yeoh, and (d) Neo-Hookean model for the strain rate of 7 s^{-1}.

an artificial data set can be generated. These parameters correspond to the mechanical response of corona radiata in tension as reported by Budday et al. [1]. Now, if an attempt is made to find the parameters of Ogden model by fitting it to the artificially created data, the result will be completely different compared to what originally used for creating the dataset, as can be seen in Figure 2.7. The result obtained by LMA is found by using an initial guess of $\mu = 0.1\,kPa$ and $\alpha = 0.1$. While the LMA is giving a good fit to the dataset with the accuracy of $R^2 = 99.8\%$, the found Ogden parameters are clearly far from the original parameters used for generating the dataset and consequently does not return the global optimum point of the optimization problem .

Figure 2.8 shows the contour plot of the average square error of curve fitting to the Ogden model with respect to parameters μ and α fitted to the mentioned artificial dataset. As can be seen, there is a relatively wide range in the center of the domain wherein all the points (including

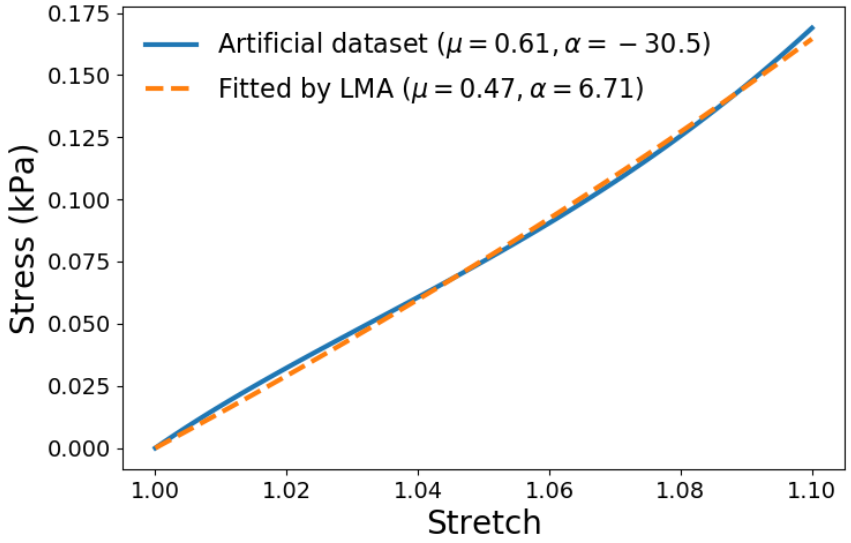

Figure 2.7. The performance of LMA method for curve fitting of the Ogden model to the artificially created dataset corresponding to the mechanical response of corona radiata in tension [1]. Opposed to our expectation, the LMA does not return the same parameters as those used for creating the artificial dataset.

the one obtained with LMA) show small error of less than 0.0015. Therefore, parameters μ and α can change in a big range while maintaining low error.

With all said, knowing the constraints of the problem and consequently, the feasible subspace of the model parameters i.e., the subdomain where all the constraints of the optimization problem are satisfied, the C-PSO algorithm can be modified to increase its efficiency. To demonstrate this, different C-PSO techniques associated with different convergence criteria are studied here. Three different convergence criteria for C-PSO including the following are proposed and studied:

- Stagnation of the best global function evaluation (SF): The solution is converged if the fitness (value) of the best particle changes within a set tolerance in a specified number of iterations.
- Stagnation of the best global position (SP): The convergence is met when the position of the best particle remains unchanged within a small tolerance bound, for some number of iterations.
- Proximity radius of the swarm (PR): In this criterion, the convergence of the solution is determined with respect to the whole swarm and opposed to the other criteria, it is not only dependent to the best particle of the swarm. The convergence radius of the swarm can be defined as the average distance of the particles from the best particle. The distance can be

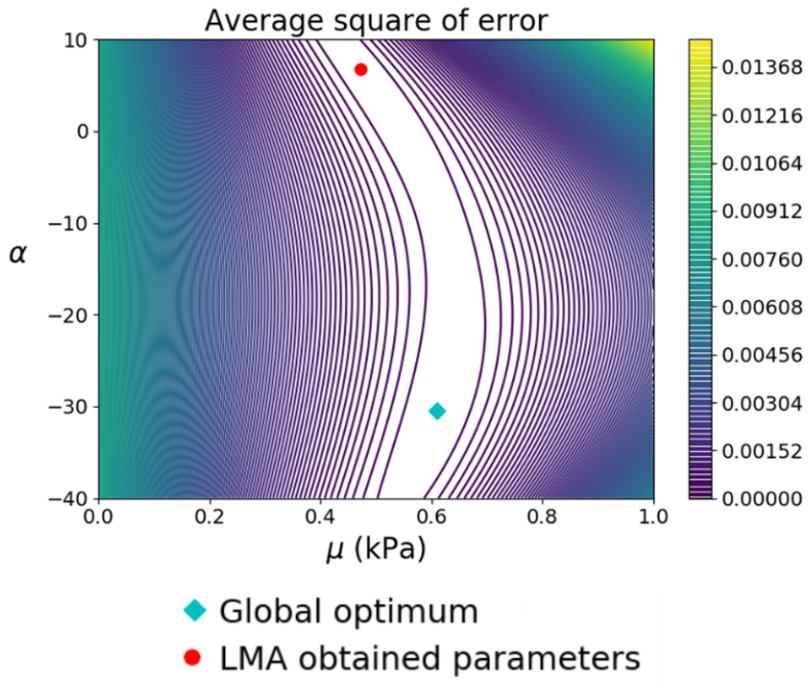

Figure 2.8. The contour plot of the average square error of the curve fitting to the Ogden model with respect to the parameters μ and α. Curve fitting is performed on the artificial dataset generated with parameters of $\mu = 0.61$ kPa and $\alpha = -30.5$ shown in Figure 2.7.

defined using the Frobenius norm of the position. This convergence criterion is visualized for a two-dimensional case in Figure 2.9 and formulated in equations (2.34) and (2.35).

$$r_i = \|x_i - x_g\|_2 \tag{2.34}$$

$$r_{avg} = \frac{1}{N}\left(\sum_{i=1}^{N} r_i\right) \tag{2.35}$$

In equations 2.34 and 2.35, r_i and r_{avg} refer to the distance of particle i and the average distance of the particles from the global best particle, respectively. N denotes the total number of particles in the swarm. The convergence is met when the average radius r_avg becomes less than a fraction of the solution domain radius i.e., the following condition:

$$r_{avg} \leq tol.\|(D_1,\, D_2,\, ...,\, D_i)\|_2 \tag{2.36}$$

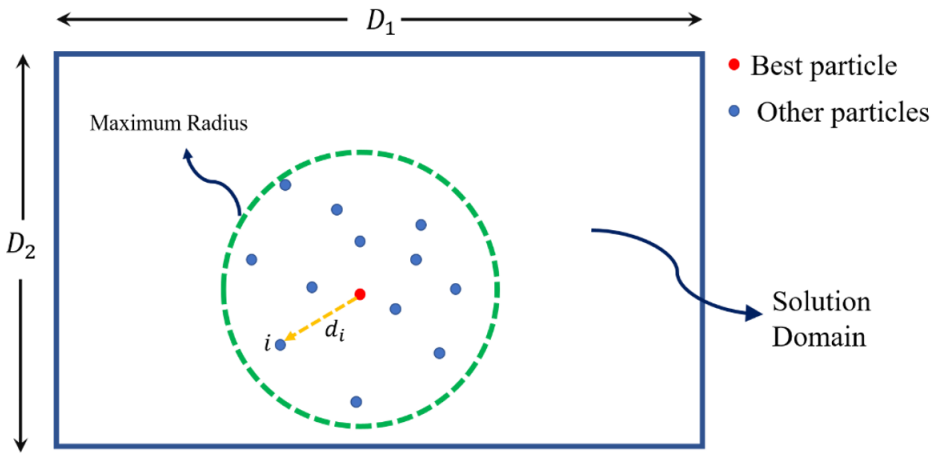

Figure 2.9. The convergence radius of the particles in PSO algorithm. The distance of each particle with respect to the best particle is calculated for finding their average distance to the best positioned particle.

where tol is a small number as a tolerance and D_i represents the length of i^{th} variable (dimension) in the solution domain and the $\|\|_2$ operator stands for the second norm of the vector.

Additionally, three different strategies will be used for solving the optimization problem of the curve fitting with respect to the constraints of the problem.

- Unconstrained (UC-PSO): The problem will be solved without applying any constraints.
- Constrained (C-PSO): The constraints of the problem will be applied to the PSO by using penalty function for constraint violation.
- Constrained with feasible initial swarm (CF-PSO): Besides applying the constraints of the problem, the initial swarm population will be created randomly, yet in a way that all the points lie in the feasible domain i.e., all the constraints are satisfied.

The Mooney-Rivlin curve fitting for strain rate of 0.1 s^{-1} is performed for 1000 times with different combinations of convergence criteria and different strategies to evaluate the efficiency of each technique and the results are shown in Table 2.5.

The tolerance for SF, SP and PR convergence criteria is set as 10^{-6} , 10^{-6} and 10^{-4}, respectively. As it can be seen, irrespective of the convergence criteria, the CF-PSO showed a better performance and reached the convergence in fewer number of iterations. The CF-PSO was able to drop down the convergence speed by approximately 11.0%, 6.5%, and 11.2% using SF, SP,

Table 2.5. The efficiency and accuracy of Mooney-Rivlin hyperelastic characterization with different PSO techniques including unconstrained, constrained, and constrained with feasible initial swarm, associated with different convergence criteria.

		Convergence criteria		
		SF	SP	PR
UC-PSO	Avg it. #	59.1	96.6	56.2
	Avg error	0.0005	0.0005	0.0005
C-PSO	Avg it. #	58.8	96.4	56.2
	Avg error	0.0005	0.0005	0.0005
CF-PSO	Avg it. #	52.6	90.0	49.8
	Avg error	0.0005	0.0005	0.0006

and PR convergence criteria relative to the C-PSO and UC-PSO techniques. This faster convergence is not due to a compromise in accuracy, since, as can be seen from Table 2.5, the average error does not show any notable difference for CF-PSO, compared to the other solution techniques.

As it can be seen from Table 2.5, the C-PSO does not show any improvement compared to the UC-PSO method. This is expected since opposed to some other optimization techniques such as simulated annealing, the fitness value of particles does not play any role in their evolution. Therefore, the relative value (fitness) of the particles does not play any role in their evolution, and the only controlling parameter is the location of the best particle which is very likely to lie in the feasible subdomain of the solution.

2.3.2. Visco-hyperelastic curve fitting

As mentioned earlier, the visco-hyperelastic curve fitting is relatively more complicated compared to that of the hyperelastic due to the higher number of variables and the imposed constraints on the problem. As a result, coming up with the right choice of initial guess becomes harder for the visco-hyperelastic characterization.

The relaxation test data for unconfined compression test on the bovine brain tissue with the strain rate of 0.1, 0.7, and 7 s^{-1} is shown in Figure 2.10.

Using the Ogden visco-hyperelastic model expanded by two terms Prony series, our goal is to find the parameters q_1, q_2 and τ_1, τ_2 that minimizes the error of curve fitting, while satisfying the constraints explained in equations (2.21) and (2.22). These constraints lead to the following

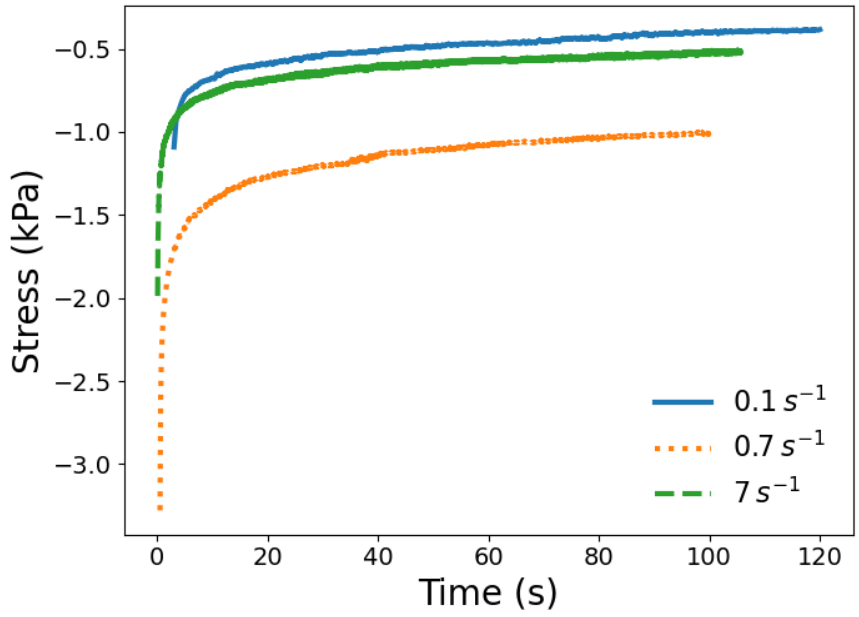

Figure 2.10. The relaxation phase of the unconfined compression test for bovine brain sample at three different strain rates of 0.1, 0.7, and 7 s^{-1}. The sample is relaxed for between 100 to 120 seconds for each corresponding strain rate.

inequalities for two term Prony series expansion:

$$q_1 + q_2 < 1 \tag{2.37}$$

$$\tau_1 - \tau_2 < 0 \tag{2.38}$$

The initial shear modulus and the respective Ogden parameter are found before as presented in Table 2.2 to 2.4. Looking into equation (2.37) as a constraint, the parameters q_1 and q_2 clearly needs to be bounded. In this case, the application of LMA method is not justifiable anymore, since the commercially available packages cannot use LMA for bounded optimization problems. It should be noted that the "scipy.optimize.curve_fit" optimization package in Python uses trust region reflective (TRF) algorithm [64] to solve for the curve fitting optimization in bounded cases.

Applying the C-PSO, the Prony series parameters for different strain rates are found and compared with that of the TRF algorithm as presented in Table 6. The lower and upper bound of the parameters q_1 and q_2 were set to be 0.001 and 0.999, and the parameters τ_1 and τ_2 were

bounded in the range of 0.001 s to 120 s (corresponding to total time of relaxation test) for both C-PSO and TRF algorithms. All the parameters were set equal to 0.1 as an initial guess for the TRF algorithm. Several other initial guesses were made, but the outcomes were no different. The C-PSO method was able to approximate the Prony series parameters with better accuracy leading to higher coefficient of determination. Looking into Table 2.6, the coefficient of determination for the TRF algorithm in the cases with the strain rates of 0.7, and 7 s^{-1} turns out to be a large negative value which clearly shows the poor performance of the TRF algorithm. The negative R^2 value suggest that using the average value of the stress for approximation yields more accurate approximation than that of the TRF algorithm. Figure 2.11 shows the curve fitting and approximation with the visco-hyperelastic coefficients found by C-PSO and TRF algorithms. It can be clearly seen that the TRF algorithm cannot provide a good approximation which consequently leads to negative coefficient of determination for the strain rates of 0.7 and 7 s^{-1}.

Table 2.6. The obtained Prony series expansion parameters for Ogden visco-hyperelastic constitutive model through C-PSO, and TRF algorithms.

	Strain rate (s^{-1})	q_1	τ_1 (s)	q_2	τ_2 (s)	R^2 (%)
C-PSO	0.1	0.4080	0.9191	0.2834	40.4249	98.53
TRF	0.1	0.4038	0.9444	0.2852	40.4104	98.39
C-PSO	0.7	0.3991	1.4030	0.2160	33.6624	98.80
TRF	0.7	0.001	110.0000	0.2214	110.0000	-3846
C-PSO	7	0.6424	0.01	0.1771	12.4351	87.28
TRF	7	0.3347	3.4801	0.2465	40.1121	-5641

Similar to what was done for hyperelastic fitting, the efficiency of different C-PSO techniques are investigated by running the algorithms for 1000 times for the case with the strain rate of 0.1 s^{-1}. The average of the square of error and the required iterations for convergence (using different convergence criteria) are inspected and presented in Table 2.7.

Given the results in Table 2.7, the CF-PSO technique slightly reduces the number of required iterations compared to the C-PSO and UC-PSO and the efficiency improvement is not as considerable as what was noticed in hyperelastic characterization. The SF convergence criteria required lower number of iterations for reaching the convergence and hence can be beneficial when

Table 2.7. The efficiency and accuracy of Ogden visco-hyperelastic characterization with different PSO techniques including unconstrained, constrained, and constrained with feasible initial swarm, associated with different convergence criteria.

		Convergence criteria		
		SF	SP	PR
UC-PSO	Avg it. #	43.0	73.4	69.6
	Avg error	0.00018	0.00019	0.00017
C-PSO	Avg it. #	44.0	74.4	70.1
	Avg error	0.00019	0.00019	0.00017
CF-PSO	Avg it. #	42.9	70.9	69.5
	Avg error	0.00017	0.00019	0.00017

used in simulation-based optimizations. The average error noticed for all these techniques are very close to each other.

2.4. Conclusion

In this study, the C-PSO algorithm as a derivative free optimization method, was employed for characterization of bovine brain tissue. Due to the nonlinear behavior of brain, the hyperelastic models including one-term Ogden, Mooney-Rivlin, Yeoh, and Neo-Hookean, and Ogden visco-hyperelastic model was used for time-independent and time-dependent material characterization, respectively. The results obtained by C-PSO method was then compared with that of the classic LMA and TRF gradient-based optimization methods. The least-square error and penalty function approach were employed for defining the optimization problem and handling the constraints, respectively. Results show that the C-PSO method was able to give as accurate result as that of the LMA for Ogden and Mooney-Rivlin hyperelastic model while ensuring that the imposed constraints of the hyperelastic models are satisfied. However, the result for Yeoh model was not the same and LMA method gives slightly better accuracy in terms of coefficient of determination. In the Yeoh model, the values obtained from PSO and LMA method are high and close to each other, but the resultant parameters are not close and relatively large difference is observed. Further analysis may be necessary to evaluate which sets of parameters are better. One of the factors lending help to such an analysis is the stability of the model in the higher range of strains.

The application of C-PSO method becomes more notable and worthy in the case of visco-hyperelastic modeling since the imposed constraints become more challenging and certain parameters in Prony series expansion need to be bounded as well. The bounded optimization cannot be

handled by LMA algorithm and hence, TRF algorithm which is commercially available in Python "Scipy" package was used as an alternative. While TRF algorithm is designed for solving bounded curve fitting, it failed to find the Prony series parameters for the strain rates of 0.7 and 7 s^{-1} while the C-PSO method successfully found the Prony series parameters with high coefficient of determination. Moreover, for the strain rate of $0.1s^{-1}$ where TRF algorithm showed success, it was still less accurate compared to the C-PSO algorithm. It was shown that the constrained PSO algorithm can characterize the brain tissue in terms of Ogden visco-hyperelastic by finding the parameters of two-term Prony series expansion. Moreover, the efficiency of the C-PSO algorithm was shown to be improved up to 11% in convergence speed, upon creating an initial feasible swarm, regardless of the convergence criteria in use.

Given the results of this study, while the LMA method showed good performance in hyperelastic characterization, C-PSO method can be used as an extra assurance method to make sure that the result is the global optimum of the problem and not the local minima. However, it seems completely necessary to use C-PSO or other derivative free optimization techniques for visco-hyperelastic curve fitting. Moreover, the suggested modifications to the C-PSO method can be beneficial in reducing the time complexity of the algorithm specially for simulation-based characterization of soft tissues.

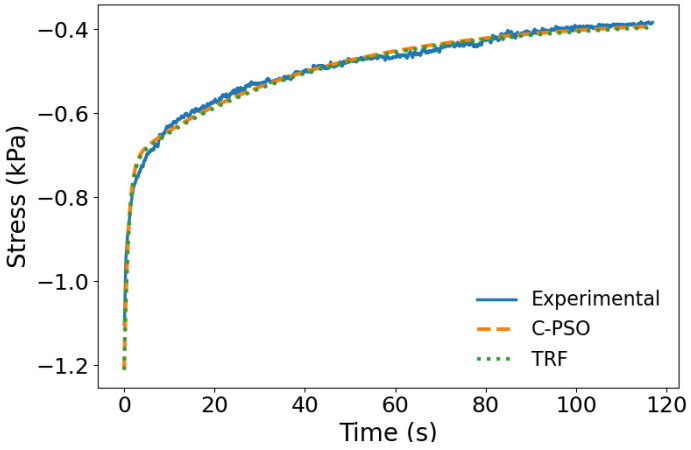

(a)

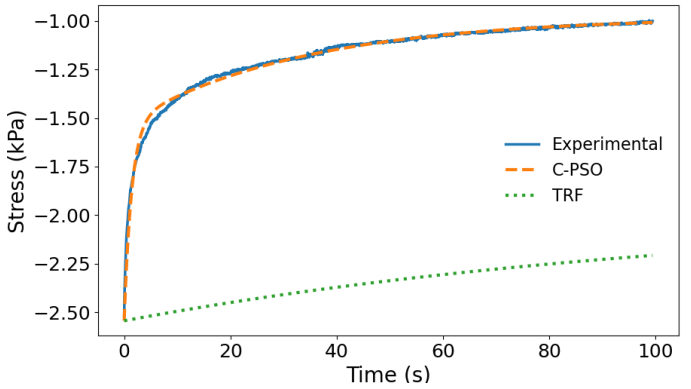

(b)

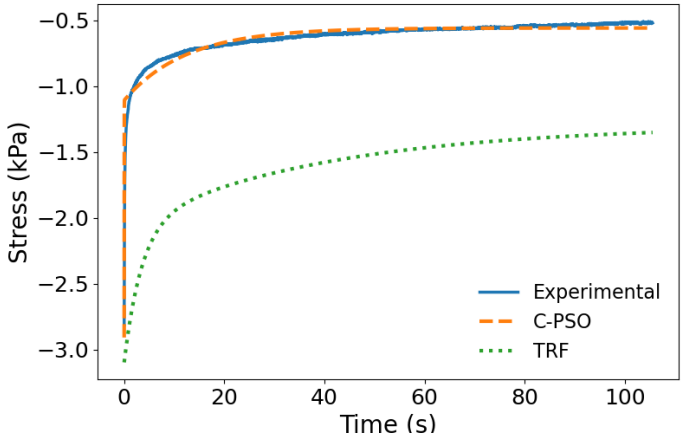

(c)

Figure 2.11. The fitted Ogden visco-hyperelastic model to the relaxation test data by the parameters found through C-PSO and TRF algorithm presented in Table 6 for the strain rates of (a) 0.1 s^{-1}, (b) 0.7 s^{-1}, and (c) 7 s^{-1}.

3. OPTIMIZED MICROMECHANICAL HYPERELASTIC CHARACTERIZATION OF HUMAN BRAIN WHITE MATTER

3.1. Introduction and literature review

TBI can happen due to many factors including sudden movement of the head, ballistic impact, or shock waves created by explosions. Computational techniques such as finite element enables us to conduct simulations for modeling the human brain response under different loading scenarios. Extensive research has been done in this field, some of which are mentioned here as references [37, 38, 84–87]. However, the validity and exactness of computer simulations using finite element human head model remains a challenge. Material properties and right constitutive model are some of the most important factors required for accurate assessment of the mechanical behavior of the brain and other organs of human head. To this end, numerous studies have been conducted to obtain material properties of the brain in macro-scale using experimental techniques [47, 52, 54, 88–91].

DAI is one of the most common form of TBI which accounts for 40-50% of TBI cases [92,93]. DAI happens with the formation of lesions in brain stem and corpus callosum [94] and is associated with the separation and disconnection of axons [95]. As axons are micro-level constituents of brain white matter, their micro-structural analysis can be helpful for ongoing research in the biomechanical field and therefore, it is required to find its material property.

The study of the brain white matter at the scale of its constituents enables us to find the micro-level stress in the brain under TBI-causing loading scenarios. Micromechanical simulations that have been extensively used for analysis of fibrous composites [96,97] can be used for this purpose. Usually a representative volume element (RVE) can be used to represent the whole structure by repeating itself in different directions.

The material in this chapter was co-authored by Mohammadreza Ramzanpour, Mohammad Hosseini-Farid, Mariusz Ziejewski, and Ghodrat Karami. Mohammadreza Ramzanpour was mainly responsible for data collection, analysis, algorithm development, and the conclusions advanced here. The other co-authors helped in proof-reading. Ghodrat Karami supervised the project.

Micromechanical studies have been conducted for material characterization of brain white matter tissue as well. Different regions of brain white matter such as brain stem and corpus callosum have highly oriented axons in the extra-cellular matrix which resembles the fibrous composite structure [98]. Abolfathi et al. [99] used linear viscoelastic model for both axon and ECM to obtain the anisotropic material properties of brain white matter under small deformation. They showed that brain white matter exhibits transverse isotropic behavior. Moreover, the effect of the axons' volume fraction and its undulation on the brain material properties were investigated. Karami et al. [100] used micromechanical analysis to simulate brain white matter under large deformation by the Ogden hyperelastic model. Using material properties of axons and ECM in guinea pig optic nerves reported by Meany et al. [3], they obtained the mechanical response of brain white matter tissue. It was shown that the increase in the axons' volume fraction results in increase of normal stress applied to the axons. Cloots et al. [23] studied the effect of axons' orientation and presence of inclusion on brain tissue deformation under loading. By modeling three different cases with maximum axons diversion angles of 30°, 45° and 60°, maximum increase of 250% in logarithmic strain of axons were observed. The presence of rigid inclusion was reported to cause 60% increase in logarithmic strain of axons compared to the no-inclusion case. Yousefsani et al. [36] applied an embedded element technique to estimate the localized stress of axons in transverse large deformation using the hyperelastic Ogden model. Moreover, they compared the results of two different RVEs, uniform and randomly distributed axons. It was shown that the tissue response is not contingent upon the distribution pattern of axons in RVE. This result will be later used as a ground for coming up with our simplified model. In those studies, the micromechanical stress, and the transfer of stress from macro to micro level were studied which requires the knowledge of the material properties of brain white matter constituents.

Genetic algorithm (GA) is an evolutionary algorithm based on natural selection process that can be used for both constrained and unconstrained single-objective and multi-objective optimization problems [101]. Many studies have employed GA for material constitutive modeling. Ning et al. [18] applied the GA algorithm with iterative finite element analysis, to determine viscoelastic material properties of a porcine brainstem in three different directions for small shear deformation. Javid et al. [2] optimized axon and ECM viscoelastic material properties of the porcine brainstem. In their study, they performed an experimental uniaxial tension test on brain samples and used

its data to find the material properties of axons and ECM which gives the closest result to their experimental test. However, the linear viscoelastic model used by Javid et al. is appropriate for small deformation and the reported properties of axons and ECM are only calibrated for tensile loading and cannot be used for other loading modes such as compression or shear.

This paper is aimed to identify hyperelastic material properties of axons and ECM in different uniaxial loading conditions including tension, compression, and shear. For this purpose, GA optimization procedure is employed to find the properties of axons and ECM that minimize the error of approximation with the known corpus callosum mechanical response from quasi-static experimental tests reported in [1]. Additionally, Nelder-Mead simplex optimization method is employed to find best-fit parameters that can best describe the behavior of axons and ECM for all three uniaxial loading cases.

3.2. Methodology

In this section, micromechanical simulations which is a backbone of further analyses will be discussed, the hyperelastic constitutive formulation for different loading scenarios would be investigated, and in the final subsection, the global optimization framework needed for finding the optimal and best-fit parameters will be introduced.

3.2.1. Micromechanical finite element modeling

Micromechanical modeling studies the materials at the scale of their constituents. The key idea behind micromechanical simulation is to find the proper heterogeneous RVE that, by its repetition, the whole structure will be approximately formed. Brain white matter tissue including corpus callosum and brain stem has unidirectional, highly oriented fibrous composite structure. This fact agrees with the provided Scanning Electron Microscopy (SEM) of brainstem published by Javid et al. [2] and diffusion tensor imaging of the brain tissue [1] representing the direction of nerve bundles for different regions of brain including corpus callosum where the nerve fiber bundles are shown to be highly oriented.

Here, it is assumed that axons have same size and uniform cross section with no undulation, distributed throughout the ECM. Moreover, the distributions of axons can be further simplified into more disciplined structured format. Figure 3.1 shows square distribution of axons in ECM with its corresponding RVE. As mentioned earlier, these simplifying assumptions are based on the previous studies such as [2, 36] where it was confirmed that there is no notable difference between

the results of the random and simple RVE. The volume fraction of axons is taken to be 52.7% which is the reported value by Javid et al [2] (Figure 3.1a). They found the volume fraction of axons by processing the SEM image of the porcine brainstem shown in Figure 3.1a. The validity of the meshed RVE model and its respective element size was checked through mesh convergence analysis by performing sample simulations.

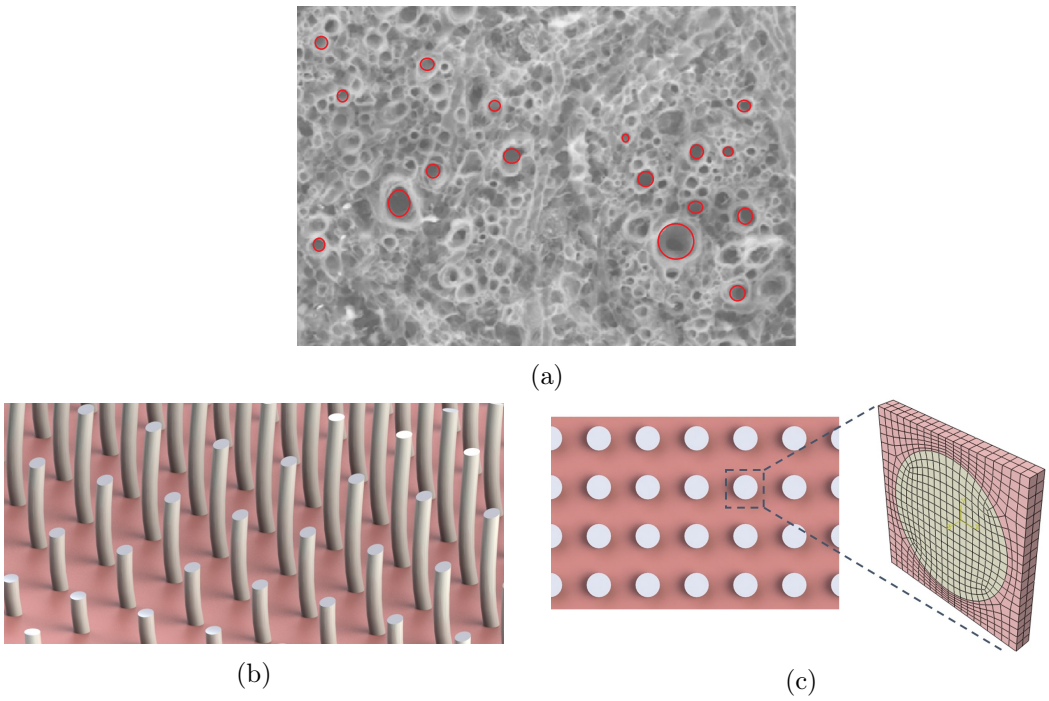

Figure 3.1. (a)Scanning Electron Microscopy image of porcine brainstem shows axons distribution in ECM presented by red circles [2],(b) Three-dimensional representation of axons distribution in extracellular matrix (ECM) based on the simplifying assumptions, (c) Schematic two dimensional view of axons distribution in ECM and the respective representative volume element (RVE).

To make the RVE repeats itself in the desired directions, periodic boundary conditions (PBC) must be applied to it. PBC controls the displacement of the opposing faces, edges and nodes of the RVE with respect to one another. In this regard, one of the faces/nodes is taken as the controlling face/node with no restriction applied, while the opposing face/node is taken as a controlled, which its displacement is determined and controlled by the displacement of the controlling face/node. In Figure 3.2, faces 1, 3 and 5 are controlling faces while faces 2, 4 and 6 are controlled ones. In a three-dimensional case, the PBC can be written as stated in equations 3.1 to 3.8 with respect to Figure 3.2. Since, the undulation of axons is ignored in the Z-direction, the depth of the RVE in

the Z-direction does not play any role after applying the PBC and only two layers of meshed finite element model is used here.

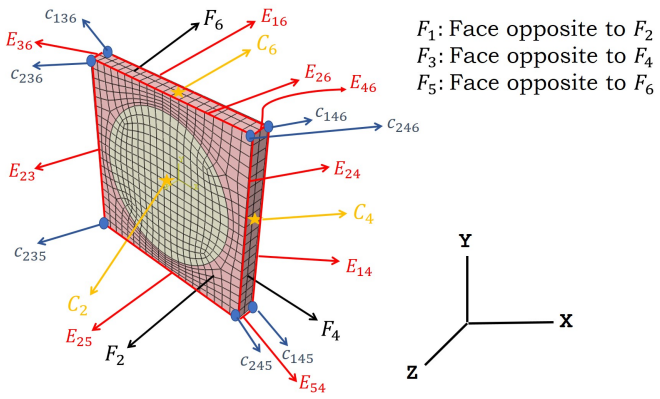

Figure 3.2. Overview of controlling and controlled faces, corner nodes and edge nodes in meshed three-dimensional RVE.

$$u_{C_{i+1}} = -u_{C_i}, \quad i = 1, 3, 5 \tag{3.1}$$

$$u_{F_{i+1}} = -u_{F_i} - u_{C_i} + u_{C_{i+1}}, \quad i = 1, 3, 5 \tag{3.2}$$

$$u_{E_{(i+1)(j+1)}} = u_{E_{ij}} - 2u_{C_i} - 2u_{C_j}, \quad ij = 13, 15, 35 \tag{3.3}$$

$$u_{E_{(i+1)(j+1)}} = u_{E_{i(j+2)}} - 2u_{C_i} - 2u_{C_{j+1}}, \quad ij = 12, 14, 34 \tag{3.4}$$

$$u_{c_{235}} + u_{c_{146}} + 2u_{C_1} - 2u_{C_3} - 2u_{C_5} = 0 \tag{3.5}$$

$$u_{c_{236}} + u_{c_{145}} + 2u_{C_1} - 2u_{C_3} + 2u_{C_5} = 0 \tag{3.6}$$

$$u_{c_{245}} + u_{c_{136}} + 2u_{C_1} + 2u_{C_3} - 2u_{C_5} = 0 \tag{3.7}$$

$$u_{c_{246}} + u_{c_{135}} + 2u_{C_1} + 2u_{C_3} + 2u_{C_5} = 0 \tag{3.8}$$

These equations must be satisfied for all translational degrees of freedom in which u is the displacement of the node or node sets, F_i $(i = 1, 2, ..., 6)$ refers to the node sets lying on faces 1 to 6, C_i $(i = 1, 2, ..., 6)$ denotes center nodes at the corresponding faces, c_{ijk} is the corner node at the intersection of F_i, F_j and F_k and E_{ij} is the node set on the edge lying on F_i and F_j intersection. Moreover, great care should be taken to enforce the mesh nodes on the opposite faces to be precisely matched together. Additionally, the meshing geometry on the faces must be exactly symmetrical with respect to the center node of the corresponding face. To avoid rigid body motion, the center node of the structure is fixed in the Z-direction, center nodes of faces 1 and 2 (C_1 and C_2) are fixed in the X and Y-direction and one arbitrary node on E_{25} edge is fixed in the X-direction.

While the micromechanical simulation result, demonstrates the stress-strain distribution in the micro scale, to approximate the result at the higher scale (macro), the volume averaging technique can be used since RVE represents a point from the bulk volume of material. The averaging can be done based on the following equation:

$$\bar{\sigma} = \frac{\sum_{i=1}^{m} \sigma_i v_i}{\sum_{i=1}^{m} v_i}, \quad \bar{\epsilon} = \frac{\sum_{i=1}^{m} \epsilon_i v_i}{\sum_{i=1}^{m} v_i} \tag{3.9}$$

in which $\bar{\sigma}$ and $\bar{\epsilon}$ are averaged stress and strain values, σ_i and ϵ_i are the local stress and strain values for the i^{th} element of the finite element model, and v_i is the i^{th} element volume size. The obtained averaged stress and strain values can further be used to obtain the hyperelastic material properties of brain white matter.

3.2.2. Hyperelastic constitutive modeling

For the cases where large deformation happen, linear elasticity can be generalized into a nonlinear form for predicting stress-strain time-independent behavior of materials. Characterizing hyperelastic properties can be done using the hyperelastic strain energy function W. The strain energy function can be written in terms of the strain invariants I_1, I_2, and I_3 or principal strains (or stretches).

One of the most common strain energy functions applied to soft biological tissues is the hyperelastic Ogden model which depends on principal stretch values [102] as stated in the following:

$$W_{Ogden} = \sum_{i=1}^{N} \frac{2\mu_i}{{\alpha_i}^2} \left(\lambda_1^{\alpha_i} + \lambda_2^{\alpha_i} + \lambda_3^{\alpha_i} - 3\right) \tag{3.10}$$

where α_i is the material parameter, μ_i is the initial shear modulus and N is the number of terms used in the Ogden model. $\lambda_k,\ k = 1, 2, 3$ are the principal stretch values which can be obtained from the principal strain values $\epsilon_k,\ k = 1, 2, 3$ based on the following equation.

$$\lambda_k = 1 + \epsilon_k \quad k = 1, 2, 3 \tag{3.11}$$

It should be noted that in equation 3.10, compressibility term is ignored for Ogden strain energy function under assumption that brain is incompressible [103]. For uniaxial compression or tensile loading conditions, the deformation gradient tensor $\boldsymbol{F}$ and the principal stretches can be stated as the following:

$$\boldsymbol{F} = \begin{bmatrix} \lambda & 0 & 0 \\ 0 & \frac{1}{\sqrt{\lambda}} & 0 \\ 0 & 0 & \frac{1}{\sqrt{\lambda}} \end{bmatrix} \tag{3.12}$$

$$\lambda_1 = \lambda, \quad \lambda_2 = \lambda_3 = \frac{1}{\sqrt{\lambda}} \tag{3.13}$$

in which λ_1, λ_2, and λ_3 are the principal stretches. By using equations 3.13 and 3.10, Cauchy stress for uniaxial tension and compression (σ_{ii}) can be written as the following for one-term Ogden model:

$$\sigma_{ii} = \frac{2\mu}{\alpha} \left(\lambda^{\alpha} - \left(\frac{1}{\sqrt{\lambda}}\right)^{\alpha}\right) \tag{3.14}$$

in which λ is the maximum principal stretch for tension and minimum principal stretch for compression loading, μ is the initial shear modulus and α is the Ogden model parameter. Equation 3.14 is used for fitting the obtained stress and stretch values in uniaxial tension and compression loading to find the Ogden material parameters.

For the incompressible simple shear mode with plane stress condition, deformation gradient and principal stretch can be written as follows assuming the shear force is employed in YZ component of the tensor notation of stress.

$$\boldsymbol{F} = \begin{bmatrix} 1 & 0 & 0 \\ 0 & 1 & \gamma \\ 0 & 0 & 1 \end{bmatrix} \tag{3.15}$$

where γ is the shear strain. It should be noted that equation 3.15 is true by the assumption that the cross section of the object remains constant during the shear deformation which is the case in our study. In the case of simple shear, shear strain can be formulated as $\gamma = \Delta l/H$ with Δl and H shown in Figure 3.3.

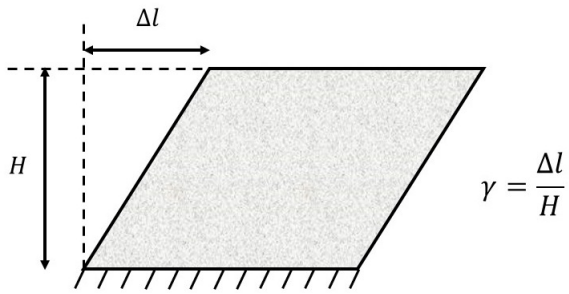

Figure 3.3. Material deformation in the case of simple shear; the bottom plate is fixed, and the shear force is taking place at the upper plate causing length change of Δl. The amount of shear is denoted by γ.

For the simple shear loading mode, the principal stretches λ_1, λ_2, and λ_3 can be stated as the following:

$$\lambda_1 = \frac{\gamma}{2} + \sqrt{1 + \frac{\gamma^2}{4}}, \quad \lambda_2 = \frac{1}{\lambda_1}, \quad \lambda_3 = 1 \tag{3.16}$$

Thereafter, the Cauchy shear stress can be found by equation 3.17:

$$\sigma_{ij} = \frac{2\mu}{\alpha} \frac{1}{\lambda_1 + \lambda_2} \left[{\lambda_1}^{\alpha} - {\lambda_2}^{\alpha} \right] \tag{3.17}$$

in which σ_{ij} is the ij component of the stress tensor where $i \neq j$ assuming the non-zero strain and displacement corresponds to the ij component of the strain tensor, λ_1 and λ_2 ($\lambda_1 > \lambda_2$) are

the principal stretches found from equation 3.16, μ is the initial shear modulus and α is the Ogden material parameter. For more details, readers are referred to [46, 74, 104].

3.2.3. Optimization framework

Several studies have used optimization techniques for finite element-based characterization of materials [27,28,60,66]. In this study, the experimental data reported by Budday et al. [1] is used for hyperelastic characterization of corpus callosum (brain white matter) to find the hyperelastic Ogden parameters of axon and ECM. Budday et al. [1] tested human brain tissue in different loading conditions of shear, compression, and tension to find its mechanical response. The obtained data was then fitted to five different hyperelastic models including neo-Hookean, Mooney-Rivlin, Demiray, Gent, and Ogden. In their work, it was shown that material parameters obtained in one specific loading condition cannot be used for predicting the material behavior in other loading conditions. Therefore, in a try to calibrate their result for all loading modes, it was demonstrated that the Ogden model is the only model capable of giving a good simultaneous fit to all three uniaxial loading modes of simple shear, compression, and tensile loadings.

To find the material properties of axon and ECM, in this study, iterative micromechanical finite element modeling in ABAQUS (ABAQUS 2016, Dassault Systems, Providence RI) was used with the GA algorithm in MATLAB (version 9.4.0 R2018a, Mathworks inc., Natick MA). The Ogden hyperelastic model was chosen as it was found to be the best model for describing brain deformation in different loading conditions as stated earlier. The flowchart of the optimization procedure is illustrated in Figure 3.4. A script is written to change the material parameters of axon and ECM, execute the simulation on ABAQUS, reading the output data from the ABAQUS and feed it to the objective function which is aimed to be minimized. The Ogden material properties found in Budday et al. studies for corpus callosum [1] in compression, tension and shear are used to find the stress in arbitrary range of stretch corresponding to the loading mode. For each iteration of micromechanical simulation, the obtained stress-stretch data is fitted to its respective Ogden model to find respective μ and α for the whole structure. These parameters are used to find the stress values at the same range of stretch used for the data in [1]. Thereafter, the objective function E

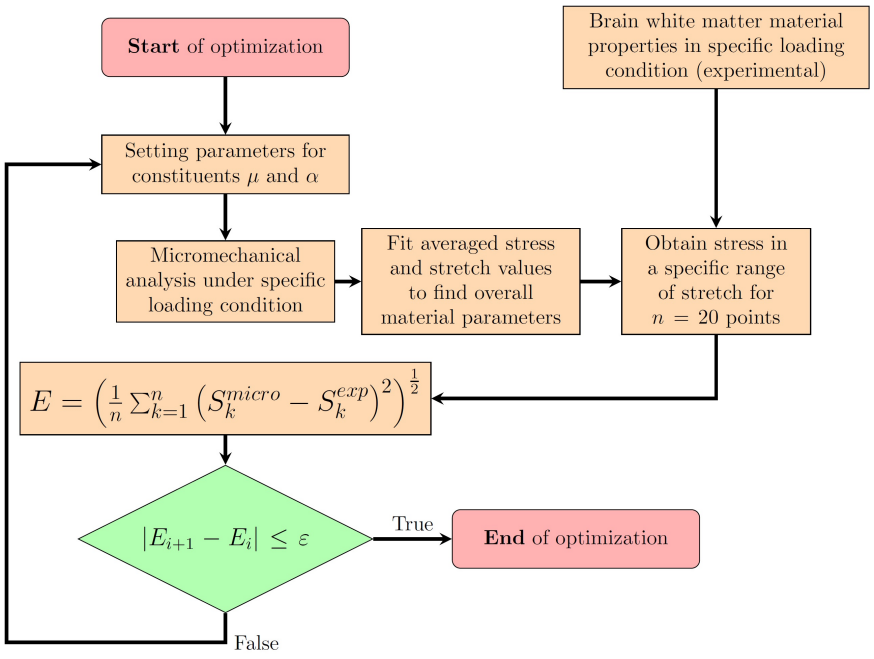

Figure 3.4. Flowchart of the optimization control for finding optimum Ogden hyperelastic material properties. The iterative procedure continues until the change in objective Function in two consecutive iterations (denoted by i and $i+1$) falls under the function tolerance level.

which is a function of axon and ECM material parameters is calculated as given in the following:

$$E(\mu_{axon}, \alpha_{axon}, \mu_{ECM}, \alpha_{ECM}) = \left(\frac{1}{n}\sum_{k=1}^{n}\left(S_k^{micro} - S_k^{exp}\right)^2\right)^{\frac{1}{2}} \tag{3.18}$$

n is the total number of points considered in stress-stretch dataset, S^{micro} denotes the averaged stress values from micromechanical analysis and S^{exp} corresponds to the stress-stretch values obtained from experimental tests conducted by Budday et al. [1]. The objective function defined in equation 3.18 is dependent on the results of micromechanical simulation. Therefore, the gradient of this function cannot be calculated and gradient based optimization methods such as gradient descent cannot be applied here. Derivative free optimization methods also known as black-box optimization are suitable to be used under these circumstances and GA optimization algorithm [82] is selected in this study. GA continues to create generations until the change in objective function gets smaller than the set function tolerance level. It should be noted that good choice of initial parameters which affects the initial population in GA, is very advantageous for accelerating the convergence.

In this paper, the parameters obtained from the optimization framework illustrated in Figure 3.4 are named as optimal parameters. These parameters are derived for specific loading modes including tension, compression, and simple shear. Hence, these parameters are likely to vary for each loading mode and the parameters for one loading mode cannot be used for the another. To obtain one set of parameters that can best describe the behavior of the material in all uniaxial loading modes, the Nelder-Mead simplex optimization algorithm [105] is employed to minimize the error of approximation when one set of parameters, called as best-fit parameters, is used for all loading modes. In other words, the procedure of finding the best fit parameter can be interpreted as a simultaneous fitting to the three loading modes. The objective function in this case can be constructed as stated in the following, considering the one-term Ogden model:

$$E(\mu_{best}, \alpha_{best}) = \sum_{i=1}^{3} \int_{\lambda_1^i}^{\lambda_2^i} (\sigma_{best} - \sigma_i)^2 \, d\lambda \tag{3.19}$$

where $i = 1, 2, 3$ corresponds to the loading modes of tension, compression, and shear. μ_{best} and α_{best} denotes the best-fit parameters, λ_1^i and λ_2^i refer to the initial and final stretch/shear strain values in the corresponding loading modes, σ_{best} and σ_i represents the approximated stress using the best-fit parameters and the target stress of each loading mode, respectively. σ_{best} for compression/tension and simple shear are calculated based on equations 3.14 and 3.17, respectively.

3.3. Results

The GA optimization procedure is carried on minimizing the difference of averaged micromechanical stresses with the mechanical response of corpus callosum in arbitrary range of stretch or shear strain values. The optimization parameters are taken to be $\mu_{axon}, \mu_{ECM}, \alpha_{axon}$ and α_{ECM} for Ogden hyperelastic model. It should be noted that if no constraint is applied to these parameters, the optimization procedure will result in the same parameters as those of the corpus callosum. Therefore, an equality constraint of $\mu_{axon}/\mu_{ECM} = 3.0$ is imposed on the solution which is consistent to different previous studies [2, 3, 99, 100]. GA algorithm was executed with the function tolerance level set as 10^{-4} and it converged after 94, 51 and 101 generations for tension, compression, and simple shear modes.

Table 3.1 presents the known Ogden material parameters for corpus callosum [1] and the calculated optimal material parameters of axon and ECM (micro level constituents) in tension,

compression, and shear mode by the proposed optimization framework. The calculated best-fit parameters for axon and ECM are presented in Table 3.1 as well.

Table 3.1. Optimal material parameters (Ogden hyperelastic) for corpus callosum and its corresponding axon and ECM in different loading conditions and the best fit parameters.

Material	Tension		Compression		Shear		Best fit	
	$\mu(kPa)$	α	$\mu(kPa)$	α	$\mu(kPa)$	α	$\mu(kPa)$	α
Corpus Callosum	0.35	-26.6	0.43	-22.8	0.32	-22.8	0.35	-25.30
Axon	0.51	-26.51	0.63	-22.73	0.48	-22.68	0.531	-25.13
ECM	0.17	-26.67	0.21	-22.84	0.16	-22.65	0.177	-25.23

The reported Ogden hyperelastic properties of corpus callosum is characterized through quasi-static experimental tests by Budday et al. [1]. As a result, the obtained material parameters of axon and ECM corresponds best to the applications with low strain rates. Several studies have investigated the strain rate dependency of brain tissue mechanical response by characterizing it in dynamic strain rates [25, 26, 53, 55, 106, 107].

Figure 3.5 illustrates the stress-stretch behavior of axon in tension, compression, and shear for the stretch range of $(1, 1.1)$, $(0.9, 1)$ and shear strain range of $(0, 0.2)$, respectively using optimal and best-fit parameters. The stretch and shear ranges used here are the ones that have used for material characterization in the optimization framework and is consistent with the experiments of Budday et al. [1]. Figure 3.6 presents same diagrams for ECM. The coefficient of determination (R^2) for the approximation with the best-fit parameter compared to optimal parameters is presented in Table 3.2. R^2 values show a close approximation between best fit and optimal parameters while having best match for the tension mode and worst for the shear mode for both axon and ECM.

Table 3.2. Coefficient of determination (R^2) for best fit parameters in stress-stretch correlation of axon and ECM in different loading conditions.

Material	Coefficient of determination (R^2)		
	Tension	Compression	Shear
Axon	99.5%	99.3%	84.5%
ECM	99.6%	99.3%	83.6%

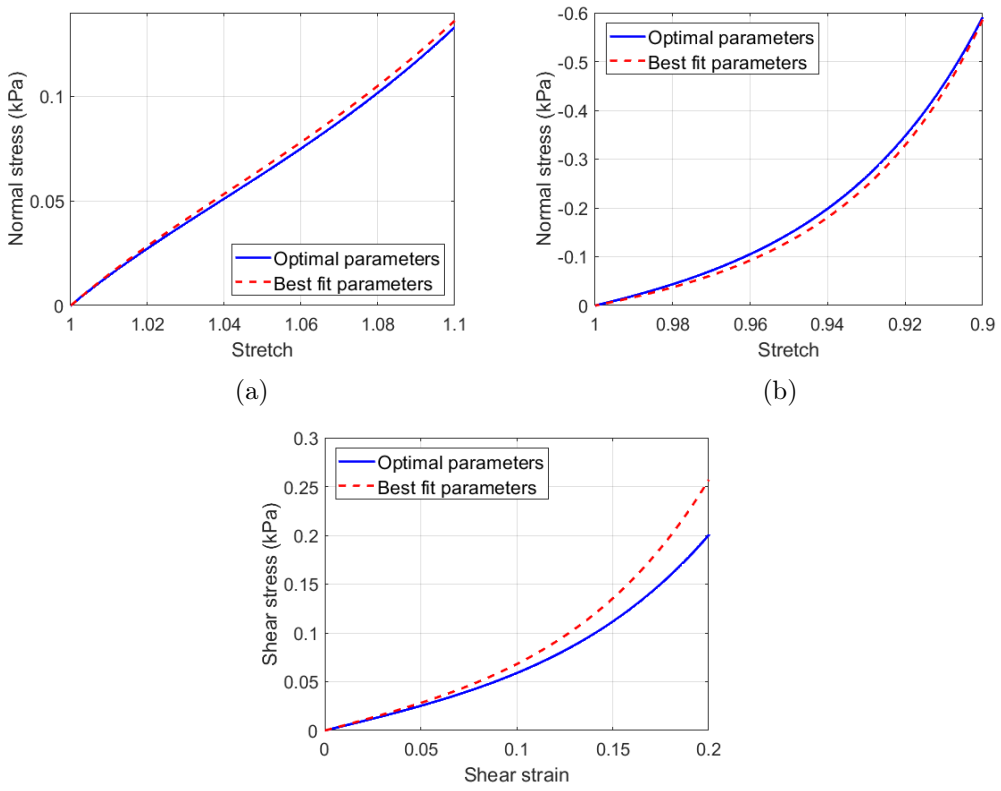

Figure 3.5. Comparison of the stress-stretch or stress-shear behavior of axon material using optimal and best fit parameters which is obtained by minimizing the error of fitting for three modes of tension, compression, and shear for (a) tension, (b) compression, and (c) shear modes.

Micromechanical simulations can be performed using the obtained material properties of axon and ECM. The micromechanical simulation gives the insight into micro-level stress distribution in the brain white matter which shows how the stress magnifies scaling from macro to micro level.

Using optimal parameters of axon and ECM, the micromechanical simulation is performed in tension, compression, and shear loading by applying displacement in the "Z" direction for tension and compression and "YZ" tensorial direction for simple shear (Figure 3.2). The results are shown in Figure 3.7. The final stretch values λ for the tension and compression modes are set to be 1.1 and 0.9, respectively. For the shear load, the final shear strain is set to have a final value of 0.2. Figure 3.7 illustrates the stress distribution for the final mentioned stretch or shear strain value.

To check the accuracy of the calculated optimal parameters and the validity of the applied optimization algorithm, the response of corpus callosum is found by calculating the volume averaged stress of RVE from micromechanical simulations. The obtained results for the three different loading

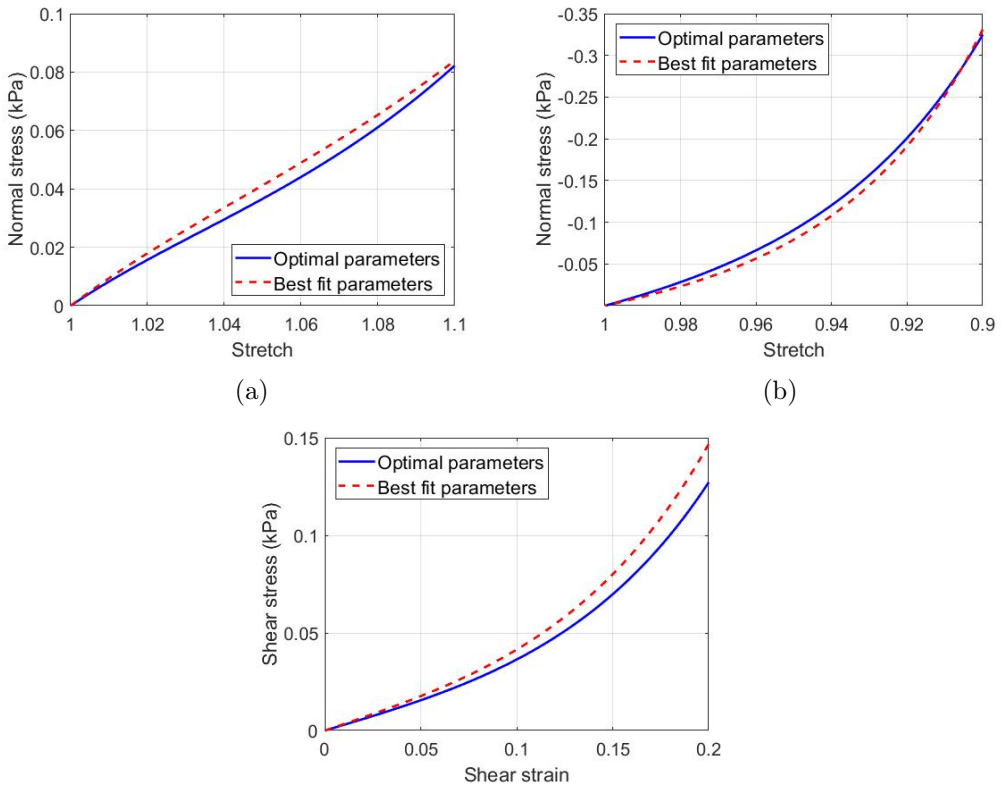

Figure 3.6. Comparison of the stress-stretch or stress-shear behavior of ECM material using optimal and best fit parameters which is obtained by minimizing the error of fitting for three modes of tension, compression, and shear for (a) tension, (b) compression and (c) shear modes.

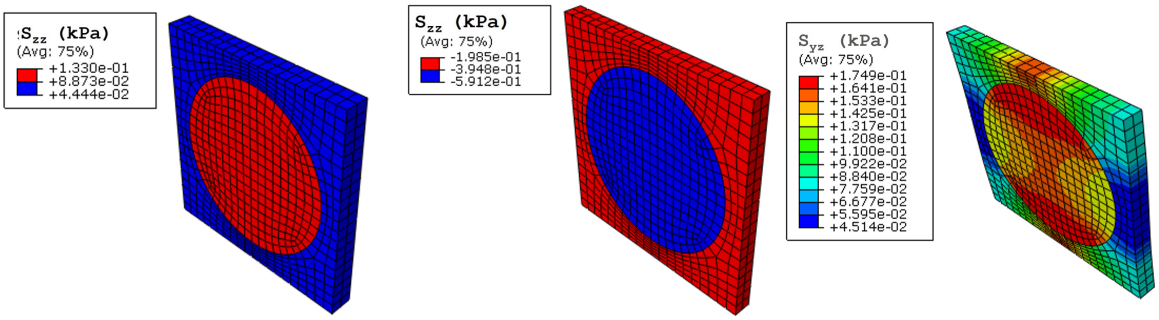

Figure 3.7. Deformed state representation of stress distribution of axon and ECM in micromechanical simulation applying obtained optimal parameters from GA for (a) tension at the stretch value of 1.1, (b) compression at the stretch value of 0.9 and (c) shear for shear of 0.2.

modes are compared with the reported result of Budday et al. [1] and as shown in Figure 3.8, the results are in excellent agreement with referenced values which shows the high accuracy of the predicted optimal parameters for axon and ECM.

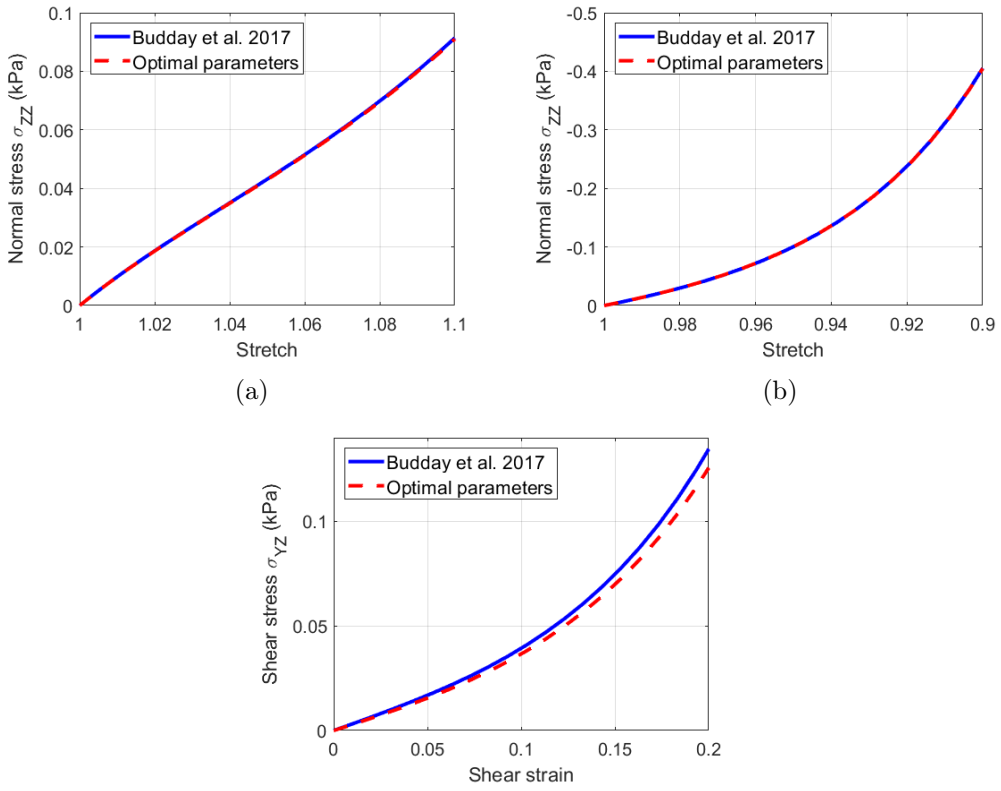

Figure 3.8. Comparison of the stress-stretch behavior of corpus callosum applying optimal parameters found by GA and results of Budday et al. [1] using the reported Ogden parameters for (a) tension, (b) compression and (c) shear.

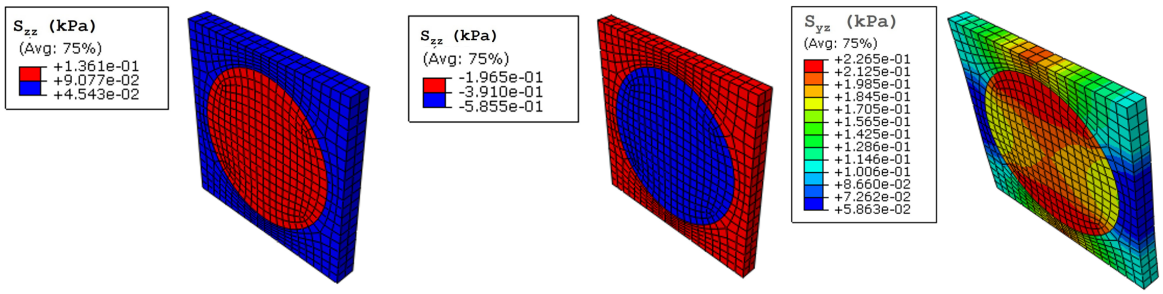

Figure 3.9. Deformed state representation of stress distribution of axon and ECM in micromechanical simulation using best fit parameters obtained by Nelder-Mead simplex method (simultaneous fit to three modes of loading) for (**a**) tension at the stretch value of 1.1, (**b**) compression at the stretch value of 0.9 and (**c**) shear for the shear strain of 0.2.

Moreover, the micromechanical simulation for uniaxial tension, compression, and shear loading is done with the best fit parameters, as shown in Figure 3.9. Comparing the results with those presented in Figure 3.7, the maximum stress obtained by applying best fit parameters shows approx-

imate change of +2%, -1%, and 29% for tension, compression, and shear mode, respectively. This result is consistent with the data presented in Table 3.2 as the best fit parameters showed lowest coefficient of determination for shear loading mode compared to other ones. Figure 3.10 shows mechanical response of corpus callosum in different loading conditions obtained from micromechanical simulations (shown in Figure 3.9) and compared with the referenced data [1] using the axon and ECM best-fit parameters.

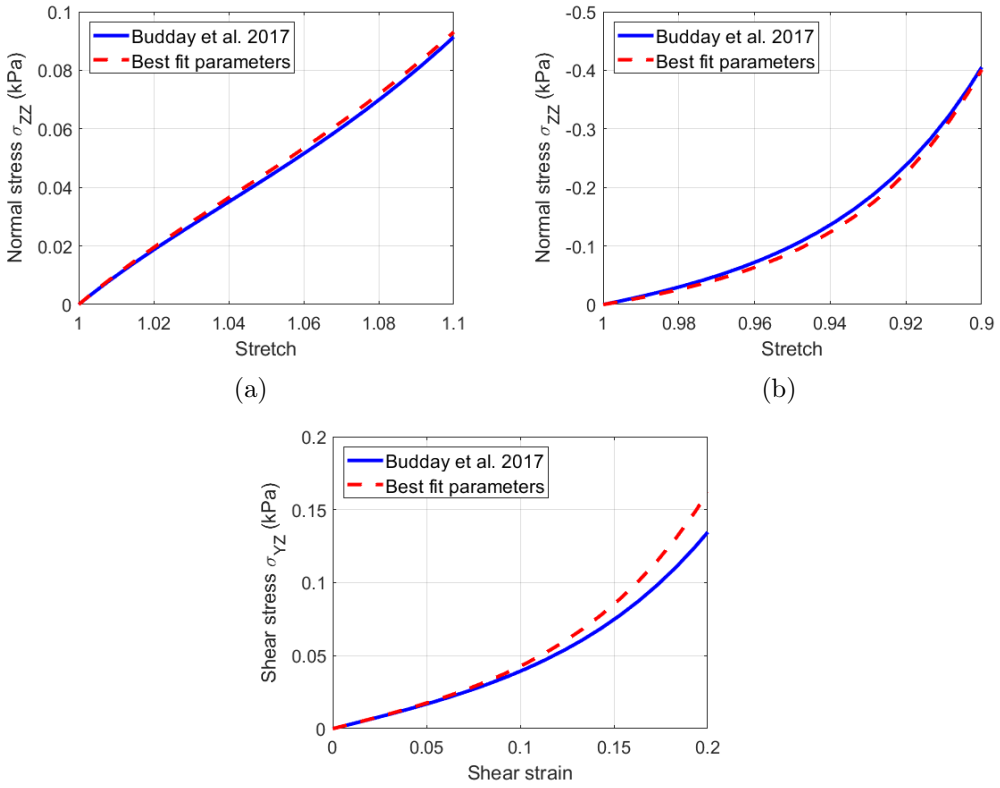

Figure 3.10. Comparison of the stress-stretch behavior of corpus callosum applying best fit parameters of axon and ECM and results of Budday et al. [1] using reported Ogden parameters for (a) tension, (b) compression and (c) shear.

3.4. Discussion

If the material parameters of the axon and ECM in the heterogeneous RVE are set to be equal, the RVE would change into a homogeneous RVE which results in a uniform constant stress distribution. This fact underscores the importance of setting a constant for initial shear modulus ratio of axons and ECM (μ_{axon}/μ_{ECM}). If this ratio constant is not considered in the optimization

problem, the objective function would be optimized with the parameters of axons and ECM equal to the parameters of the corpus callosum.

Moreover, the choice of axons volume fraction is important in the final optimized results. In this paper, the axons volume fraction was obtained from a published study conducted on porcine brainstem [2]. To the authors best knowledge, there is a lack of information on this quantity for human brain white matter and specifically, corpus callosum. However, this parameter can be easily changed and modified in our framework.

Different material properties have been reported in the literature for axons which vary in a wide range. Compared to the best-fit axons shear modulus of 0.531 kPa obtained in this study for human brain white matter, Meaney et al. [3] found the shear modulus of axons in guinea pig optic nerve to be approximately 0.29 kPa and the reported shear modulus of axons for porcine brainstem was 12.9 kPa (tensile loading mode with the strain rate of 5.5 s^{-1} [2]). This value for the porcine corona radiata was found to be about 1.4 kPa according to Yousefsani et al. [108]. Different factors such as the loading mode, strain rate of deformation, and the kind of the tissue used in the experimental study (as the input data) are influential in this variation of the reported results. In this study, the loading mode factor was omitted by introducing the best-fit parameters.

3.5. Conclusion

In this paper, GA optimization method was employed to find the hyperelastic properties of human brain white matter (corpus callosum) constituents including axon and ECM. A square RVE with the axon volume fraction of 52.7% was used and periodic boundary condition was applied to ensure the repetition of the RVE in all directions. The hyperelastic properties of corpus callosum was obtained from Buuday et al. [1] in terms of Ogden hyperelastic model.

The optimal parameters found by GA was then applied in micromechanical analysis and the obtained results were compared with the published result of Budday et al. [1] showing an excellent agreement. This is a confirmation to the authenticity of the proposed optimization algorithm which is based on genetic algorithm and iterative micromechanical finite element simulation. It was shown that these constituents have different properties (called as optimal parameters) in tension, compression, and simple shear loading. Therefore, to report one set of parameters that can best describe the behavior of axons and ECM in all loading modes, best-fit parameters were found through another optimization procedure which minimizes the error for three loading modes simultaneously.

The obtained optimal and best-fit parameters of axon and ECM can be used in the study of brain micromechanics and to find micro level stress and stress concentration in human brain white matter structure. The material characterization for axons and ECM were done by using hyperelastic model. Employing visco-hyperelastic models for time-dependent modeling in different loading scenarios can be done for a future work. Moreover, two parameters of the initial shear modulus ratio of the axons and ECM, and the axons volume fraction can highly affect the resultant parameters. Therefore, if future experimental studies would be able to find the more accurate estimation of those values, the optimal parameters should be updated accordingly.

4. VISCO-HYPERELASTIC CHARACTERIZATION OF HUMAN BRAIN WHITE MATTER MICRO-LEVEL CONSTITUENTS IN DIFFERENT STRAIN RATES

4.1. Introduction and literature review

Traumatic brain injury (TBI) is a common pathology and a major health problem worldwide. Each year, an average of 1.4 million cases of TBI are reported in the United States alone [109]. TBI may happen due to the sudden movement of the head, impact, shock waves due to a blast and generally any mechanical load applied to the head. State of the art research suggests that the primary reason for TBI is the deformation and mechanical strain happening in the brain [110]. Common symptoms associated with TBI include dizziness, headaches, and loss of memory; studies have shown that DAI is the primary cause [111]. DAI which is characterized by the formation of contusions and lesions in the brain white matter happens due to the shear deformation of axons in brain white matter. Corpus callosum and corona radiata are parts of the brain white matter which are known to be commonly affected by the DAI [112]. Understanding the extent of DAI severity and its mechanism can be helpful in preventing such a pathology.

Due to the infeasibility and risks associated with experimental tests, computational techniques are suitable procedures for the simulation of the incidents leading to TBI. In this respect, different scenarios such as coup and contrecoup injuries in impact induced TBIs [38], ballistic impacts [113,114], and blast induced injury [115,116] have been simulated through numerical modeling to find the stress and strain distribution of the brain at the time of the incident. Different factors and parameters lend help to make those simulations more accurate among which, geometrical model exactness, inclusion of different organs of the head and brain in the model, and choice of material properties can be mentioned. As such, extensive efforts have been made to characterize the brain

The material in this chapter was co-authored by Mohammadreza Ramzanpour, Mohammad Hosseini-Farid, Jayse McLean, Mariusz Ziejewski, and Ghodrat Karami. The content of this chapter was published in the journal of Medical & Biological Engineering & Computing, 58(9), 2107-2118. Mohammadreza Ramzanpour was mainly responsible for experimental data collection, analysis, algorithm development, and the conclusions advanced here. The other co-authors helped in proof-reading the paper. Ghodrat Karami supervised the project.

tissue material properties. Brain tissue is an ultra-soft, strain rate sensitive material which shows a nonlinear behavior under loading. Hyperelastic models have been used in numerous studies to model such a behavior. Mihai et al. [58] introduced several hyperelastic models for brain tissue modeling. They focused on development of an appropriate strain energy function that can predict behavior of human brain tissue in mixed loadings of shear, compression, and tension. They found that Ogden model provides a better solution compared to other hyperelastic models such as Mooney-Rivlin, Neo-Hookean, Gent, and Fung in the case of multiaxial loading [58]. Budday et al. [1] tested the human brain tissue in tension, compression, and shear; the mechanical response of the tissue was fitted with several hyperelastic constitutive models. They found that the material property parameters for a specific loading mode cannot be used for other loading modes. In order to obtain one set of material property parameters to be used for general loading cases, they calibrated the material properties to the specific loadings. They also found that the Ogden model outperforms other hyperelastic models in describing the mechanical behavior of brain in all three loading modes by one set of parameters.

Another category of commonly used technique for brain tissue characterization is the indentation test. Feng et al. and Qiu et al. [117, 118] used this test for characterization of injured brain tissue using elastic and viscoelastic constitutive models, respectively. Budday et al. [89] performed long-range and short-range flat punch indentation tests on different parts of the bovine brain tissue. They found out that the white matter was approximately 40% stiffer compared to grey matter. Feng et al. [119] used inverse finite element modeling in conjunction with experimental asymmetrical indentation tests to find the hyperelastic transversely isotropic parameters of the porcine brain white matter under large strain deformation. Moreover, by performing the indentation tests parallel and perpendicular to the brain axonal fiber direction, the orientational dependency of the material parameters were investigated as well.

The study of TBI is usually associated with evaluating the dynamic response of the brain. Brain as a soft material shows a time-dependent behavior where hyperelastic models are not able to provide such information for brain. The time varying stiffness of the solids and specifically soft materials are referred to as viscosity and should be addressed in studying the dynamic behavior of brain. Hosseini-Farid et al. [48] investigated the dynamic response of brain tissue by measuring the instantaneous and equilibrium response of the brain tissue in different strain rates. The instanta-

neous response was calculated using quasi-linear viscoelasticity theory and the equilibrium response was measured through equilibrium stress evaluation. Hyper-viscoelastic models have also been proposed for describing the behavior of other soft biological tissues such as ligaments [120]. Rashid et al. [53] performed relaxation compression tests on brain in different strain rates with the strain values of 0.3 and characterized its response by using hyper-viscoelastic model. The Ogden based hyper-viscoelastic model which its relaxation time-dependent part is based on Prony series expansion was used for this purpose. The strain energy function was derived in the form of convolution integral.

Micromechanical analysis has been used to find the anisotropic response of the brain white matter. The studies in this area were inspired by the micromechanical study of composite materials [121, 122]. Abolfathi et al. [99] found the anisotropic properties of brain white matter through micromechanical analysis. A viscoelastic constitutive model which is appropriate for small deformation was used with Prony series expansion to account for time-dependent properties of both axons and ECM as constituents of the brain white matter. To obtain all the anisotropic coefficients of the linear viscoelastic model, six different simulations including three uniaxial tensile loading in three different direction and three simple shear tests were performed by the means of finite element simulations. In their study, the material properties of axons and ECM were obtained from another published papers [98]. Moreover, the effects of axons undulation and volume fraction on the overall properties of brainstem were studied as well. Nonlinear modeling of brain white matter was the target of study in the paper of Karami et al. [100]. Using the mechanical properties of axons and ECM from [3], the mechanical response of brain white matter was found for large deformation cases by the assumption of isotropic behavior of brain white matter.

The mentioned studies in the the micromechanical analysis were aimed at finding the mechanical response of the homogeneous brain white matter by knowing the mechanical properties of heterogeneous representative volume element (RVE) constituents. However, as mentioned in [99], the availability of the experimental data to calculate the properties of micro-level constituents is a point of challenge since experimental techniques such as nanoindentation [123] and atomic force microscopy (AFM) [124] can be quite complex and laborious in terms of design of experiments and sample preparation of soft biological tissues. On the contrary, the macro-level tests such as uniaxial loading tests can be done with much lower cost and with higher availability and accessi-

bility. Therefore, several studies aimed at finding the mechanical properties of brain white matter micro-level constituents (including axons and ECM) by using the experimental data of macro-level tests performed on brain white matter. To this end, simulation-based optimization by finite element modelling has been extensively used in different fields [59, 60] including the biomechanical engineering. Javid et al. [2] tried to find the mechanical properties of axons and ECM of the porcine brainstem through relaxation tensile tests for up to 5% of deformation. The viscoelastic constitutive model was used for both axons and ECM in micromechanical simulations. Applying the averaging technique for homogenization, they minimized the difference between micromechanical simulations and experimental results through conducting iterative finite element simulations. Moreover, the effect of different types of RVE including hexagonal, square, and randomly distributed were studied as well. The obtained results showed good agreements between micromechanical simulation and experimental data. While the viscoelastic model can only be used in the cases associated with small deformation, it still captures the time-dependent response of the brain. Yousefsani et al. [36] used an embedded element technique to perform transverse-plane hyperelastic micromechanical simulation of brain white matter. The RVE used in their study was formed by probabilistic distribution of axons embedded in ECM. Directional dependency was observed in transverse plane loading mode.

4.2. Materials and methods

In this section, first, the constitutive models used for describing the behavior of brain tissue will be explained. Thereafter, the details on the micromechanical simulation methodology will be delineated and finally, the developed simulation-based optimization framework used for micro-level characterization of human brain white matter will be investigated.

4.2.1. Material constitutive modeling

The Ogden hyperelastic model has been extensively used for describing the behavior of rubber-like materials and soft tissues including brain. The Ogden strain energy function can be written as the following:

$$W_{ogden} = \sum_{i=1}^{N} \frac{2\mu_i}{{\alpha_i}^2} \left({\lambda_1}^{\alpha_i} + {\lambda_2}^{\alpha_i} + {\lambda_3}^{\alpha_i} - 3 \right) \tag{4.1}$$

where λ_1, λ_2 and λ_3 denote the principal stretch values, μ_i and α_i are Ogden material parameters, and N is the number of terms used in the Ogden model. As expected, increasing the number

of terms (N) in the Ogden model will consequently increase the accuracy of curve fitting to the experimental data. However, as demonstrated in various studies, using one term will be sufficient most of the time, which is the case in our study as well.

Relaxation test is one of the most common types of tests used for characterizing the time-dependent behavior of soft materials [54,55,125]. Soft materials such as brain, exhibit time varying stiffness when being held under specific deformation for a period. As brain is subjected to constant deformation, the induced stress value drops over time. As a result, a time-dependent model is required to express such a behavior. Miller et al. [52] proposed the following strain energy function for soft biological tissues. While this strain energy function was originally used to describe the behavior of brain tissue in tension, there is no inherent loading mode specific constraint involved and it has been utilized successfully for the compression mode as well [4,53].

$$W = \frac{2}{\alpha^2} \int_0^t \left[\mu\left(t-\tau\right) \frac{d}{d\tau} \left({\lambda_1}^{\alpha} + {\lambda_2}^{\alpha} + {\lambda_3}^{\alpha} - 3 \right) \right] d\tau \tag{4.2}$$

As stated in equation 4.2, convolution integral is employed for formulation of the strain energy function. The term μ which represents the relaxed shear modulus, is calculated based on the following equation:

$$\mu = \mu_0 \left[1 - \sum_{i=1}^{n} g_i \left(1 - \exp\left(-t/\tau_i\right) \right) \right] \tag{4.3}$$

where μ_0 is the instantaneous shear modulus, g_i is the relaxation coefficient, t denotes the time, and τ_i is the characteristic time coefficient. n is the number of terms utilized in the Prony series expansion and usually two terms ($n = 2$) can provide a good approximation.

4.2.2. Micromechanical modeling

Micromechanical modeling studies the materials at the scale of their constituents by using a heterogeneous RVE, hence, providing an insight into stress and strain distribution at the micro-level. The key idea behind micromechanical modeling is to find the heterogeneous RVE that can represent the whole structure of macro-level homogeneous material. The concept of the micromechanical modeling has been tested in the analysis of composite materials [96,97,126,127]. Brain white matter has a fibrous structure with the axons highly oriented and dispersed in the ECM material. The axons stem surrounded by myelin, also known as nerve fibers, are highly oriented. Therefore, attempts

have been made to model the brain white matter as a fibrous composite structure. From one point of view, the research in this area can be divided into two separate categories. One contains the studies that are aimed at finding the material properties of brain white matter when the properties of its constituents are known [99, 100]. Second category includes those studies conducted to find properties of brain white matter constituents from known response and mechanical properties of the brain white matter [2, 36] through macro tests.

The first step toward micromechanical analysis is to identify the appropriate RVE. This is usually done through microscopic images of materials, which shows the micro-level structure, the volume fraction of each constituent, and geometrical shape of them. The scanning electron microscopy (SEM) images of porcine brainstem [2] and histology slide of guinea pig optic nerve [3] can be seen in Figure 4.1(a) and Figure 4.1(b). These figures can be used for estimating the volume fraction of axons and verifying their orientation in the matrix. As it can be seen in Figure 4.1(a), the axons vary in diameter size, and show random distribution. While it seems that the most realistic representation of RVE can be created by considering this randomness, different independent studies [2, 100, 108] confirmed that simplified representation of RVE with uniform diameter of axons and organized dispersion structure can lead to results just as accurate as the more complicated randomly dispersed RVE. Moreover, using random RVE has its own challenges, since the meshing in RVE must be completely symmetrical with respect to all coordinate axis, which would be almost impossible for random RVEs. In this study, the square RVE as shown in Figure 4.1(c) is employed. To make representation of a whole brain white matter possible, certain equations need to be applied on the meshed RVE. These equations that ensure the repetition of RVE in all directions are known as the periodic boundary conditions (PBC) and must be applied as constraints to the meshed RVE in the finite element simulations, for which the readers are referred to second chapter of this dissertation.

As mentioned, applying PBC, makes RVE to repeats and extends itself in all directions, thus, the RVE represents a small point in macro sized material, and this is the key idea behind the micromechanical analysis. The RVE can then be used in different finite element simulations of interest including relaxation test which is used in this study. For homogenization purposes, the

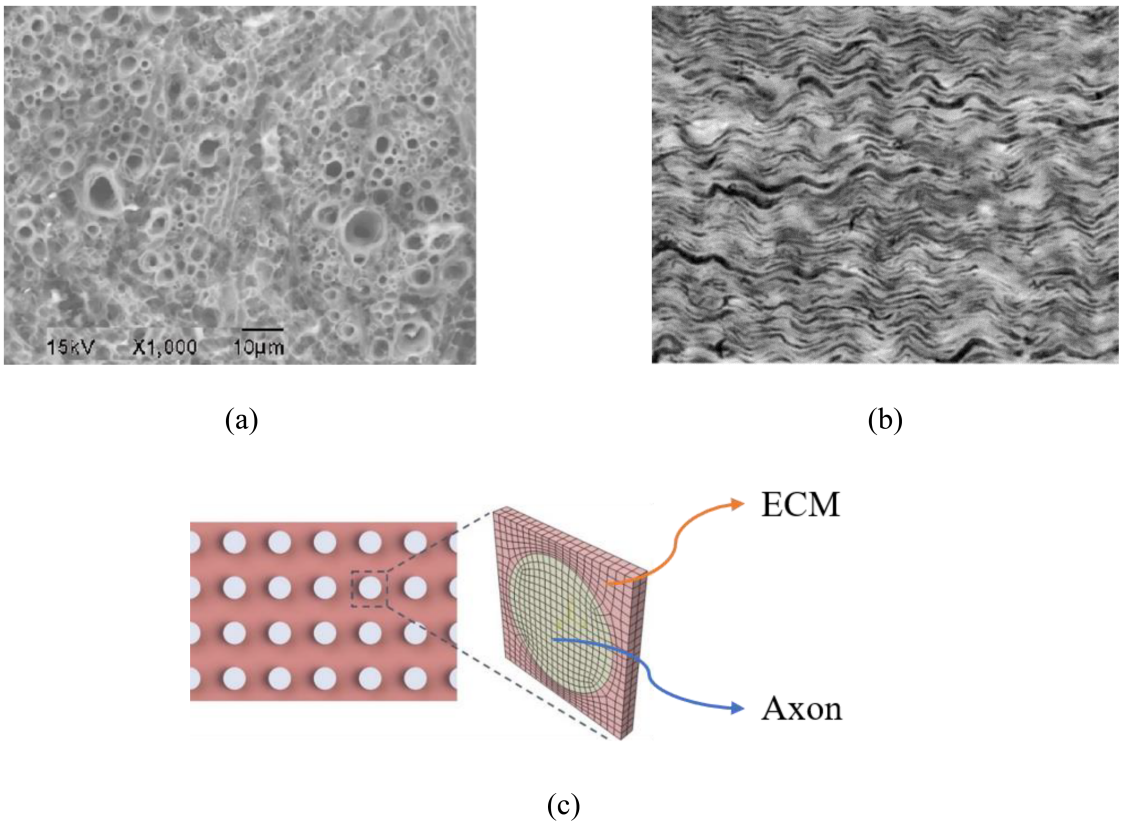

Figure 4.1. The overview of tissues with nerve fibers structure (a) porcine brain stem scanning electron microscopy (SEM) showing dispersion of axons in ECM [2] (b) immunohistochemistry of the guinea pig optic nerve [3] (c) the square RVE for representing the patterned structure of brain white matter and other tissues with oriented dispersion of axons and nerve fibers.

macro-level stress and strain will be found by volume averaging of the micro-level stress and strain fields over the RVE, based on the following equations:

$$\overline{\sigma} = \frac{1}{V}\sum_{i=1}^{m} \sigma_i v_i, \quad \overline{\epsilon} = \frac{1}{V}\sum_{i=1}^{m} \epsilon_i v_i \tag{4.4}$$

where σ_i , ϵ_i, and v_i denotes the stress, strain and volume of the i^{th} element of the meshed RVE, respectively, and V the is total volume of the RVE.

4.2.3. A framework for the visco-hyperelastic simulation-based optimization

Time-dependent characterization of human brain white matter has been performed for different parts of the brain [47]. However, there is no similar experimental data for dynamic behavior of micro-level constituents of brain white matter. Using derivative-free optimization methods in the context of micromechanical finite element modeling, the goal is to find the visco-hyperelastic

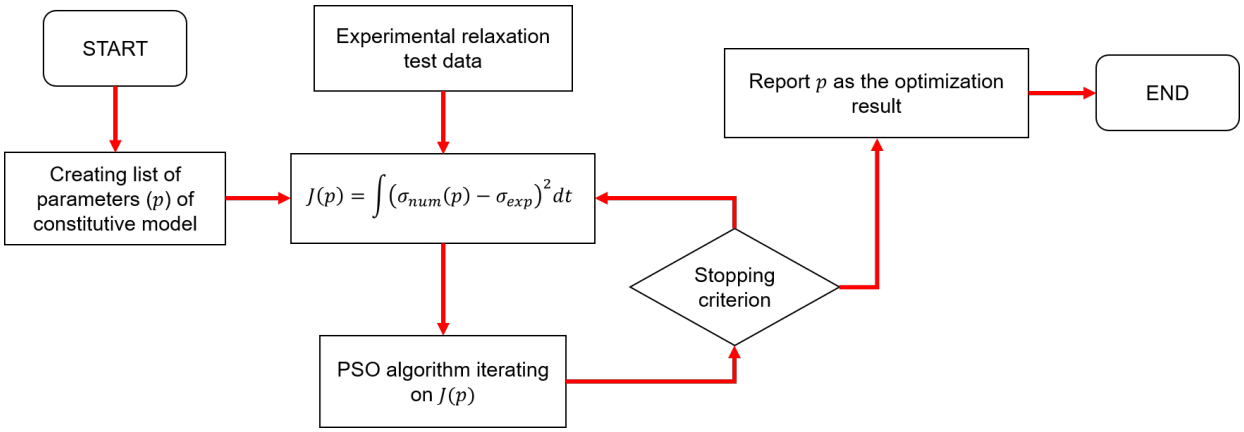

Figure 4.2. The flowchart of the optimization framework for finding the parameters of brain white matter constituents.

properties of axons and ECM. The key idea is the fact that if right material properties are chosen for those constituents, the overall response of brain white matter obtained from micromechanical finite element modeling will be close to that of the experimental relaxation tests. To this end, an iterative optimization framework must be defined which changes the material properties of constituents until the desired results will be obtained. The schematic representation of the optimization framework is shown in Figure 4.2. In Figure 2, $J(p)$ is the objective (cost) function which is dependent to the parameters of the visco-hyperelastic model including μ, g_i, and τ_i introduced in equation (4.3). These parameters must be separately assigned to both constituents of the brain white matter. Therefore, the number of parameters in the constitutive model doubles up in the objective function to account for the material properties of both axon and ECM. Consequently, the following cost function is defined to perform the optimization procedure in the context of iterative finite element simulation.

$$J(p) = \int_{t_1=0}^{t_2=500s} [\sigma_{FE}(p,t) - \sigma_{\exp}(t)]^2 \tag{4.5}$$

in which J denotes the cost function, σ_{FE} represents the averaged stress values obtained from the numerical micromechanical finite element simulation, t is the time, p represents the independent variables on which the cost function (and hence, numerical simulated stress) is dependent on (listed in Table 4.1) and σ_{exp} denotes the experimental stress corresponding to the data presented in Figure 3 and Figure 4 appearing in the subsequent section of this thesis.

Table 4.1. List of the arguments p in the cost function defined in equation (5) which correspond to the constitutive model described in equations (4.1) to (4.3).

Axon	ECM
μ_0,α,g_1, g_2,τ_1,τ_2	μ_0,α,g_1, g_2,τ_1,τ_2

As listed in Table 4.1, total number of 12 variables control the finite element obtained stress values which consequently, the cost function will be dependent on. Moreover, the following constraints must be held between the variables for both axons and ECM:

$$g_1 + g_2 < 1 \tag{4.6}$$

$$\tau_1 - \tau_2 < 0 \tag{4.7}$$

Different derivative-free optimization algorithms can be used for the proposed optimization framework in Figure 4.2 [128–130]. In this part, the constrained particle swarm optimization (C-PSO) algorithm. The C-PSO algorithm is widely used for black-box optimization problems where the function of interest is not explicitly stated in terms of its independent variable or when the function is time-consuming to be evaluated. PSO algorithm was originally introduced by Kennedy and Eberhart [131]. In PSO, several particles are randomly placed in the search domain of the objective function. The search domain is n-dimensional space where n denotes the number of variables associated with the objective function. For the initial iteration, each particle will be randomly located in the search space and objective function will be evaluated at those points. In the next iterations, the particles will displace themselves in the search domain by using the information from the history of their own and the communicative information acquired from other particles in the swarm. This process continues until the whole swarm is converged i.e., gets very close to a specific point in the search domain. This point is the optimum solution to the objective function. The swarm particles update their trajectory based on the following equations:

$$\overrightarrow{v_i}^{k+1} = \overrightarrow{v_i}^{k} + c_1 r_1 \left(\overrightarrow{x_{*i}}^{k} - \overrightarrow{x_i}^{k} \right) + c_2 r_2 \left(\overrightarrow{x_g}^{k} - \overrightarrow{x_i}^{k} \right) \tag{4.8}$$

$$\overrightarrow{x_i}^{k+1} = \overrightarrow{x_i}^{k} + \overrightarrow{v_i}^{k+1} \tag{4.9}$$

In the above equations, k denotes the iteration number, $\overrightarrow{v_i}^{k}$ represents the velocity of the i^{th} particle, $\overrightarrow{x_g}^{k}$ is the global best location experienced by the whole swarm in the k^{th} iteration, $\overrightarrow{x_{*i}}^{k}$ denotes the best location experienced by the i^{th} particle up to the k^{th} iteration, r_1 and r_2 are uniform random numbers, and finally c_1 and c_2 are constant coefficients which can be adjusted from problem to problem. Commonly $c_1 = c_2 = 2.05$ is employed in this implementation of PSO. The second and third terms on the right-hand side of equation (4.8) qualifies the cognitive and social behavior of particles in their search process and therefore, the choice of c_1 and c_2 affects the weights of these terms in evolution of particles and balances the self-learning and swarm-learning effects. Usually, boundaries can be set up for the search space domain, and therefore, the velocity quantity must be bounded as well. Restricting the velocity of particles, however, can slow down the process of convergence, but it helps to avoid the divergence of particles. It should be noted that while mostly in the literature and particle swarm optimization terminology, the term $\overrightarrow{v_i}$ is referred to as the velocity of the particles, it is in fact, a type of displacement and corresponds to the displacement of a particle in the two consecutive iterations. To be consistent with the literature, this term will be mentioned as velocity in this dissertation as well.

As can be speculated from Equation (4.8), all the particles are learning from the swarm by moving toward the global best experienced location. Therefore, there is a probability that all or a majority of particles will be attracted to the global best point and get stuck in the local optimum of the objective function. Linearly decreasing weighted PSO, balances the local and global search properties of the swarm by applying a decreasing weight on the velocity of the particles from previous iteration as stated in the following equations [82]:

$$\overrightarrow{v_i}^{k+1} = \omega \overrightarrow{v_i}^{k} + c_1 r_1 \left(\overrightarrow{x_{*i}}^{k} - \overrightarrow{x_i}^{k} \right) + c_2 r_2 \left(\overrightarrow{x_g}^{k} - \overrightarrow{x_i}^{k} \right) \tag{4.10}$$

$$\omega = \omega_{max} - (\omega_{max} - \omega_{min}) \frac{k}{k_{max}} \tag{4.11}$$

where k denotes the current iteration number in the optimization iterative process, k_{max} is the maximum number of iterations, ω_max and ω_min are the upper and lower boundaries imposed on the ω which is the PSO velocity relaxation coefficients. In this study, the values of ω_max and ω_min was set to be 1.1 and 0.1, respectively. This way, the search procedure will be more inclined to global exploration in the initial iterations and more to the exploitation as the number of iterations increases.

It is worthy to mention that other derivative-free algorithms such as genetic algorithm or pattern search algorithm can be used for optimization process as well. However, the gradient based optimization algorithms such as gradient descent may fail to provide a reasonable approximation since they can get stuck in the local minimum of the optimization problem [26]. The derivative-free optimization algorithms get around this problem and are more likely to find the global minimum. However, in this part, the C-PSO algorithm is used and will be employed the optimization problem by imposing the constraints stated in equations (4.6) and (4.7). For more details on the C-PSO, how to configure it for imposing the constraints of the optimization problem, and on its modification for faster convergence, readers are referred to [26, 28].

4.3. Results

In this section, first, the results from micro-level characterization of brain white matter in different strain rates will be presented. Thereafter, the possibility of generalizing the material properties of axons by studying its dependency to the strain rate will be studied.

4.3.1. Micromechanical optimization of the constituents' properties

The relaxation compression tests at different strain rates conducted in [4] were used as the input data for the optimization procedure. Based on [4], stress relaxation test on the brain white matter was performed by holding the sample at the compressive stretch value of $\lambda = 0.7$ (corresponding to the compressive strain value of 0.3) for the duration of 500 seconds. The finite element simulation of compression relaxation test was created in ABAQUS (ABAQUS Inc., Providence, RI) with the same deformation speed and relative sample size as that of the [4] by use of the meshed RVE introduced in previous sections. Figure 4.3 and Figure 4.4 show the ramp and relaxation part of the relaxation tests performed by Forte et al. [4].

Using curve fitting techniques by the C-PSO algorithm [26], the visco-hyperelastic material parameters of the brain white matter are found to be as presented in Table 4.2.

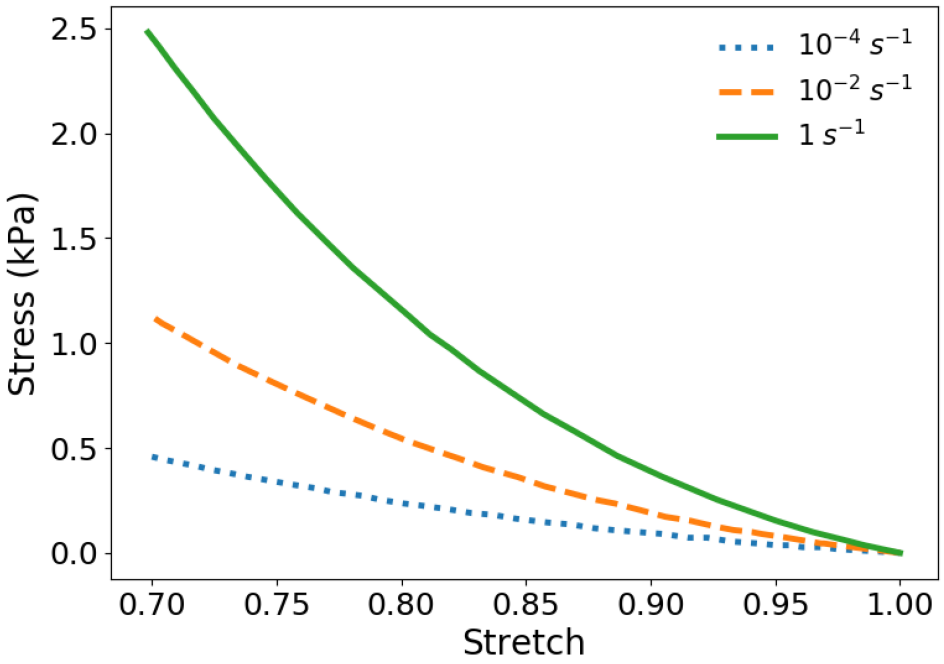

Figure 4.3. The ramp part of the relaxation test at different strain rates of 0.0001, 0.01, and 1 s^{-1} obtained from [4]. As can be seen, the stiffness of the tissue increases with the increase in the strain rate value.

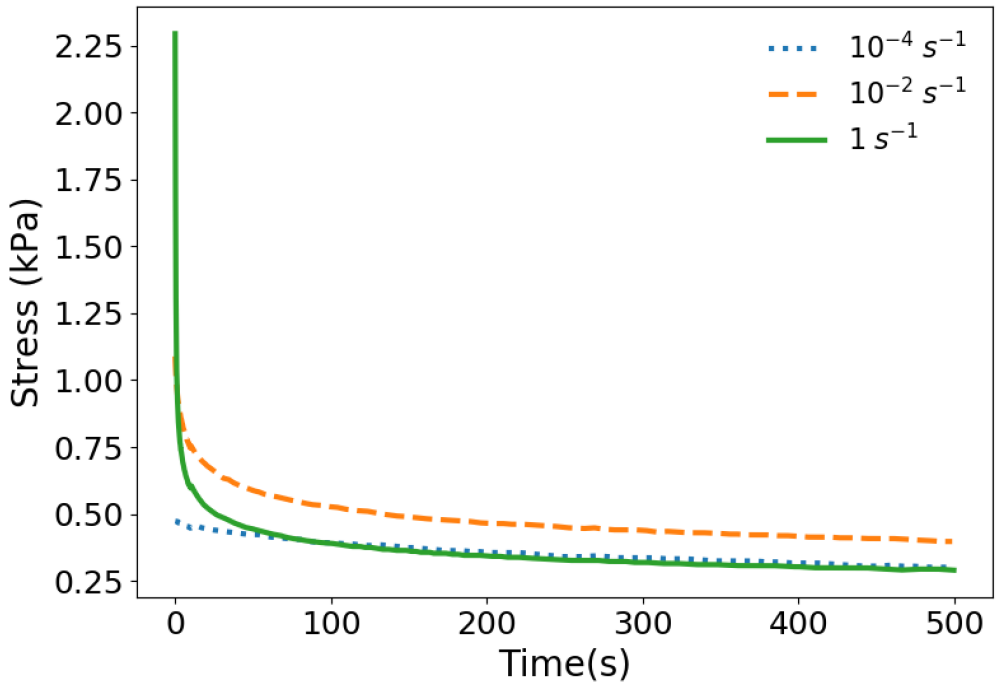

Figure 4.4. The compression relaxation test data of Forte et al. [4] at the stretch value of $\lambda = 0.7$. The relaxation test is done by holding the sample for 500 s. The points in the original paper are digitized through image processing techniques.

Table 4.2. Visco-hyperelastic material properties of brain white matter using the experimental data presented in Figure 4.3 and Figure 4.4.

Strain rate (1/s)	μ_0 (kPa)	α	g_1	g_2	τ_1 (s)	τ_2 (s)
0.0001	0.2751	-3.4996	0.172	0.256	123.348	441.027
0.01	0.5669	-4.5181	0.303	0.326	2.240	71.522
1.0	1.1783	-4.7659	0.653	0.206	0.448	15.007

Table 4.3 and Table 4.4 list the obtained optimal material properties for axons and ECM after conducting the particle swarm optimization method. These results are obtained by setting the volume fraction of axons in RVE, equal to 0.527 and the ratio of initial shear modulus of axon to the initial shear modulus of ECM equal to 3.0 ($\mu_{0_{axon}}/\mu_{0_{ECM}} = 3.0$). It should be noted that it is vital to impose the ratio of the initial shear modulus as a constraint into the optimization framework. Otherwise, the material properties of axon and ECM will be the same as the material properties of the brain white matter itself and the defined cost function stated in equation (4.5) will be exactly zero corresponding to its global minimum.

Table 4.3. The optimal material properties for axons with respect to the compression relaxation test.

Strain rate (1/s)	μ_0 (kPa)	α	g_1	g_2	τ_1 (s)	τ_2 (s)
0.0001	0.4018	-3.4258	0.184	0.293	121.546	438.412
0.01	0.8280	-4.6221	0.4430	0.2431	4.2587	72.200
1.0	1.7210	-4.7549	0.651	0.219	0.398	16.259

Table 4.4. The optimal material properties for ECM with respect to the compression relaxation test.

Strain rate (1/s)	μ_0 (kPa)	α	g_1	g_2	τ_1 (s)	τ_2 (s)
0.0001	0.1339	-3.4346	0.176	0.285	123.530	441.235
0.01	0.2760	-4.7330	0.310	0.335	2.539	70.326
1.0	0.5737	-4.8021	0.634	0.219	0.463	16.008

Figure 4.5 demonstrates the averaged mechanical response of RVE in micromechanical finite element simulation using the acquired optimal material properties of axons, compared with the experimental data from the compressive relaxation test for three different deformation strain

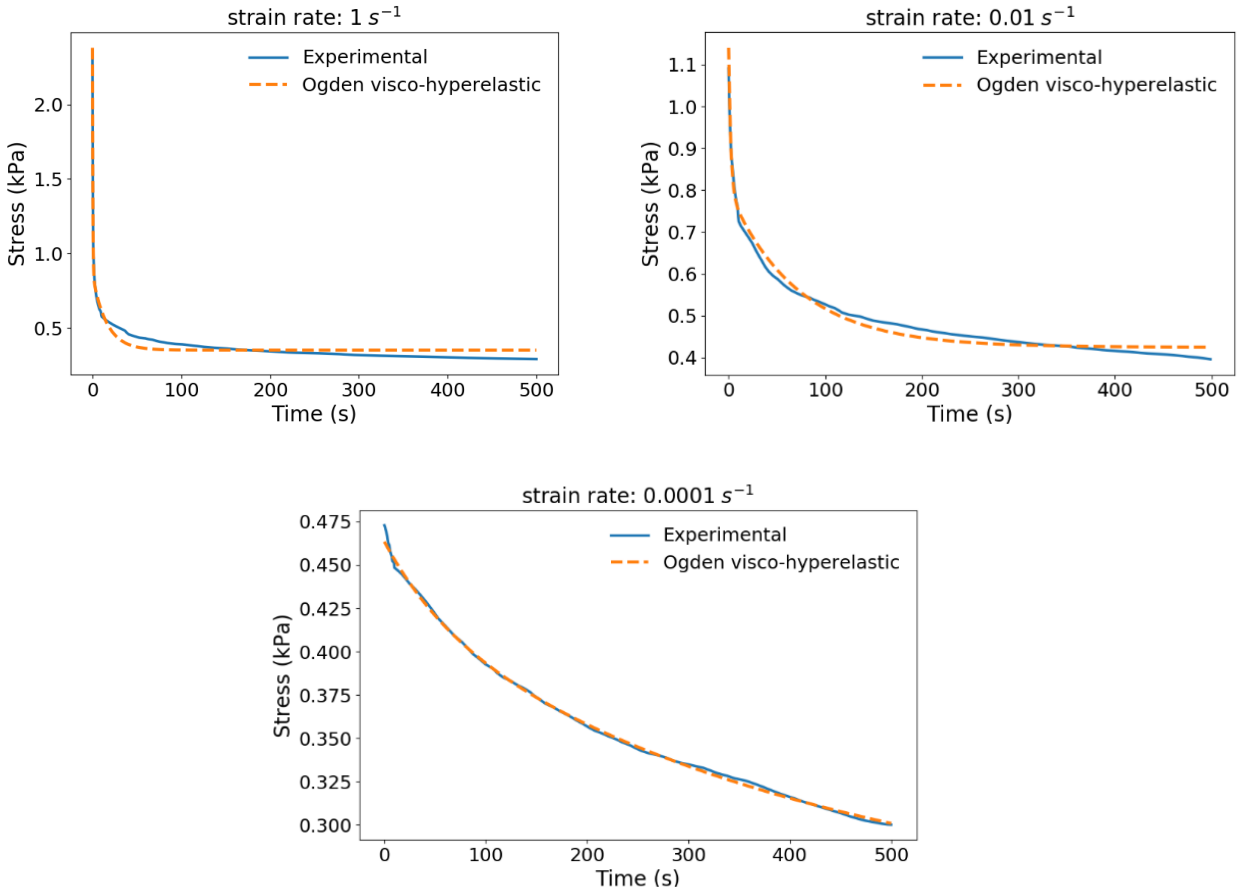

Figure 4.5. Comparison of the experimental results of relaxation test on human brain white matter [4] and the obtained numerical results of micromechanical finite element simulation by using the acquired optimal parameters of axons and ECM presented in Table 4.3.

rates. As it can be seen, good agreement is observed which implies on the success of our proposed optimization framework. The cost function J has the value of 0.0248, 0.0359, and 0.0199 for three strain rates of 0.0001, 0.01 and 1 s^{-1}, with the acquired optimal parameters and the coefficient of determination comparing the numerical micromechanical results with experimental result stand at high values of $R^2 = 99.59\%$, $R^2 = 99.14\%$, and $R^2 = 99.45\%$ which again confirms the high accuracy of the resultant optimization process and micro-level constituents' characterization of human brain white matter. Figure 4.6 shows the relaxed stress of axons and ECM with respect to time. Since the obtained Prony series parameters of axon and ECM are close to each other, the overall pattern of Ogden shear modulus reduction for both materials seems to be nearly identical. Both axon and ECM experience more than 50% reduction in the shear modulus compared to the initial shear modulus expressed by Ogden constitutive model.

4.3.2. Strain rate dependency of the axons material properties

In this section, the aim is to correlate the material properties of axons with respect to the deformation strain rate. In Figure 4.7, the obtained initial shear modulus of axons is depicted with respect to the strain rates of the compression tests. As represented in Figure 4.7, if logarithmic scale is used for demonstration of strain rates values, a linear relationship is observable between the strain rate and the axons initial shear modulus. To predict the initial shear modulus of axons with respect to the strain rate, a linear regression is performed, and the predicted initial shear modulus of axons is also represented in Figure 4.7 by a solid line. The prediction line can be stated by the following equation:

$$\mu_0\,(kPa) = 0.1432 \ln(\dot{\epsilon}) + 1.6432 \tag{4.12}$$

Moreover, finding the reduced shear modulus of axons can be of interest as well. Figure 4.8 shows the reduced shear modulus of axons at $t = 5s$. The linear pattern seen for the initial shear modulus is not observable here anymore. The maximum reduced shear modulus after 5 s is seen for the strain rate of 0.01 s^{-1}. The following equations state the first and second order regression for predicting the reduced shear modulus of axons for the intermediate strain rate values, respectively.

$$\mu_5\,(kPa) = 0.0112 \ln(\dot{\epsilon}) + 0.5381 \tag{4.13}$$

$$\mu_5\,(kPa) = -0.0053(\ln(\dot{\epsilon}))^2 - 0.0374 \ln(\dot{\epsilon}) + 0.5008 \tag{4.14}$$

where μ_5 stands for the reduced shear modulus of axons at $t = 5s$.

Figure 4.9 demonstrates several micromechanical finite element simulations with the obtained optimal parameters for the strain rate of 1 s^{-1}, shown at different times of 1 s, 10 s and 25 s. These simulations can provide us with a detailed understanding of the stress distribution at the micro-level. In this case, where the uniaxial compression relaxation test is performed, the stress is uniformly distributed in the axon and ECM, with the stress of axons being approximately 3 times greater than that of the ECM. This is true for the three shown instances, since the Prony series expansion parameters for both constituents are close to each other.

4.4. Discussion

To bridge between the micromechanical simulations and the macro-level tests, and to plausibly find the micro-level constituents, the micromechanical simulation and macro-level tests must be in high degree of resemblance to each other. One point that may raise concerns upon the validity of the micromechanical simulation is the orientational dependency of the brain white matter stiffness. Forte et al. paper [4] from which the experimental data was obtained, does not concern itself with the orientation of the axonal fibers in the brain white matter samples for the uniaxial tests and this seems to be a reasonable approximation and approach; since Budday et al. [1] performed uniaxial tests in different axonal fiber orientations and they posited that there is no statistically significant dependency between the shear modulus of axons and the axonal fiber orientation. Hence, in this study, the micromechanical simulation and uniaxial loading is performed along the direction of the axonal nerves while using the macro-level compression test data from Forte et al [4], on the premise of the conclusion asserted by Budday et al [1], as explained. Moreover, the no-friction boundary condition of the uniaxial testing was considered in our micromechanical simulations as well.

There is a wide range of reported properties for axons in different biological tissues as can be found in the literature. The reported initial shear modulus of axons in guinea pig optic nerves, using the Ogden hyperelastic model by Meaney [3] was in the range of 0.28 to 0.29 kPa. The initial shear modulus of axons in porcine brainstem under tensile test with the strain rate of 5.5 s^{-1} was found to be approximately 12.9 kPa, as reported by Javid et al. [2]. In this study, this value was found to be in the range of 0.4 to 1.7 kPa for axons of human brain white matter under compression. This variation may be originated from difference in tissues used for experimental tests, regional variation, load dependency, strain rate dependency, and the employed constitutive models. The degree of dependency of the axons shear modulus to the strain rate of deformation was found to be notable, showing 4.5 times increase as the strain rate rise from 0.0001 to 1.0 s^{-1}.

The quality of the first and second order regression for approximating the initial and reduced shear modulus of axons is another point which deems to be worthy of discussion. Looking into Figure 4.8, it can be elicited that the first order regression with the independent variable of $ln(\dot{\epsilon})$, as reflected in equation (4.13), could not give a good approximation of reduced shear modulus of axons (at t = 5s) for the intermediate range of strain rates. Alternatively, the second order regression

as stated in equation (4.14) can be used for approximating purposes, however, it should be noted that we should be cautious when using this equation for finding the reduced shear modulus in the strain rates outside the range of 0.0001 s^{-1} to $1s^{-1}$. In other words, extrapolation may lead to far inaccurate and irrational approximations. Moreover, since the regression is built upon 3 points, the second order regression will be identical as the second order interpolation and the associated error of prediction will be zero, which could result in overfitting and inaccurate results if used for the ranges of the strain rate beyond what was discussed here. Therefore, a great care should be taken upon the decision of whether using the first or second order regression for approximating the reduced shear modulus of axons in the intermediate strain rate values.

The resultant material properties for axons and ECM are dependent to some of the assumptions made in the optimization framework including the axons volume fraction and the ratio of the initial shear modulus of axons to ECM. As mentioned earlier, there must be a fixed initial shear modulus ratio, to carry on the optimization procedure since if the material properties of both axons and ECM are set to equal parameters, the RVE represents a homogeneous material with the property equivalent to that of the assigned ones. The axons volume fraction is another factor that affects the constituents' properties. In this paper, those parameters were assigned based on the previous published studies [2, 100]. However, those values are not specifically derived for human brain white matter tissue, and hence, experimental micro-level tests on human brain white matter could be beneficial for better approximation of that kind.

The utilization of biphasic constitutive models could open a new line of research in the field of micromechanical characterization of the brain [55, 61]. The biphasic model breaks down the brain structure into two independent phases of solid and fluid, as water constitutes 80% of the volume fraction of brain. A recent study involved with macro-characterization analysis, suggests a calibrated shear modulus of 1.8 kPa for bovine brain tissue in three deformation speed of 10, 100, and 1000 mm/s [55]. However, to the authors best knowledge, there is no reported biphasic properties for micromechanical constituents of brain tissue as there are some limitations and hindrances. Due to the lack of specific direct micro-level experimental tests, there are some parameters with unknown values such as hydraulic conductivity, permeability, and water fraction for both axons and ECM. Therefore, besides the added computational complexity to the optimization framework due

to the increased number of parameters, more assumptions will be required to correlate between the properties of those micro-level constituents.

4.5. Conclusion

In this part of the dissertation, a C-PSO algorithm as a derivative free optimization method in conjunction with finite element micromechanical simulation was used to find the visco-hyperelastic material properties of axons and ECM as micro-level constituents of human brain white matter. As brain white matter is a heterogeneous material at the micro-level, consisting of axons embedded in ECM, a sample RVE representing a smallest recognizable unit of brain white matter was developed with the axons volume fraction of 52.7% [2]. The experimental compressive relaxation experiment performed in [4] was used as the input experimental data in this study. The cost function was defined as the sum of the square of error between the finite element and experimental results. Thereafter, a particle swarm optimization algorithm was used to find the optimal material properties of axon and ECM. The Ogden hyperelastic model with Prony time series expansion was used to account for the viscous behavior of the brain in a relaxation test. Comparing the results of the micromechanical simulation carried on with the obtained optimal parameters and experimental data showed a high quality agreement. A high coefficient of determination and low-cost function value proves the validity of the conducted optimization framework. The Prony series expansion parameters of axons and ECM were found to be close to that of the human brain white matter. In addition, the strain rate dependency of the initial shear modulus and reduced shear modulus of axons were studied through first and second order regression. It was shown that linear approximation may not be beneficial for approximating the reduced shear modulus of axons at the intermediate strain rate values. The results of this study can be used for the studies focused on the DAI, drug delivery or any other research which requires the knowledge of the micro-level constituent properties of human brain white matter.

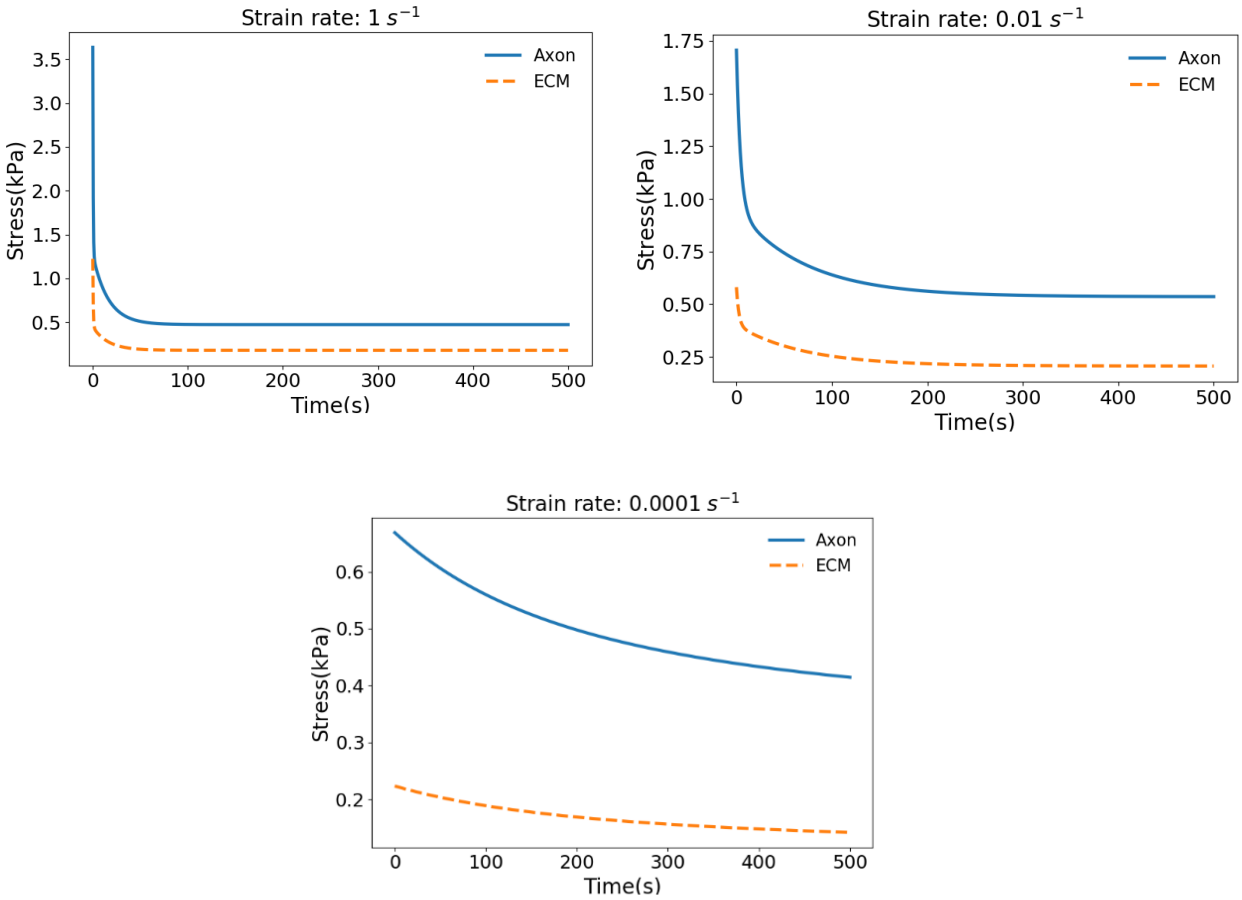

Figure 4.6. Relaxation stress of axon and ECM using the Ogden visco-hyperelastic constitutive model for different strain rates.

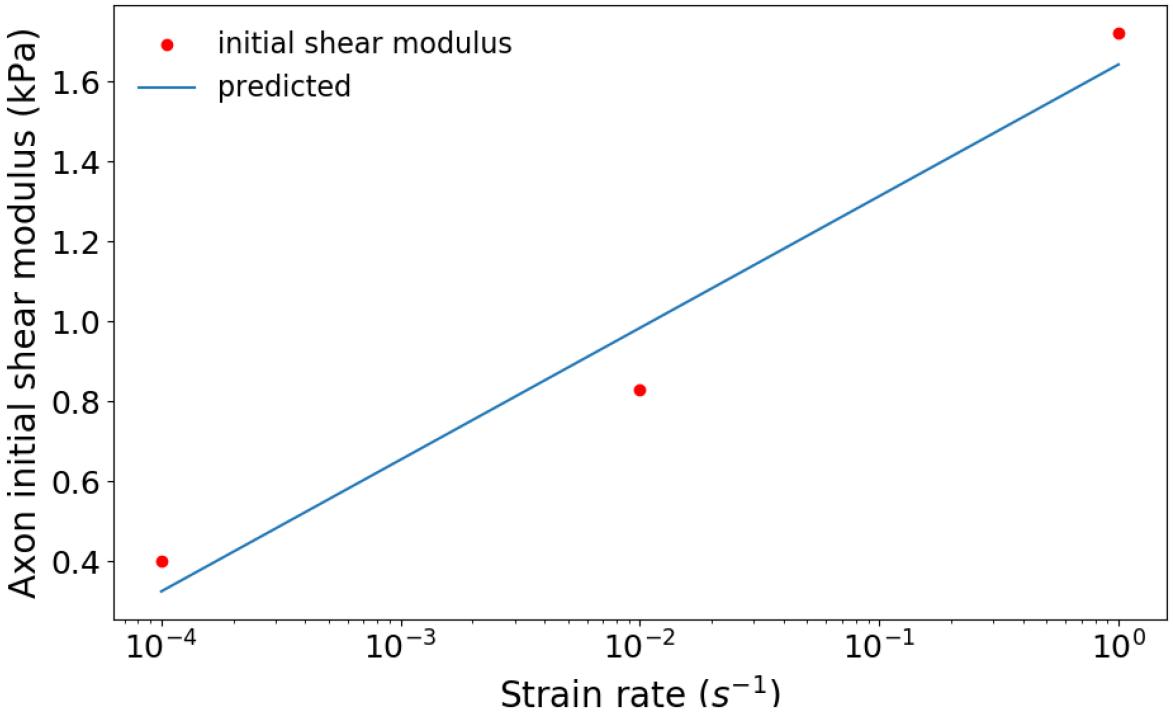

Figure 4.7. The obtained initial shear modulus of axons in different strain rates and the predicted initial shear modulus with respect to strain rate.

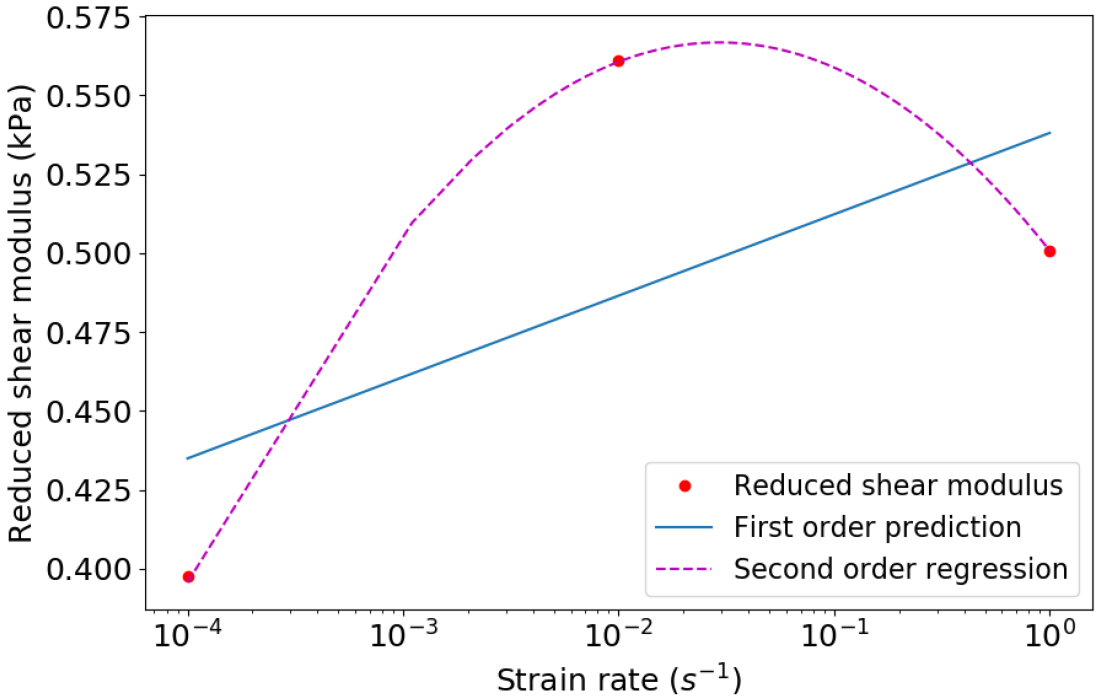

Figure 4.8. The obtained reduced shear modulus of axons at $t = 5s$ for different strain rate values and the corresponding first and second order regression for predicting the reduced shear modulus at intermediate strain rate values.

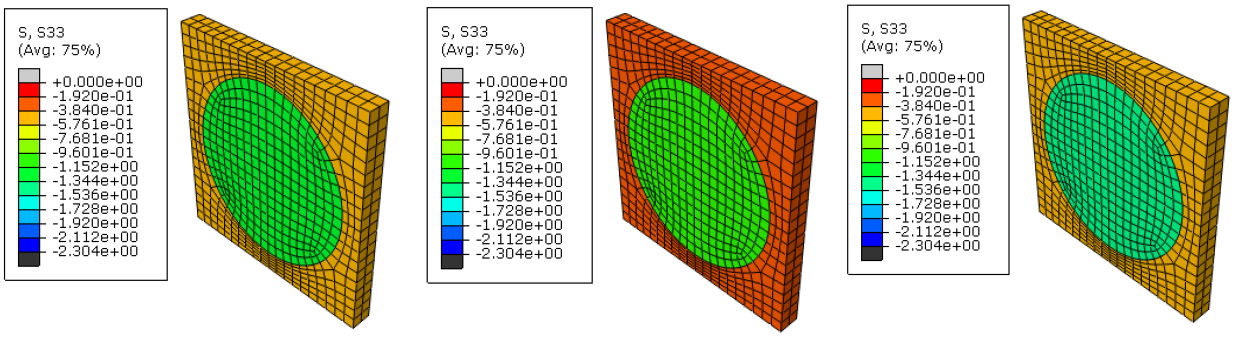

(a) (b) (c)

Figure 4.9. The micromechanical stress distribution in the RVE used for simulating human brain white matter in unconfined compression relaxation test at (a) t = 1s, (b) t = 10s, and (c) t = 25s.

5. ARTIFICIAL INTELLIGENCE BASED APPROACHES FOR QUALITATIVE DESCRIPTION OF TISSUE STIFFNESS FROM MAGNETIC RESONANCE ELASTOGRAPHY SIMULATIONS

5.1. Introduction and literature review

Alongside the development of different imaging techniques for diagnosis of different pathologies in human organs tissues, palpation is still commonly used by physicians to detect the tissues affected by diseases. Generally, the pathologic tissues are prone to have more stiffness compared to normal tissues [132, 133]. MRE is a non-invasive technique used for quantitative and qualitative measurement of tissue stiffness. In MRE, shear waves are generated in the tissue either by mechanical actuation [134] or intrinsic phenomena such as heartbeat rate or respiratory system [135, 136]. The small displacement of the tissue is then visualized by magnetic resonance imaging which in fact depicts the propagation of shear waves in the tissue. Thereafter, the phase contrast sequencing [137] is performed to find either quantitative or qualitative stiffness mapping of the tissue. The stiffness of the tissue and its material property affects the shear wavelength propagating in the tissue. While conventional imaging techniques such as CT-Scan and MRI only provide information on the pathologies affecting the morphological characteristics of the tissue, the MRE goes further by giving additional information on quantifying the stiffness of the tissue. Another advantage of the MRE lies in its capability of in-vivo characterization of the tissue, while other methods are mostly done for in-vitro conditions which may affect the material properties of the tissue being measured post-mortem [44]. While it is theoretically possible to perform in-vivo MRE, due to the difficulties of such an experiment, some of the works in this field are done for in-vitro conditions.

The material in this chapter was co-authored by Mohammadreza Ramzanpour, Mohammad Hosseini-Farid, Mariusz Ziejewski, and Ghodrat Karami. Mohammadreza Ramzanpour was mainly responsible for data collection, analysis, algorithm development, and the conclusions advanced here. The other co-authors helped in proof-reading the paper. Ghodrat Karami supervised the project.

Numerous MRE-based studies have been conducted for brain [43, 138], liver [139–141], trabecular bone [142], and other biological tissues. Kruse et al. [132] used MRE to approximate the shear modulus of in-vivo human brain cerebral tissue. They used an acoustic actuator for vibration of the target tissue and employed a modified gradient echo pulse sequence for MRE acquisition. Using a linear elastic model for finding the stiffness, they concluded that brain white matter is approximately 2.5 times stiffer than brain grey matter. Time-dependent modeling of tissues has also been a point of study where Green et al. [42] tried to characterize the brain by viscoelasticity under in-vivo condition. By using the harmonic excitation, they were able to calculate the viscoelastic parameters of the tissue by solving for a displacement field equation induced by acoustic wave propagation using inversion techniques. Schmidt et al. [143] implemented a transversely isotropic model to analyze the ex-vivo MRE experimental results on porcine brain white matter. Moreover, finite element simulation was conducted to verify their results. For the incompressible transverse isotropic model, 3 parameters are needed to characterize the material behavior. In their study, they found the anisotropic shear properties of porcine white matter by fitting numerical FE simulations to the experimental results in hand. Moreover, good agreement was found with theoretical estimation of shear wave propagation in transverse isotropic material. They concluded that porcine brain white matter is mildly anisotropic in shear.

Chen et al. [45] investigated the effects of material properties, excitation frequency, boundary conditions, and applied tension on the stiffness calculation derived from MRE. Assuming a plane wave condition, linear elastic material model was used for this purpose. Theoretically, in the linear elastic model, the shear wavelength induced in the solid is proportional to the shear modulus of the solid [134]. Performing MRE on agarose gel phantom, they were able to find the shear wavelength by measuring peak displacement values in the excitation frequency of the range 150 to 200 Hz. Finite element model of MRE was used to verify the results from experimental MRE. Good agreement was found between experimental and FE results.

While various studies have focused on the quantitative analysis of the tissue based on different material modeling [144–146], the inversion scheme and solution of the displacement field can be challenging for more advanced constitutive models. Characterization of tissue based on more advanced constitutive models has been done by employing inverse finite element analysis and comparison of the numerical displacement of the tissue and experimental results [143, 147] of the MRE

and observing the induced shear wavelength. Moreover, in some cases the exact stiffness of the tissue is not required in the clinical processes and the comparative stiffness of the tissue could be useful in diagnosing the pathological effects as well [148]. Moreover, a quick estimation of the tissue stiffness can be useful in clinical procedures as well. To this end, simulation-based optimizations [25,59] have been widely used for material characterization in different fields. These optimization techniques are mostly time consuming and therefore are not beneficial in cases where quick decision-making process is important. In this part of the dissertation, a new statistical framework is introduced for categorizing the stiffness of the tissue by numerical MRE simulation. We will show that considering the shear wavelength as the sole factor for parameterizing the tissue stiffness would not be effective and nodal displacement at different cycles of the induced harmonic displacement will be used instead. The effect of different constitutive models on the pattern of the induced harmonic displacement in the tissue will be discussed as well in this paper.

Upon the development of artificial intelligence and machine learning approaches in different fields of engineering and science, they have found their ways into the biomechanical and biomedical research as well. Liang et al. [149], employed artificial neural networks (ANN) as a FE surrogate for estimating stress distribution on heart aorta. Using statistical shape model, they generated 729 FE model of aorta with different geometrical parameters, and the FE simulations were performed to obtain the corresponding stress distribution. In the first step of their proposed DL pipeline, shape decoding is done through the use of an ANN which encodes a 5000 node FE model into three nodes. Thereafter, the shape encoded FE model is employed within the context of another multilayer neural network with two hidden layers to find the stress code which will be subsequently used to find the stress distribution. Their trained DL pipeline was capable of predicting the stress distribution with the average error of 0.492% and 0.891% in terms of he Von-Mises and peak Von-Mises stress, respectively.

Murphy et al. [150] explored finding the stiffness of brain tissue using neural network inversion (NNI) algorithm. Training of the NNI was done on 5×5×5 3D patches with 3-mm isotropic voxels. The stiffness of the tissue was varied in the range of 0.1 to 5 kPa and the wave source varying from 1 to 10 randomly located in a spherical shell. They used 54 features as an input of their brain-NNI model including the real and imaginary parts of the first harmonic displacement data.

Good agreement was seen between the NNI and direct inversion (DI) algorithm with the coefficients of determination R^2 evaluated as 0.974 and 0.915 for brain and liver tissues, respectively.

Scott et al. [151] used ANN for estimating the tissue stiffness from MRE simulation data on inhomogeneous materials on the notion that consideration of inhomogeneity will yield a better spatial stiffness estimation accuracy. They used coupled harmonic oscillators to generate three-dimensional displacement map dataset. Smooth variation in spatial material properties were implemented in the material. The curl of the wave field was used as an input to the ANN model as each simulation consisted of a 16×16×16 patch of isotropic voxels. They were able to demonstrate the higher efficiency of the ANN approach compared to finding the stiffness with homogeneous assumptions using DI algorithms.

In this paper, in addition to the stiffness of the tissue, other material properties of the tissue including Poisson's ratio, and density will be varied in different FE simulations. While these parameters are used for generating the simulation dataset, they will not be used as an input feature for the prediction phase.

5.2. Methodology

In this section, first, the finite element model used for simulating the MRE process will be described. Then, the machine learning and deep learning algorithms used for building the statistical inference frameworks including logistic regression and convolutional neural networks will be delineated.

5.2.1. Finite element simulation

The propagation of the shear wave in the tissue depends on the material properties and stiffness of the tissue. Shear waves can be generated by applying a harmonic displacement in the tissue. In this study, an axi-symmetrical model is created in finite element package ABAQUS/Standard 2016 (ABAQUS Inc., Providence, RI) as shown in Figure 5.1. The model is 200 mm in width and 20 mm in height and it is meshed with a total number of 561 nodes and 500 quad elements of the type 4-node bilinear axi-symmetric quadrilateral, with reduced integration and hourglass control. Upon guaranteeing the stability of the model, the bottom edge of the model is fixed in the vertical direction. Chen et al. [45] has validated this finite element model using experimental MRE results. A harmonic displacement with an amplitude of 1 mm and a frequency of 200 Hz is applied to the center of the model governed by the equation $D_h = 0.001cos(400\pi t)$ where D_h stands for the har-

monic displacement in meters, t denotes time in seconds, and the 400π corresponds to the circular frequency.

In the first step, the first 20 modes of the natural frequency of the created FE model are calculated using Block-Lanczos eigen-solver [152] and in another step, a transient dynamic modal analysis simulation is performed upon the application of harmonic displacement which runs for 10 ms corresponding to the completion of two complete cycles of the displacement. The time step of the transient dynamic modal analysis was set to be 0.1 ms. Upon the completion of simulations, a subroutine script is executed to capture the vertical displacement of all nodes of the model at different time steps of the simulation. This data can be used for finding the shear wavelength and patterns of displacement of the nodes in the model.

The controlling parameters in the simulation are stiffness, density, and the Poisson's ratio. The density was changed from 1040 kg/m^3 to 1050 kg/m^3 with the incremental steps of 1 kg/m^3. The Poisson's ratio was varied from 0.4 to 0.495 with step size of 0.005. Finally, the stiffness (elastic constants) was set in the range of 1 kPa to 10 kPa with the step size of 1 kPa merged with four additional stiffness values of 3.5, 3.51, 6.5, 6.51 kPa. Total number of 3080 simulations were carried on with all possible combination of the values from the controlling parameters. The vertical displacement of all nodes of the model were recorded at the end of the first and second cycle of the simulation. Subsequently, the dataset yielded from these 3080 simulations were randomly assigned into two separate training and testing dataset with the training dataset consisted of 2156 simulation instances while the rest were assigned to the testing dataset. Finally, for the labeling

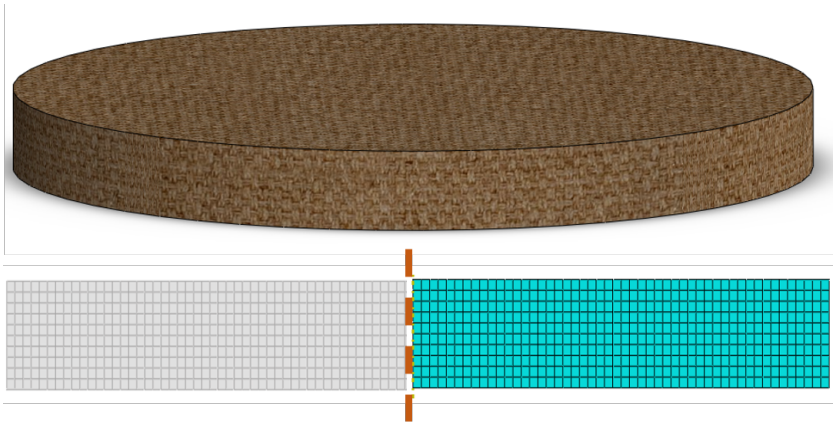

Figure 5.1. The two-dimensional axi-symmetrical finite element model for simulation of the actuation in MRE. The harmonic displacement is applied at the center of the model.

purpose, the simulations carried on with the elastic constants of less than or equal to 3.50 kPa were labeled as "low", the ones greater than 3.5 kPa and less than 6.51 kPa were assigned to the class named as "medium", and the instances with the elastic modulus of greater than or equal to 6.51 kPa were placed in the "high" class. It should be noted density and Poisson's ratio parameters were not included as the features of the model (for training purposes) to check how robust those AI models are toward the changes in those material parameters.

5.2.2. Artificial intelligence techniques

In this section, introduction and explanation on the machine learning and deep learning techniques used for classification of the tissue stiffness will be provided. In the first part, a generalized linear technique known as logistic regression and the context on which was used will be explained and then the convolutional neural network as a deep learning approach will be investigated.

5.2.2.1. Logistic regression

Logistic regression is a widely used algorithm in machine learning for classification applications [153]. Given θ to be the features of the training data including the bias term, it is desired to find a hypothesis $h_\theta(x)$ that can estimate the probability of the input x falling into one of the provided classes in the training data, where θ represents the features of the hypothesis (from the dataset). This probability can be estimated using the Sigmoid function stated as $f(u) = 1/(1+e^{-u})$. Here, for training the logistic regression hypothesis, only the vertical displacement of the upper edge nodes (51 nodes from the surface that harmonic displacement is being applied) at the end of the first and second cycle are used. Therefore, there will be a total number of 102 features. Hence, using a vectorized form, this generalized linear probabilistic hypothesis can be written in the following form [153]:

$$h_\theta(x) = f(\theta^T x) = \frac{1}{1 + e^{-\theta^T(x)}} \tag{5.1}$$

whereas mentioned before, function f is the Sigmoid function. The vector $\theta = [\theta_0, \theta_1, ..., \theta_{102}]$ refers to the coefficients of the trained logistic regression with the θ_0 begin the bias coefficient. The matrix $x = [x_0, x_1, ..., x_{102}]$ represent the values of the features of the problem i.e., the vertical displacement of the upper 51 nodes of the model at the end of the first and second cycles.

Upon the presence of three classes in our training data, and by employing "one vs rest" technique [154] , three different logistic regression models are trained with respect to three existing classes. The cost function associated with logistic regression which should be minimized to find the optimal parameters of the model θ can be stated as the following:

$$C(\theta) = -\frac{1}{n}\sum_{i=1}^{n} l^{(i)} log(h_\theta(x^{(i)}) + (1 - l^{(i)})(1 - log(h_\theta x^{(i)})) + \lambda \sum_{j=1}^{m} \theta_j^2 \tag{5.2}$$

where $l^{(i)}$ refers to the label (class) of the i^{th} training data and $C(\theta)$ denotes the defined cost function for logistic regression. The n stands for the number of samples in the training data which in our case is equal to 3080. The λ is the regularization constant which is used to improve the generalization of the logistic regression by attacking the problem of overfitting or underfitting and the m denotes the number of features in our logistic regression hypothesis which is equal to 102 in our case. It should be noted that the coefficient of the bias term θ_0 is not regularized. Note that, when using "one vs rest" technique, the labels are either 0 or 1 with respect to the formulation of equation (5.2). For example, if training a logistic regression hypothesis for the class "medium" is desired, all the instances labeled as "medium" would be considered 1 and the rest (including "low" and "high") would be labeled as 0.

To minimize the cost function stated in equation (5.2), the gradient descent algorithm can be used which is a gradient based optimization technique. To this end, a gradient of the cost function stated in equation 5.2) is required which can be stated as the following:

$$\frac{\partial C(\theta)}{\partial \theta_j} = \frac{1}{n}\sum_{i=1}^{n} (h_\theta(x^{(i)} - y^{(i)}) x_j^{(i)} + \frac{\lambda}{m}\theta_j \tag{5.3}$$

The equation (5.3), demonstrates the derivative of the cost function with respect to its j^{th} variable. The $x_j^{(i)}$ refers to the j^{th} coordinate of the i^{th} training instance. The gradient descent algorithm uses the gradient of the cost function to adjust the parameters based on the provided initial guess, as the following:

$$\theta_j^{k+1} = \theta_j^k - r\frac{\partial C(\theta)}{\partial \theta_j}, \quad j = 1, 2, ..., m \tag{5.4}$$

where k denotes the iteration number of the gradient descent algorithm and the parameter r is known as the learning rate and it is usually less than 1.0. Each iteration consists of repetition of the equation (5.4) for all m features of the dataset.

5.2.2.2. Convolutional neural network

Convolutional neural network (CNN) is a type of multi-layer perceptron, mostly appropriate for the type of data which has a grid pattern [155]. Benefiting from a special kind of weights known as kernels (or filters), they can capture the spatial features of the input data, and to dynamically learn low- and high-level patterns. A typical CNN has three main components including convolutional layers, pooling layers, and fully connected layers. Convolutional layers weights are adaptively optimized to extract the spatial features of the image, pooling layer is designed to down sample the image to obtain higher order patterns with the small kernel size, and finally, the fully connected layer works with the flattened extracted features of the previous layers to do the classification task. However, it should be noted that the state-of-the-art CNN architectures may have additional elements such as batch normalization, and dilated convolution. The main advantage of the CNN over regular artificial neural networks (ANN) with the fully connected layers, is the independency of the number of its parameters from the input data. This becomes available using kernels and convolutional operations. Since the focus of this paper is not on the CNN, but rather on its application, the details of the CNN will not be discussed and readers are referred to [156] for more information.

Since the MRE FE model has a grid and matrix-wise pattern, CNN can be applied on it for the classification task. As mentioned, the FE model used for MRE simulation had 561 nodes in a 11×51 matrix fashion. With the bottom edge of the model being fixed, the vertical displacement of the nodes lying on this edge will always be zero, and hence, this spurious information can be dropped giving a 10×51 matrix. Given that the vertical displacement of the nodes was recorded at two time instances (end of first and second cycle), the input to the CNN can be viewed as a 10×51×2 tensor. In computer vision terminology, this input is equivalent to a two-channel image with the resolution of 10(width)×51(height). Here, since this approach would result in a matrix with high aspect ratio, it was decided to form the input data by vertical concatenation of the data at the end of each cycle. The vertical concatenation of two 10×51 matrix, will yield a 20×51 matrix with one channel as can be seen from Figure 5.2. By replicating this matrix in the third dimension, a three-channel input with the dimension of 20×51×3 can be obtained.

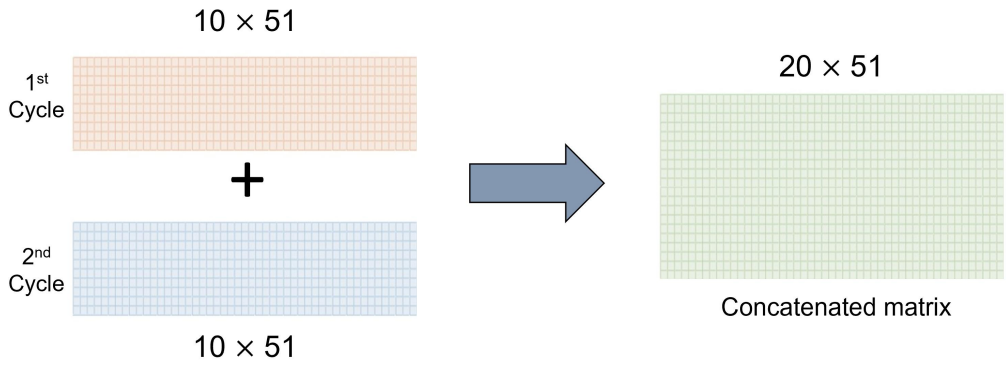

Figure 5.2. The process of preparing the input data for the CNN. The matrix of displacement at the end of the first and the second cycle are vertically concatenated to form a 20×51 matrix. This matrix can be further replicated in the third dimension to represent a three channeled image.

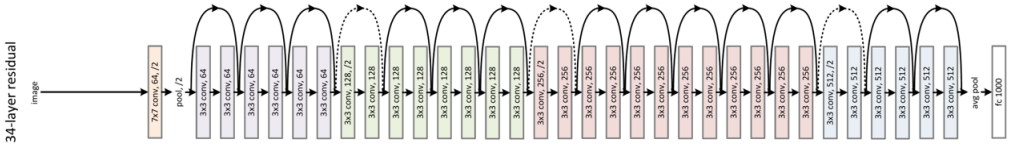

Figure 5.3. ResNet34 architecture [5] originally designed for image classification task on ImageNet dataset [6] with 1000 distinct categories (classes).

Two well-tested CNN architectures, ResNet18, and ResNet34 [5] have been explored by the researchers for performing the classification tasks. These networks have relatively low number of parameters compared to some other famous networks such as AlexNet and VGGNet. Moreover, due to the presence of skipping layers and by passing the data from one layer to the further subsequent layers, it can overcome the problem of vanishing gradient [157] while enjoying the benefit of increasing the number of layers. The high-level view of the ResNet34 architecture is shown in Figure 5.3 [5].

As can be inferred from Figure 5.3, this specific architecture was originally developed to classify an image into a 1000-category problem and hence, it is needed to be modified (ResNet18 as well) to be appropriate for a three-category classification problem. This task was done through modifying the last layer by changing the final 1000 node into a three-node layer. Moreover, in this dissertation, a simple custom CNN was developed with only 11 layers of two-dimensional convolutional and batch normalization operators, accompanied by a fully connected neural network. This architecture is much simpler compared to the ResNet18 and ResNet34 with much smaller

number of trainable parameters. The architecture of this custom-built CNN is illustrated in Figure 5.4.

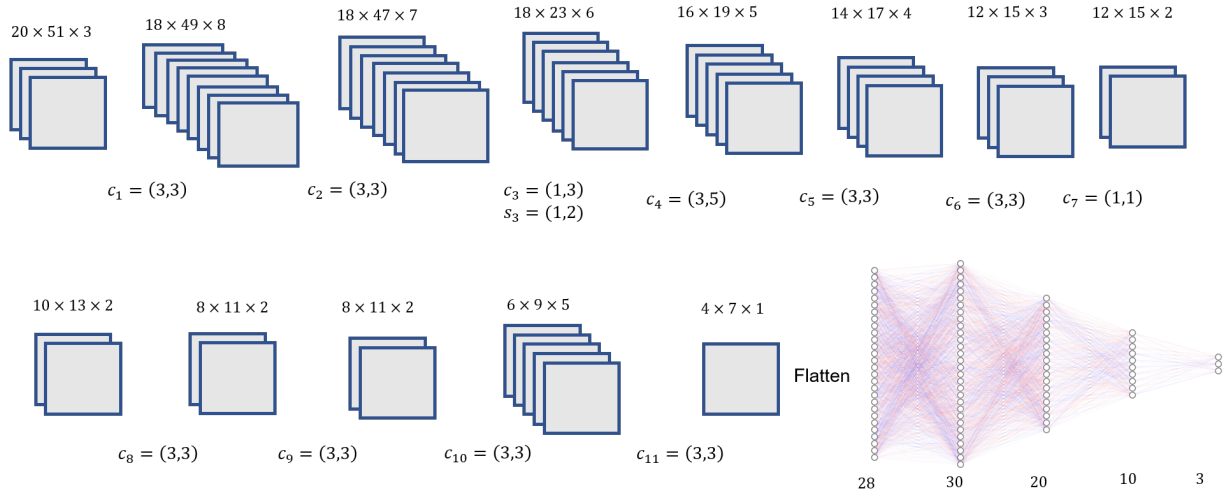

Figure 5.4. The structure of the developed CNN (custom-built). All the layers are accompanied by a batch normalization and nonlinear rectified linear unit (ReLU) activation function. The final layer is a fully connected network with ReLU activation function as well. The matrix sizes are not proportional the actual size of them. The c_i stands for the convolutional operation size in the i^{th} layer and s_i denotes the stride of that convolutional layer. The $s_i = (1, 1)$ except for the cases written otherwise.

5.3. Results

In this section, first, the results of FE MRE simulations will be demonstrated. Subsequently, the outcome of the trained logistic regression and CNN from the FE simulation dataset will be presented.

5.3.1. Shear wave propagation

As mentioned before, the simulations were done for different values of elastic modulus, density, and Poisson's ratio. Finite element simulations are performed in the finite element package of ABAQUS (ABAQUS Inc., Providence, RI). As an example, Figure 5.5 shows the vertical displacement field of the whole model for different elastic modulus values of 2 kPa, 5 kPa, and 8 kPa with the density of 1040 kg/m^3 and Poisson's ratio of 0.495. Figure 5.6 shows the shear wave propagation in the model at the end of the first and the second cycles of the induced harmonic displacement. Since the harmonic displacement has the frequency of 200 Hz, each cycle takes 5 ms to complete,

and therefore, the first and the second cycles correspond to the simulation running time of 5 ms and 10 ms, respectively.

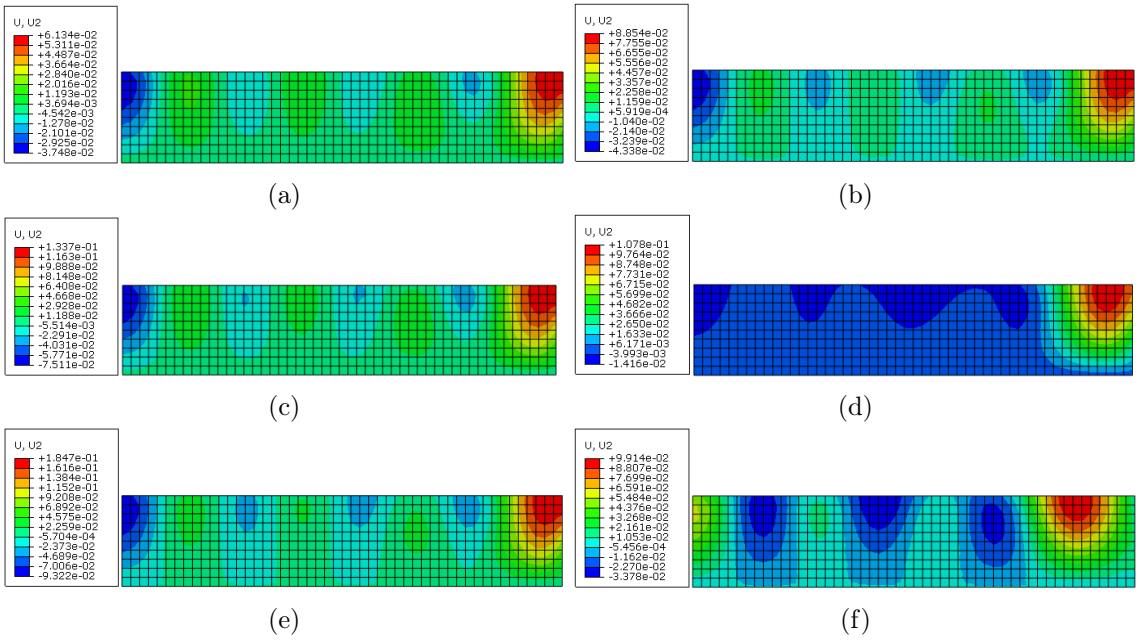

Figure 5.5. FE simulation results showing the vertical displacement field of the model with the assigned elastic modulus values of (a)&(b) 2 kPa, (c)&(d) 5 kPa, and (e)&(f) 8 kPa at the end of the first and the second cycle of the harmonic displacement, respectively.

As it can be seen, in some cases, there is a significant difference between the wave propagation in the first and the second cycle e.g., 5 and 8 kPa. More importantly, no specific obvious correlation can be found through the displacement of the center or any other point of the model, as they are not directly commensurate to the elastic modulus.

5.3.2. Training a logistic regression hypothesis and evaluation

In this section, the training process for training the logistic regression hypothesis defined in equation 5.1 and further evaluation of it will be demonstrated. In a randomly fashion, 60% of the 3080 simulations were assigned for training, 10% went to the CV dataset, and the remaining 30% was used for testing. As can be seen from equation 5.2, the regularized form of the cost function is employed to avoid the possible problem of overfitting or underfitting. To find the appropriate regularization constant λ, several logistic regression models were trained with different values of λ and then were tested on the cross-validation (CV) dataset. The one with the highest score on the

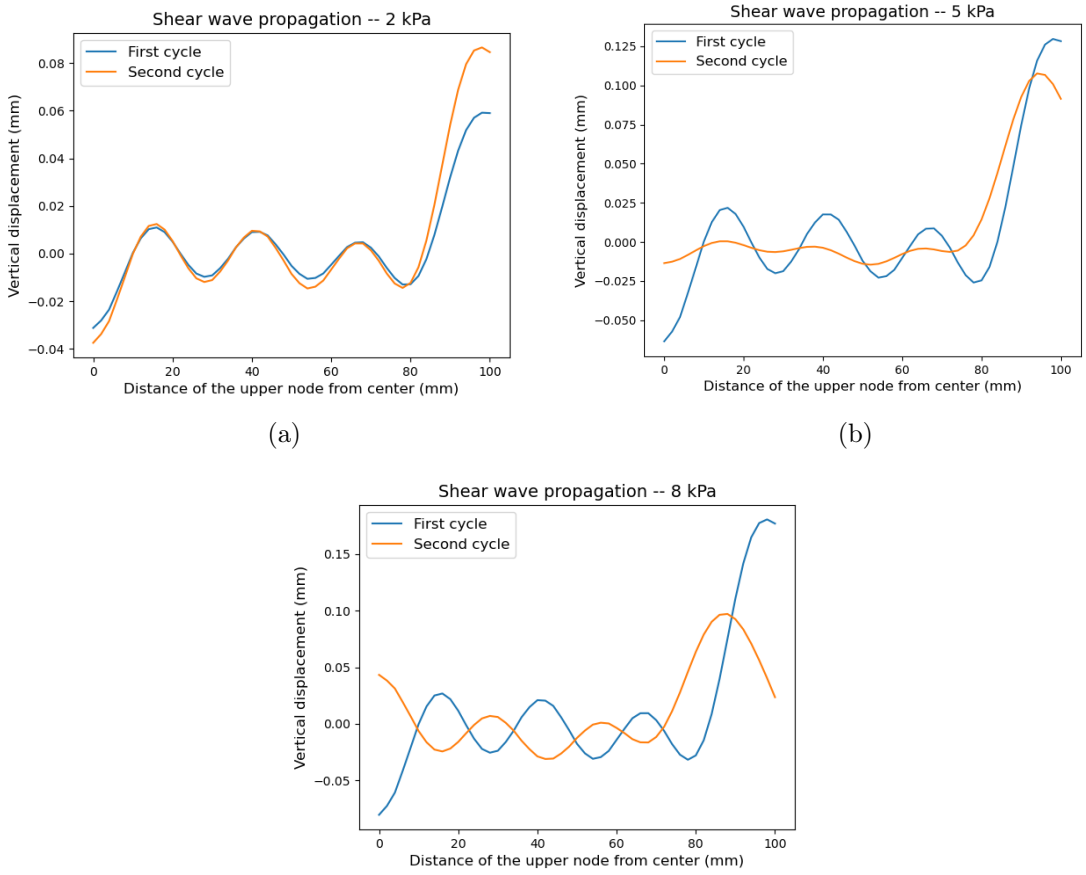

Figure 5.6. Shear wave formation i.e., the upper edge vertical displacement for different elastic constants of (a) 2 kPa, (b) 5 kPa, and (c) 8 kPa corresponding to low, medium, and high stiffness value at the end of the first and the second cycle of the induced harmonic displacement.

CV dataset, was then evaluated against the testing dataset. Total of 197 different regularization constants ranging from 10^{-4} to a large value of 10^{6} were tested with a conclusion that the best value for the regularization constant is $\lambda = 2 \times 10^{4}$. Figure 5.7 shows how the performance and accuracy of the model varies as the regularization constant λ changes evaluated on testing dataset. It can be seen using large numbers for regularization constant helps the hypothesis to better generalize and alleviates the problem of overfitting. However, going beyond the optimal value of $\lambda = 2 \times 10^{4}$, the performance starts to drop shifting the model to be biased.

Testing the trained logistic regression hypothesis with the regularization constant of 2×10^{4} on the testing dataset provided the accuracy of 91.3%. The distribution of the classes on the testing dataset and the performance of the hypothesis with respect to each class can be seen in Figure 5.8.

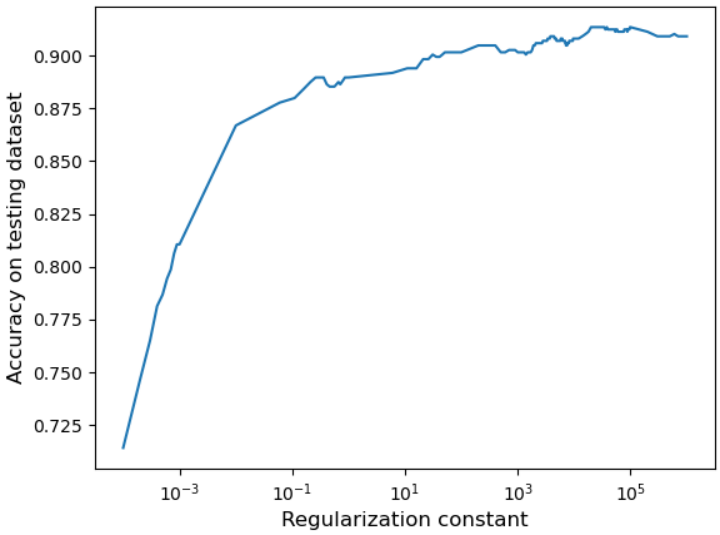

Figure 5.7. The performance of the regularized logistic regression hypothesis with different regularization constants.

In Table 5.1, different criteria such as sensitivity (recall), specificity, precision, F1 score, and accuracy for each of the three classes of interest are listed.

Table 5.1. The sensitivity, specificity, precision, F1 score, and accuracy for each of the classes including Low, Medium, and High stiffness.

Class	Sensitivity	Specificity	Precision	F1 score	Accuracy
Low	0.932	0.973	0.932	0.932	0.961
Medium	0.882	0.931	0.876	0.879	0.913
High	0.930	0.965	0.936	0.933	0.952

5.3.3. CNN training and evaluation

Using the field displacement of the model at two-time steps (end of the first and the second cycle), three different CNN models are trained using a data-driven approach to build a tissue stiffness classifier. ResNet18, ResNet34, and one custom-built CNN were trained on the same 3080 simulations used for logistic regression hypothesis training, however, in lieu of using only the upper edge nodes displacement, the whole field displacement was used as input to the CNN. The specifications of these CNNs were discussed in the Methodology section. For training of the CNNs, no CV dataset was involved, and the training was done on 70% of the whole data to be further

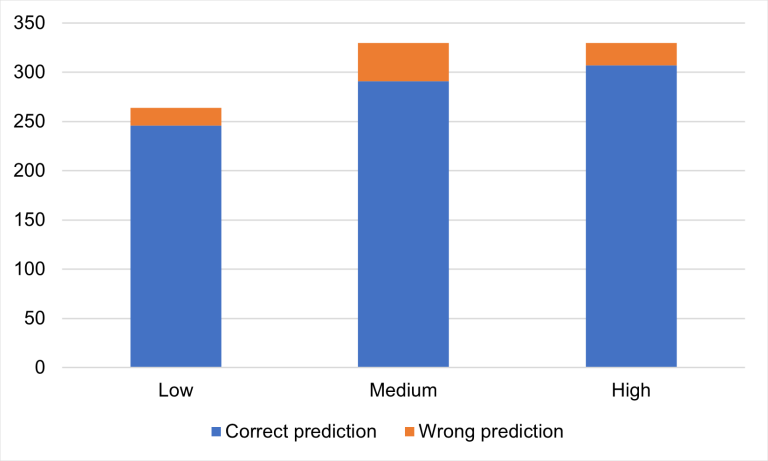

Figure 5.8. The accuracy demonstration for each specific class. The portion of mislabeled predictions can be seen for each class.

evaluated on the rest 30% of the dataset corresponding to 924 simulation cases. The Table 5.2 summarizes the evaluation of the trained CNNs on our testing dataset which was kept the same for all the three CNNs.

Table 5.2. Different trained CNNs and the accuracy of their evaluation on the same testing dataset. The number of trainable parameters of the models are also shown.

CNN	Number of parameters	Accuracy
ResNet18	11.7 M	0.861
ResNet34	21.2 M	0.863
Custom-built	4241	0.895

As it can be seen from the Table 5.2, the best accuracy was achieved with our custom-built CNN, while the performance of the ResNet18 and ResNet34 was close together. All the listed CNNs were trained for 300 epochs with the batch size of 256. The Adam optimizer was used for minimizing the loss function (cross entropy loss) with the variable learning rate ranging from 10^{-4} to 10^{-6}.

5.4. Discussion

There is a main difference between the way the logistic regression and the CNN were constructed and that was in the terms of the input to those prediction models. While for the logistic regression, only the vertical displacement of the upper edge nodes in two-time steps was used, the complete field displacement of the model was considered as input for the CNN models. In this way, the number of features (input) for the logistic regression was 102 (51 nodes in 2-time steps)

while the input to the CNN was vertically stacked matrices of displacement from one half of the axi-symmetrical FE model, where each matrix corresponds to the field displacement at one time step yielding a merged 20×51 matrix.

As in the MR imaging, there would be limited access to the displacement of the inner nodes of the model, the logistic regression construction is closer to the real-world application and the study on the CNN can be viewed as evaluating the feasibility of data-driven modeling approaches for tissue stiffness classification. However, even when seemingly more information was used as input for the CNN structure, the performance i.e., correct prediction of the class of the instances, drops and demonstrate a sub-par performance compared to the logistic regression. The most plausible explanation for this is the level of difficulty associated with training of the deep learning models compared to the linear ones. Per Table 5.2, even for our own simple custom-built CNN, the number of trainable parameters is high which makes the model prone to overfitting and consequently poor generalization. This problem was tried to be fixed by reducing the number of layers and nodes in the fully connected layers, but it was not possible to achieve a better performance. This explanation is further buttressed through the fact that the complicated models such as ResNet18 and ResNet34 show worse performance compared to our custom-built CNN. This is what was expected from the beginning, since the large number of parameters in those networks make them in need of much larger dataset opposed to what has been used for their training[1].

It should be noted that our model is density and Poisson's ratio agnostic. While these two variables were changed in different simulations, they were not considered as input (feature) to both of the proposed AI approaches. This can be viewed as an advantage of this AI-based approach of ours compared to the inverse-analysis. This exclusion of those parameters is aligned to the real-world situation, as there is always a variation in person-to-person biological tissues material properties. However, upon the inclusion of these two parameters (density and Poisson's ratio) in the logistic regression and with the proper amount of regularization, 100% accuracy was obtained.

In our simulations, the control parameters were stiffness, density, and Poisson's ratio. These parameters may be close from one instance to another and hence, the nodes displacements would be close as well. Therefore, the question rises, if we can simply assign the class of an unknown instance to the class of the closest (in terms of the nodes displacement) simulation with a known

[1] 70% of the total 3080 simulations were used for training.

category? This is basically, a definition to the K-Means classification technique. The possibility of exploiting the K-Means as a possible classification technique was examined. Even by using a high number of neighbor nodes such as 27, the obtained accuracy level was no more than 0.84 which is behind what gained with logistic regression. This is a confirmation on the fact that the displacement pattern of the nodes in MRE simulation is more complex that could be taken care of with the simple closest-simulation finding approach i.e., K-Means.

Looking into class-specific performance of the trained logistic regression in Table 5.1, it can be seen that it performs better for the Low and High classes compared to the Medium class. The instances of the High class can be critical in terms of the medical diagnosis, as the higher level of stiffness are usually associated with pathology. For example, the sensitivity measure, determines how many of the instances with the actual High stiffness class are predicted. As can be seen from the same table, the sensitivity for High class was found to be better compared to that of the Medium class. From Table 5.1, it seems that our logistic regression hypothesis is performing better in the marginal classes and the performance drops in the middle class. One possible explanation could be from the fact that there are higher number of instances closer to other ones. For example, while certain number of instances in Low classes are close to the Medium instances, this number could be potentially doubled for the Medium class, as some are close to the Low and some other are close to the High class.

5.5. Conclusion

In this part of the dissertation, a data-driven AI approach for creating a tissue stiffness classifier framework based on the FE simulation of MRE was created. Two AI-based approaches including regularized logistic regression and deep convolutional neural networks were studied. The vertical displacement of the upper edge nodes of the model were used as an input features to the logistic regression model and the concatenated vertical displacement field matrix of the model obtained at the end of the first and second cycle of the imposed harmonic displacement was used as an input tensor to the different CNNs studied here.

A two-dimensional axi-symmetrical model was created for FE simulations and a harmonic displacement imposed at the center of the model was used to simulate the mechanical actuator commonly used in the MRE process. To find the field displacement of the model at different time steps, a transient dynamic modal analysis was performed.

Total of 3080 simulations through realistic variation of three control parameters including stiffness, density, and Poisson's ratio were conducted. Based on the linear elastic constants assigned to the tissue, the simulation instances were labeled into one of the three classes including Low, Medium, and High stiffness in a near evenly distributed fashion. Training and hyper-tuning the logistic regression hypothesis on the training and CV dataset, it became possible to obtain the accuracy of 0.913. This accuracy measure indicates the fraction of the testing dataset instances which the prediction was the same as our expected class assignment of those simulations (based on their stiffness values). Moreover, the high value of sensitivity on the instances with High stiffness class, indicates the high success rate of the logistic regression model in pathology diagnosis with the assumption that the pathology increases the stiffness of certain biological tissues. While the deep learning CNN approach is more complicated compared to the linear logistic regression and even more data is fed to the CNN for training (whole displacement field rather than the upper edge displacement), it cannot reach the level of the performance observed with logistic regression. While ResNet18 and ResNet34 architectures are among some of the very well-known models for classification purposes, the number of trainable parameters in them are too high for appropriate training and hence generalization. On the contrary our simple developed CNN with simple stride convolutional and batch normalization layer was able to obtain better performance but still not to the level of logistic regression.

6. CONCLUSION AND SUGGESTIONS FOR FUTURE WORKS

In this chapter, A conclusion on the previous parts of this dissertation is provided. Moreover some suggestions for continuing this research on the possible future works that can be carried on will be looked into.

6.1. Conclusion

The problem of brain tissue material characterization shows its importance in the simulation of TBI and upon the recognition of several gaps and challenges in the field, several research topics were carried on addressing those issues as reflected in this dissertation.

First, C-PSO algorithm was developed which helps to find the most accurate parameters of different hyperelastic and visco-hyperelastic constitutive models. To this end, the constraints of the hyperelastic and visco-hyperelastic models were identified and used to reduce the time complexity of the developed optimization algorithm. To test the algorithm, several uniaxial and relaxation tests were performed on the bovine brain tissue. The curve fitting for hyperelastic models were done with both C-PSO and classical LMA and for most of the hyperelastic models, the performance of those two algorithms were noticed to be nearly equal. However, the performance of the C-PSO was found to be highly superior compared to another classical curve fitting algorithm (for constrained optimization), TRF algorithm, for the visco-hyperelastic model. Even for the relaxation tests with high strain rate, the performance of the TRF was found to be even worse than the naive approach of stress averaging. The accuracy of the curve fitting with the C-PSO was found to be higher than 99% while it was found to be negative for TRF algorithm results. Additionally, through the exploration of different convergence strategies with PSO implementation, it was found that the proximity radius criterion can reduce the time complexity up to 11% while maintaining the accuracy of the fitting. The importance of this developed optimization technique and modifying it to reduce the time complexity comes from the fact that it could be used for both experimental data curve fitting and simulation-based optimizations.

The better understanding of the DAI as a common form of TBI requires better understanding of the brain white matter micro-level constituents including axons and ECM. The hyperelastic characterization of these micro-level constituents were performed for three different uniaxial loading modes of tension, compression, and simple shear. The uniaxial tension, compression, and shear uniaxial loading tests performed on corpus callosum was obtained from [1]. The micromechanical simulation was then used in the context of a simulation-based optimization framework to obtain the hyperelastic properties of the axons and ECM in terms of the Ogden one term model. The initial shear modulus of the axons was found to be 0.51, 0.63, and 0.48 kPa for tension, compression, and shear uniaxial loading modes, respectively. The difference on mechanical behavior of the axons in these loading modes was a source of motivation to find and report the best-fit parameters that can best describe its behavior in all loading modes. Since these best-fit parameters are defined to minimize the error of estimation on all loading modes combined, it could be load agnostic hyperelastic parameters. The best-fit initial shear modulus (using Ogden one-term model) of the axons was found to be 0.531 kPa.

Moreover, the time-dependent characterization of axons and ECM was done for the visco-hyperelastic characterization of axons and ECM to describe their time-dependent behavior. Using the developed C-PSO in a simulation-based optimization framework, the visco-hyperelastic parameters of axons and ECM were found for different strain rates of 0.0001, 0.01, and 1.0 s^{-1} from the macro-level experimental relaxation tests on human brain white matter [4]. Since the relaxation tests were done for the time of 500 seconds, it was of the utmost importance to use the modified C-PSO that is efficient in terms of the time complexity as previously described. The initial shear modulus of the axons for the strain rates of 0.0001, 0.01, and 1.0 s^{-1} were found to be 0.4018, 0.8280, and 1.7210, respectively. The first and second order regression were successfully performed to capture the initial and reduced shear modulus dependency of the axons to the strain rate. While the first order regression was found to be sufficient for the initial shear modulus, the reduced shear modulus was found to be better described through the second order regression.

Finally, in another part of the dissertation, the possibility of using a data-driven AI based approach for classifying the tissue stiffness for detection of the tissues with high level of stiffness was explored. A two-dimensional axi-symmetrical model with the height of 10 mm and the width of 200 mm was created in the ABAQUS FE package and a harmonic displacement was imposed

at the center of the model with the frequency of 200 Hz to simulate the mechanical actuator used in the MRE process. MRE FE simulation was done through two steps. First, finding the natural frequencies of the model and later, using the transient dynamic modal analysis to find the displacement field of the model. Total number of 3080 simulations were performed through the combinatorial variation of stiffness, density, and Poisson's ratio quantities. Using the linear elastic model, the stiffness values of the material were changed from 2 to 10 kPa, the Poisson's ratio was varied from 0.4 to 0.495, and the density was ranged from 1040 to 1090 kg/m^3. In an evenly distributed fashion, the simulation instances were labeled as Low, Medium, and High stiffness classes based on their stiffness values. First, a logistic regression hypothesis was trained based on the 60% of the simulation data as the training dataset. The regularization parameter was found through the process of hyperparameter tuning and evaluation on the cross-validation dataset which constitutes 10% of the total dataset instances. Testing the trained regularized logistic regression on the remaining 30% of the data, showed the accuracy performance of 0.9134 indicating the fraction of the instances which were correctly classified. The high sensitivity of the logistic regression model for the class of "High" stiffness, with the amount of 0.93 could be a well-accepted performance for detection of the pathological tissues. The CNN-style architecture was then explored as a deep learning approach for classification purpose. ResNet18, ResNet34, and a custom-built CNN were trained and tested on the simulation dataset. While only the vertical displacement of the upper edge nodes of the model were used as an input for the logistic regression, the whole vertical displacement field of the FE model was used for CNN training. This means that more information was used as an input to the CNN compared to logistic regression and the highest accuracy was obtained by the custom-built CNN with the value of 0.893. While not as good as logistic regression, the acceptable performance of these AI-based approaches on the context of data-driven modeling opens the door for quick decision-making process which could help the physicians for detection of pathological tissues. Moreover, these AI-based approaches were agnostic of the density, and Poisson's ratio. While these parameters were changed in the simulations, they were not considered as input parameters for training of the logistic regression and the CNN. This is an improvement over the inversion algorithms where these properties need to be known for stiffness field map generation.

6.2. Suggestions for future works

The simulation-based optimization framework reflected in this dissertation is based on iterative FE simulations to minimize a defined objective (cost) function. Based on what experienced through the studies of this dissertation, several thousands of simulations were needed for micromechanical characterization of brain white matter. Given the time required for completion of each single FE simulation, this process is highly time-consuming. AI-based regression techniques can be used to predict the results of the FE simulation from the previous simulations without running the FE simulation, which helps to save time and further reduce the time complexity of the simulation-based optimization.

Biphasic constitutive models have been developed for macromechanical characterization of brain [55, 158]. Given the presence of liquid water in the brain tissue, development of the biphasic models for the micromechanical characterization of brain tissue can be of the interest.

Finally, upon the confirmation of the efficiency of the AI-based approaches for tissue stiffness classification, the experimental validation of those AI frameworks can be performed, if the MRE technology is accessible. Moreover, three-dimensional FE models can be studied with the same introduced AI frameworks as well.

REFERENCES

[1] S. Budday, G. Sommer, C. Birkl, C. Langkammer, J. Haybaeck, J. Kohnert, M. Bauer, F. Paulsen, P. Steinmann, E. Kuhl, *et al.*, "Mechanical characterization of human brain tissue," *Acta biomaterialia*, vol. 48, pp. 319–340, 2017.

[2] S. Javid, A. Rezaei, and G. Karami, "A micromechanical procedure for viscoelastic characterization of the axons and ecm of the brainstem," *Journal of the mechanical behavior of biomedical materials*, vol. 30, pp. 290–299, 2014.

[3] D. Meaney, "Relationship between structural modeling and hyperelastic material behavior: application to CNS white matter," *Biomechanics and modeling in mechanobiology*, vol. 1, no. 4, pp. 279–293, 2003.

[4] A. E. Forte, S. M. Gentleman, and D. Dini, "On the characterization of the heterogeneous mechanical response of human brain tissue," *Biomechanics and modeling in mechanobiology*, vol. 16, no. 3, pp. 907–920, 2017.

[5] K. He, X. Zhang, S. Ren, and J. Sun, "Deep residual learning for image recognition," in *Proceedings of the IEEE conference on computer vision and pattern recognition*, pp. 770–778, 2016.

[6] J. Deng, W. Dong, R. Socher, L.-J. Li, K. Li, and L. Fei-Fei, "Imagenet: A large-scale hierarchical image database," in *2009 IEEE conference on computer vision and pattern recognition*, pp. 248–255, Ieee, 2009.

[7] A. Azim and B. Joseph, "Traumatic brain injury," in *Surgical Critical Care Therapy*, pp. 1–10, Springer, 2018.

[8] C. A. Taylor, J. M. Bell, M. J. Breiding, and L. Xu, "Traumatic brain injury-related emergency department visits, hospitalizations, and deaths-united states, 2007 and 2013.," *Morbidity and mortality weekly report. Surveillance summaries (Washington, DC: 2002)*, vol. 66, no. 9, pp. 1–16, 2017.

[9] I. Humphreys, R. L. Wood, C. J. Phillips, and S. Macey, "The costs of traumatic brain injury: a literature review," *ClinicoEconomics and outcomes research: CEOR*, vol. 5, p. 281, 2013.

[10] H. Mao, L. Zhang, B. Jiang, V. V. Genthikatti, X. Jin, F. Zhu, R. Makwana, A. Gill, G. Jandir, A. Singh, *et al.*, "Development of a finite element human head model partially validated with thirty five experimental cases," *Journal of biomechanical engineering*, vol. 135, no. 11, 2013.

[11] A. M. Nahum, R. Smith, and C. C. Ward, "Intracranial pressure dynamics during head impact," tech. rep., SAE Technical Paper, 1977.

[12] X. Trosseille, C. Tarriere, F. Lavaste, F. Guillon, and A. Domont, "Development of a fem of the human head according to a specific test protocol," tech. rep., SAE Technical Paper, 1992.

[13] W. N. Hardy, C. D. Foster, M. J. Mason, K. H. Yang, A. I. King, and S. Tashman, "Investigation of head injury mechanisms using neutral density technology and high-speed biplanar X-ray," tech. rep., SAE Technical Paper, 2001.

[14] G. W. Nyquist, J. M. Cavanaugh, S. J. Goldberg, and A. I. King, "Facial impact tolerance and response," *SAE transactions*, pp. 850–871, 1986.

[15] K. M. Tse, L. B. Tan, S. J. Lee, S. P. Lim, and H. P. Lee, "Development and validation of two subject-specific finite element models of human head against three cadaveric experiments," *International journal for numerical methods in biomedical engineering*, vol. 30, no. 3, pp. 397–415, 2014.

[16] Y. Li, W. Zhang, Y.-C. Lu, and C. Wu, "Hyper-viscoelastic mechanical behavior of cranial pia mater in tension," *Clinical Biomechanics*, vol. 80, p. 105108, 2020.

[17] D. De Kegel, J. Vastmans, H. Fehervary, B. Depreitere, J. Vander Sloten, and N. Famaey, "Biomechanical characterization of human dura mater," *Journal of the mechanical behavior of biomedical materials*, vol. 79, pp. 122–134, 2018.

[18] X. Ning, Q. Zhu, Y. Lanir, and S. S. Margulies, "A transversely isotropic viscoelastic constitutive equation for brainstem undergoing finite deformation," *Journal of biomechanical engineering*, vol. 128, no. 6, pp. 925–933, 2006.

[19] J. Rahmoun, A. Auperrin, R. Delille, H. Naceur, and P. Drazetic, "Characterization and micromechanical modeling of the human cranial bone elastic properties," *Mechanics Research Communications*, vol. 60, pp. 7–14, 2014.

[20] S. Budday, T. C. Ovaert, G. A. Holzapfel, P. Steinmann, and E. Kuhl, "Fifty shades of brain: a review on the mechanical testing and modeling of brain tissue," *Archives of Computational Methods in Engineering*, pp. 1–44, 2019.

[21] S. Chatelin, A. Constantinesco, and R. Willinger, "Fifty years of brain tissue mechanical testing: from in vitro to in vivo investigations," *Biorheology*, vol. 47, no. 5-6, pp. 255–276, 2010.

[22] A. Goriely, M. G. Geers, G. A. Holzapfel, J. Jayamohan, A. Jérusalem, S. Sivaloganathan, W. Squier, J. A. van Dommelen, S. Waters, and E. Kuhl, "Mechanics of the brain: perspectives, challenges, and opportunities," *Biomechanics and modeling in mechanobiology*, vol. 14, no. 5, pp. 931–965, 2015.

[23] R. Cloots, J. Van Dommelen, T. Nyberg, S. Kleiven, and M. Geers, "Micromechanics of diffuse axonal injury: influence of axonal orientation and anisotropy," *Biomechanics and modeling in mechanobiology*, vol. 10, no. 3, pp. 413–422, 2011.

[24] Y. Pan, A. A. Pelegri, and D. I. Shreiber, "Simulation of the mechanical behavior of white matter using a micromechanics finite element method," *MRS Online Proceedings Library*, vol. 1301, no. 1, pp. 87–92, 2011.

[25] M. Ramzanpour, M. Hosseini-Farid, J. McLean, M. Ziejewski, and G. Karami, "Visco-hyperelastic characterization of human brain white matter micro-level constituents in different strain rates," *Medical & Biological Engineering & Computing*, vol. 58, no. 9, pp. 2107–2118, 2020.

[26] M. Ramzanpour, M. Hosseini-Farid, M. Ziejewski, and G. Karami, "A constrained particle swarm optimization algorithm for hyperelastic and visco-hyperelastic characterization of soft biological tissues," *International Journal for Computational Methods in Engineering Science and Mechanics*, pp. 1–16, 2020.

[27] M. Ramzanpour, M. Hosseini-Farid, M. Ziejewski, and G. Karami, "Microstructural hyperelastic characterization of brain white matter in tension," in *ASME International Mechanical Engineering Congress and Exposition*, vol. 59407, p. V003T04A009, American Society of Mechanical Engineers, 2019.

[28] M. Ramzanpour, M. Hosseini-Farid, M. Ziejewski, and G. Karami, "Particle swarm optimization method for hyperelastic characterization of soft tissues," in *ASME International Mechanical Engineering Congress and Exposition*, vol. 59469, p. V009T11A028, American Society of Mechanical Engineers, 2019.

[29] M. Ramzanpour, M. Hosseini-Farid, J. McLean, M. Ziejewski, and G. Karami, "A logistic regression analysis for tissue stiffness categorization through magnetic resonance elastography," in *ASME International Mechanical Engineering Congress and Exposition*, vol. 84522, p. V005T05A043, American Society of Mechanical Engineers, 2020.

[30] R. P. Vito and S. A. Dixon, "Blood vessel constitutive models—1995–2002," *Annual review of biomedical engineering*, vol. 5, no. 1, pp. 413–439, 2003.

[31] J. Bols, J. Degroote, B. Trachet, B. Verhegghe, P. Segers, and J. Vierendeels, "A computational method to assess the in vivo stresses and unloaded configuration of patient-specific blood vessels," *Journal of computational and Applied mathematics*, vol. 246, pp. 10–17, 2013.

[32] F. Pervin, W. W. Chen, and T. Weerasooriya, "Dynamic compressive response of bovine liver tissues," *Journal of the mechanical behavior of biomedical materials*, vol. 4, no. 1, pp. 76–84, 2011.

[33] C. D. Untaroiu and Y.-C. Lu, "Material characterization of liver parenchyma using specimen-specific finite element models," *Journal of the mechanical behavior of biomedical materials*, vol. 26, pp. 11–22, 2013.

[34] K. Laksari, M. Shafieian, and K. Darvish, "Constitutive model for brain tissue under finite compression," *Journal of biomechanics*, vol. 45, no. 4, pp. 642–646, 2012.

[35] L. A. Mihai, L. Chin, P. A. Janmey, and A. Goriely, "A comparison of hyperelastic constitutive models applicable to brain and fat tissues," *Journal of The Royal Society Interface*, vol. 12, no. 110, p. 20150486, 2015.

[36] S. A. Yousefsani, A. Shamloo, and F. Farahmand, "Micromechanics of brain white matter tissue: A fiber-reinforced hyperelastic model using embedded element technique," *Journal of the mechanical behavior of biomedical materials*, vol. 80, pp. 194–202, 2018.

[37] M. Hosseini-Farid, M. Amiri-Tehrani-Zadeh, M. Ramzanpour, M. Ziejewski, and G. Karami, "The strain rates in the brain, brainstem, dura, and skull under dynamic loadings," *Mathematical and Computational Applications*, vol. 25, no. 2, p. 21, 2020.

[38] M. Ramzanpour, A. Eslaminejad, M. Hosseini-Farid, M. Ziejewski, and G. Karami, "Comparative study of coup and contrecoup brain injury in impact induced TBI," *Biomedical sciences instrumentation*, vol. 54 (1), pp. 76–82, 12 2018.

[39] P. Saboori and G. Walker, "Brain injury and impact characteristics," *Annals of biomedical engineering*, vol. 47, no. 9, pp. 1982–1992, 2019.

[40] M. Hosseini-Farid, M. Ramzanpour, A. Eslaminejad, M. Ziejewski, and G. Karami, "Computational simulation of brain injury by golf ball impacts in adult and children," *Biomedical Sciences Instrumentation*, vol. 54, no. 1, pp. 369–376, 2018.

[41] M. Toma and P. D. Nguyen, "Coup-contrecoup brain injury: fluid–structure interaction simulations," *International journal of crashworthiness*, vol. 25, no. 2, pp. 175–182, 2020.

[42] M. A. Green, L. E. Bilston, and R. Sinkus, "In vivo brain viscoelastic properties measured by magnetic resonance elastography," *NMR in Biomedicine: An International Journal Devoted to the Development and Application of Magnetic Resonance In vivo*, vol. 21, no. 7, pp. 755–764, 2008.

[43] C. L. Johnson and E. H. Telzer, "Magnetic resonance elastography for examining developmental changes in the mechanical properties of the brain," *Developmental cognitive neuroscience*, vol. 33, pp. 176–181, 2018.

[44] G. Low, S. A. Kruse, and D. J. Lomas, "General review of magnetic resonance elastography," *World journal of radiology*, vol. 8, no. 1, p. 59, 2016.

[45] Q. Chen, S. I. Ringleb, A. Manduca, R. L. Ehman, and K.-N. An, "A finite element model for analyzing shear wave propagation observed in magnetic resonance elastography," *Journal of Biomechanics*, vol. 38, no. 11, pp. 2198–2203, 2005.

[46] B. Rashid, M. Destrade, and M. D. Gilchrist, "Mechanical characterization of brain tissue in simple shear at dynamic strain rates," *Journal of the mechanical behavior of biomedical materials*, vol. 28, pp. 71–85, 2013.

[47] S. Budday, G. Sommer, J. Haybaeck, P. Steinmann, G. Holzapfel, and E. Kuhl, "Rheological characterization of human brain tissue," *Acta biomaterialia*, vol. 60, pp. 315–329, 2017.

[48] M. Hosseini-Farid, A. Rezaei, A. Eslaminejad, M. Ramzanpour, M. Ziejewski, and G. Karami, "Instantaneous and equilibrium responses of the brain tissue by stress relaxation and quasi-linear viscoelasticity theory," *Scientia Iranica*, vol. 26, no. 4: Special Issue Dedicated to Professor Abolhassan Vafai, pp. 2047–2056, 2019.

[49] S. Budday, G. Sommer, G. Holzapfel, P. Steinmann, and E. Kuhl, "Viscoelastic parameter identification of human brain tissue," *Journal of the mechanical behavior of biomedical materials*, vol. 74, pp. 463–476, 2017.

[50] K. Miller and K. Chinzei, "Constitutive modelling of brain tissue: experiment and theory," *Journal of biomechanics*, vol. 30, no. 11-12, pp. 1115–1121, 1997.

[51] M. H. Farid, *Mechanical characterization and constitutive modeling of rate dependent viscoelastic brain tissue under high rate loadings*. PhD thesis, North Dakota State University, 2019.

[52] K. Miller and K. Chinzei, "Mechanical properties of brain tissue in tension," *Journal of biomechanics*, vol. 35, no. 4, pp. 483–490, 2002.

[53] B. Rashid, M. Destrade, and M. D. Gilchrist, "Mechanical characterization of brain tissue in compression at dynamic strain rates," *Journal of the mechanical behavior of biomedical materials*, vol. 10, pp. 23–38, 2012.

[54] M. Hosseini-Farid, M. Ramzanpour, J. McLean, M. Ziejewski, and G. Karami, "Rate-dependent constitutive modeling of brain tissue," *Biomechanics and modeling in mechanobiology*, pp. 1–12, 2019.

[55] M. Hosseini-Farid, M. Ramzanpour, J. McLean, M. Ziejewski, and G. Karami, "A poro-hyper-viscoelastic rate-dependent constitutive modeling for the analysis of brain tissues," *Journal of the Mechanical Behavior of Biomedical Materials*, vol. 102, p. 103475, 2020.

[56] K. Kallol, M. Motalab, M. Parvej, P. Konari, H. Barghouthi, and M. Khandaker, "Differences of curing effects between a human and veterinary bone cement," *Materials*, vol. 12, no. 3, p. 470, 2019.

[57] T. C. Gasser, R. W. Ogden, and G. A. Holzapfel, "Hyperelastic modelling of arterial layers with distributed collagen fibre orientations," *Journal of the royal society interface*, vol. 3, no. 6, pp. 15–35, 2006.

[58] L. A. Mihai, S. Budday, G. A. Holzapfel, E. Kuhl, and A. Goriely, "A family of hyperelastic models for human brain tissue," *Journal of the Mechanics and Physics of Solids*, vol. 106, pp. 60–79, 2017.

[59] M. Hosseini-Farid, M. Ramzanpour, M. Ziejewski, and G. Karami, "A compressible hyper-viscoelastic material constitutive model for human brain tissue and the identification of its parameters," *International Journal of Non-Linear Mechanics*, vol. 116, pp. 147–154, 2019.

[60] J. Shojaeiarani, M. Hosseini-Farid, and D. Bajwa, "Modeling and experimental verification of nonlinear behavior of cellulose nanocrystals reinforced poly (lactic acid) composites," *Mechanics of Materials*, 2019.

[61] M. Hosseini Farid, M. Ramzanpour, M. Ziejewski, and G. Karami, "A biphasic viscoelastic constitutive model for brain tissue," in *ASME International Mechanical Engineering Congress and Exposition*, vol. 59407, p. V003T04A005, American Society of Mechanical Engineers, 2019.

[62] K. Levenberg, "A method for the solution of certain non-linear problems in least squares," *Quarterly of applied mathematics*, vol. 2, no. 2, pp. 164–168, 1944.

[63] J. J. Moré, "The Levenberg-Marquardt algorithm: implementation and theory," in *Numerical analysis*, pp. 105–116, Springer, 1978.

[64] A. R. Conn, N. I. Gould, and P. L. Toint, *Trust region methods*. SIAM, 2000.

[65] H. Hoursan, F. Farahmand, and M. T. Ahmadian, "A three-dimensional statistical volume element for histology informed micromechanical modeling of brain white matter," *Annals of biomedical engineering*, vol. 48, no. 4, pp. 1337–1353, 2020.

[66] M. H. R. Ghoreishy, "Determination of the parameters of the prony series in hyper-viscoelastic material models using the finite element method," *Materials & Design*, vol. 35, pp. 791–797, 2012.

[67] M. Hosseini Farid, M. Ramzanpour, M. Ziejewski, and G. Karami, "A constitutive material model with strain-rate dependency for brain tissue," in *ASME International Mechanical Engineering Congress and Exposition*, vol. 59407, p. V003T04A004, American Society of Mechanical Engineers, 2019.

[68] M. Hosseini Farid, A. Eslaminejad, M. Ramzanpour, M. Ziejewski, and G. Karami, "The strain rates of the brain and skull under dynamic loading," in *ASME 2018 international mechanical engineering congress and exposition*, American Society of Mechanical Engineers Digital Collection, 2018.

[69] X. Zhai, E. A. Nauman, D. Moryl, R. Lycke, and W. W. Chen, "The effects of loading-direction and strain-rate on the mechanical behaviors of human frontal skull bone," *Journal of the mechanical behavior of biomedical materials*, vol. 103, p. 103597, 2020.

[70] W. H. Press and S. A. Teukolsky, "Savitzky-Golay smoothing filters," *Computers in Physics*, vol. 4, no. 6, pp. 669–672, 1990.

[71] D. Acharya, A. Rani, S. Agarwal, and V. Singh, "Application of adaptive Savitzky–Golay filter for EEG signal processing," *Perspectives in science*, vol. 8, pp. 677–679, 2016.

[72] G. Marckmann and E. Verron, "Comparison of hyperelastic models for rubber-like materials," *Rubber chemistry and technology*, vol. 79, no. 5, pp. 835–858, 2006.

[73] G. DeBotton, I. Hariton, and E. Socolsky, "Neo-Hookean fiber-reinforced composites in finite elasticity," *Journal of the Mechanics and Physics of Solids*, vol. 54, no. 3, pp. 533–559, 2006.

[74] R. W. Ogden, *Non-linear elastic deformations*. Courier Corporation, 1997.

[75] J. S. Bergstrom, *Mechanics of solid polymers: theory and computational modeling*. William Andrew, 2015.

[76] K. Romanov, "The drucker stability of a material," *Journal of Applied Mathematics and Mechanics*, vol. 65, no. 1, pp. 155–162, 2001.

[77] O. H. Yeoh, "Some forms of the strain energy function for rubber," *Rubber Chemistry and technology*, vol. 66, no. 5, pp. 754–771, 1993.

[78] I. Abaqus, "Abaqus documentation," *Version*, vol. 6, pp. 1–5, 2014.

[79] K. E. Parsopoulos, M. N. Vrahatis, *et al.*, "Particle swarm optimization method for constrained optimization problems," *Intelligent Technologies–Theory and Application: New Trends in Intelligent Technologies*, vol. 76, no. 1, pp. 214–220, 2002.

[80] R. Poli, J. Kennedy, and T. Blackwell, "Particle swarm optimization," *Swarm intelligence*, vol. 1, no. 1, pp. 33–57, 2007.

[81] R. C. Eberhart and Y. Shi, "Comparing inertia weights and constriction factors in particle swarm optimization," in *Proceedings of the 2000 congress on evolutionary computation. CEC00 (Cat. No. 00TH8512)*, vol. 1, pp. 84–88, IEEE, 2000.

[82] K.-L. Du and M. Swamy, "Search and optimization by metaheuristics," *Techniques and Algorithms Inspired by Nature; Birkhauser: Basel, Switzerland*, 2016.

[83] E. Jones, T. Oliphant, P. Peterson, *et al.*, "SciPy: Open source scientific tools for Python," 2001.

[84] M. Toma, R. Chan-Akeley, C. Lipari, and S.-H. Kuo, "Mechanism of coup and contrecoup injuries induced by a knock-out punch," *Mathematical and Computational Applications*, vol. 25, no. 2, p. 22, 2020.

[85] F. A. Fernandes, R. J. Alves de Sousa, M. Ptak, and J. Wilhelm, "Certified motorcycle helmets: Computational evaluation of the efficacy of standard requirements with finite element models," *Mathematical and Computational Applications*, vol. 25, no. 1, p. 12, 2020.

[86] M. Ghajari, P. J. Hellyer, and D. J. Sharp, "Computational modelling of traumatic brain injury predicts the location of chronic traumatic encephalopathy pathology," *Brain*, vol. 140, no. 2, pp. 333–343, 2017.

[87] C. Bastien, C. Neal-Sturgess, H. Davies, and X. Cheng, "Computing brain white and grey matter injury severity in a traumatic fall," *Mathematical and Computational Applications*, vol. 25, no. 3, p. 61, 2020.

[88] F. Velardi, F. Fraternali, and M. Angelillo, "Anisotropic constitutive equations and experimental tensile behavior of brain tissue," *Biomechanics and modeling in mechanobiology*, vol. 5, no. 1, pp. 53–61, 2006.

[89] S. Budday, R. Nay, R. de Rooij, P. Steinmann, T. Wyrobek, T. C. Ovaert, and E. Kuhl, "Mechanical properties of gray and white matter brain tissue by indentation," *Journal of the mechanical behavior of biomedical materials*, vol. 46, pp. 318–330, 2015.

[90] K. Miller, K. Chinzei, G. Orssengo, and P. Bednarz, "Mechanical properties of brain tissue in-vivo: experiment and computer simulation," *Journal of biomechanics*, vol. 33, no. 11, pp. 1369–1376, 2000.

[91] M. Hosseini-Farid, A. Rezaei, A. Eslaminejad, M. Ramzanpour, M. Ziejewski, and G. Karami, "Instantaneous and equilibrium responses of the brain tissue by stress relaxation and quasi-linear viscoelasticity theory," *Scientia Iranica*, vol. 26, 04 2019.

[92] D. H. Smith, D. F. Meaney, and W. H. Shull, "Diffuse axonal injury in head trauma," *The Journal of head trauma rehabilitation*, vol. 18, no. 4, pp. 307–316, 2003.

[93] J. M. Meythaler, J. D. Peduzzi, E. Eleftheriou, and T. A. Novack, "Current concepts: diffuse axonal injury–associated traumatic brain injury," *Archives of physical medicine and rehabilitation*, vol. 82, no. 10, pp. 1461–1471, 2001.

[94] D. Laskowitz and G. Grant, *Translational research in traumatic brain injury*, vol. 57. CRC Press, 2016.

[95] T. A. Gennarelli, L. E. Thibault, J. H. Adams, D. I. Graham, C. J. Thompson, and R. P. Marcincin, "Diffuse axonal injury and traumatic coma in the primate," *Annals of Neurology: Official Journal of the American Neurological Association and the Child Neurology Society*, vol. 12, no. 6, pp. 564–574, 1982.

[96] M. R. Garnich and G. Karami, "Localized fiber waviness and implications for failure in unidirectional composites," *Journal of composite materials*, vol. 39, no. 14, pp. 1225–1245, 2005.

[97] G. Karami and M. Garnich, "Effective moduli and failure considerations for composites with periodic fiber waviness," *Composite Structures*, vol. 67, no. 4, pp. 461–475, 2005.

[98] K. B. Arbogast and S. S. Margulies, "A fiber-reinforced composite model of the viscoelastic behavior of the brainstem in shear," *Journal of biomechanics*, vol. 32, no. 8, pp. 865–870, 1999.

[99] N. Abolfathi, A. Naik, M. Sotudeh Chafi, G. Karami, and M. Ziejewski, "A micromechanical procedure for modelling the anisotropic mechanical properties of brain white matter," *Computer Methods in Biomechanics and Biomedical Engineering*, vol. 12, no. 3, pp. 249–262, 2009.

[100] G. Karami, N. Grundman, N. Abolfathi, A. Naik, and M. Ziejewski, "A micromechanical hyperelastic modeling of brain white matter under large deformation," *Journal of the mechanical behavior of biomedical materials*, vol. 2, no. 3, pp. 243–254, 2009.

[101] D. Simon, *Evolutionary optimization algorithms*. John Wiley & Sons, 2013.

[102] R. de Rooij and E. Kuhl, "Constitutive modeling of brain tissue: current perspectives," *Applied Mechanics Reviews*, vol. 68, no. 1, p. 010801, 2016.

[103] M. T. Prange and S. S. Margulies, "Regional, directional, and age-dependent properties of the brain undergoing large deformation," *Journal of biomechanical engineering*, vol. 124, no. 2, pp. 244–252, 2002.

[104] T. Ritto and L. Nunes, "Bayesian model selection of hyperelastic models for simple and pure shear at large deformations," *Computers & Structures*, vol. 156, pp. 101–109, 2015.

[105] J. C. Lagarias, J. A. Reeds, M. H. Wright, and P. E. Wright, "Convergence properties of the nelder–mead simplex method in low dimensions," *SIAM Journal on optimization*, vol. 9, no. 1, pp. 112–147, 1998.

[106] X. Jin, F. Zhu, H. Mao, M. Shen, and K. H. Yang, "A comprehensive experimental study on material properties of human brain tissue," *Journal of biomechanics*, vol. 46, no. 16, pp. 2795–2801, 2013.

[107] B. Rashid, M. Destrade, and M. D. Gilchrist, "Mechanical characterization of brain tissue in tension at dynamic strain rates," *Journal of the mechanical behavior of biomedical materials*, vol. 33, pp. 43–54, 2014.

[108] S. A. Yousefsani, A. Shamloo, and F. Farahmand, "Nonlinear mechanics of soft composites: hyperelastic characterization of white matter tissue components," *Biomechanics and Modeling in Mechanobiology*, pp. 1–11, 2019.

[109] J. A. Langlois, W. Rutland-Brown, and M. M. Wald, "The epidemiology and impact of traumatic brain injury: a brief overview," *The Journal of head trauma rehabilitation*, vol. 21, no. 5, pp. 375–378, 2006.

[110] M. Ratajczak, M. Ptak, L. Chybowski, K. Gawdzińska, and R. Będziński, "Material and structural modeling aspects of brain tissue deformation under dynamic loads," *Materials*, vol. 12, no. 2, p. 271, 2019.

[111] K. Arfanakis, V. M. Haughton, J. D. Carew, B. P. Rogers, R. J. Dempsey, and M. E. Meyerand, "Diffusion tensor mr imaging in diffuse axonal injury," *American Journal of Neuroradiology*, vol. 23, no. 5, pp. 794–802, 2002.

[112] N. B. Topal, B. Hakyemez, C. Erdogan, M. Bulut, O. Koksal, S. Akkose, S. Dogan, M. Parlak, H. Ozguc, and E. Korfali, "MR imaging in the detection of diffuse axonal injury with mild traumatic brain injury," *Neurological research*, vol. 30, no. 9, pp. 974–978, 2008.

[113] T. El Sayed, A. Mota, F. Fraternali, and M. Ortiz, "Biomechanics of traumatic brain injury," *Computer Methods in Applied Mechanics and Engineering*, vol. 197, no. 51-52, pp. 4692–4701, 2008.

[114] M. H. Farid, M. Ramzanpour, A. Eslaminejad, M. Ziejewski, and G. Karami, "Computational simulation of brain injury by golf ball impacts in adult and children," *brain*, vol. 13, p. 16, 2018.

[115] A. Rezaei, M. Salimi Jazi, and G. Karami, "Computational modeling of human head under blast in confined and open spaces: primary blast injury," *International journal for numerical methods in biomedical engineering*, vol. 30, no. 1, pp. 69–82, 2014.

[116] P. A. Taylor and C. C. Ford, "Simulation of blast-induced early-time intracranial wave physics leading to traumatic brain injury," *Journal of biomechanical engineering*, vol. 131, no. 6, 2009.

[117] Y. Feng, Y. Gao, T. Wang, L. Tao, S. Qiu, and X. Zhao, "A longitudinal study of the mechanical properties of injured brain tissue in a mouse model," *Journal of the mechanical behavior of biomedical materials*, vol. 71, pp. 407–415, 2017.

[118] S. Qiu, W. Jiang, M. S. Alam, S. Chen, C. Lai, T. Wang, X. Li, J. Liu, M. Gao, Y. Tang, *et al.*, "Viscoelastic characterization of injured brain tissue after controlled cortical impact (CCI) using a mouse model," *Journal of neuroscience methods*, vol. 330, p. 108463, 2020.

[119] Y. Feng, C.-H. Lee, L. Sun, S. Ji, and X. Zhao, "Characterizing white matter tissue in large strain via asymmetric indentation and inverse finite element modeling," *Journal of the mechanical behavior of biomedical materials*, vol. 65, pp. 490–501, 2017.

[120] G. Limbert and J. Middleton, "A transversely isotropic viscohyperelastic material: Application to the modeling of biological soft connective tissues," *International Journal of Solids and Structures*, vol. 41, no. 15, pp. 4237–4260, 2004.

[121] M. R. Garnich and G. Karami, "Finite element micromechanics for stiffness and strength of wavy fiber composites," *Journal of Composite Materials*, vol. 38, no. 4, pp. 273–292, 2004.

[122] G. Karami and M. Garnich, "Micromechanical study of thermoelastic behavior of composites with periodic fiber waviness," *Composites Part B: Engineering*, vol. 36, no. 3, pp. 241–248, 2005.

[123] D. M. Ebenstein and L. A. Pruitt, "Nanoindentation of biological materials," *Nano Today*, vol. 1, no. 3, pp. 26–33, 2006.

[124] M. Radmacher, "Measuring the elastic properties of biological samples with the AFM," *IEEE Engineering in Medicine and Biology Magazine*, vol. 16, no. 2, pp. 47–57, 1997.

[125] Q. Liu, J. Liu, F. Guan, X. Han, L. Cao, and K. Shan, "Identification of the visco-hyperelastic properties of brain white matter based on the combination of inverse method and experiment," *Medical & biological engineering & computing*, vol. 57, no. 5, pp. 1109–1120, 2019.

[126] A. Naik, N. Abolfathi, G. Karami, and M. Ziejewski, "Micromechanical viscoelastic characterization of fibrous composites," *Journal of composite materials*, vol. 42, no. 12, pp. 1179–1204, 2008.

[127] N. Abolfathi, A. Naik, G. Karami, and C. Ulven, "A micromechanical characterization of angular bidirectional fibrous composites," *Computational materials science*, vol. 43, no. 4, pp. 1193–1206, 2008.

[128] L. M. Rios and N. V. Sahinidis, "Derivative-free optimization: a review of algorithms and comparison of software implementations," *Journal of Global Optimization*, vol. 56, no. 3, pp. 1247–1293, 2013.

[129] S. R. Alimo, P. Beyhaghi, and T. R. Bewley, "Delaunay-based global optimization in non-convex domains defined by hidden constraints," in *Evolutionary and Deterministic Methods for Design Optimization and Control With Applications to Industrial and Societal Problems*, pp. 261–271, Springer, 2019.

[130] S. R. Alimo, P. Beyhaghi, and T. R. Bewley, "Optimization combining derivative-free global exploration with derivative-based local refinement," in *2017 IEEE 56th Annual Conference on Decision and Control (CDC)*, pp. 2531–2538, IEEE, 2017.

[131] R. Eberhart and J. Kennedy, "Particle swarm optimization," in *Proceedings of the IEEE international conference on neural networks*, vol. 4, pp. 1942–1948, Citeseer, 1995.

[132] S. A. Kruse, G. H. Rose, K. J. Glaser, A. Manduca, J. P. Felmlee, C. R. Jack Jr, and R. L. Ehman, "Magnetic resonance elastography of the brain," *Neuroimage*, vol. 39, no. 1, pp. 231–237, 2008.

[133] M. Yin, J. A. Talwalkar, K. J. Glaser, A. Manduca, R. C. Grimm, P. J. Rossman, J. L. Fidler, and R. L. Ehman, "Assessment of hepatic fibrosis with magnetic resonance elastography," *Clinical Gastroenterology and Hepatology*, vol. 5, no. 10, pp. 1207–1213, 2007.

[134] J. Braun, K. Braun, and I. Sack, "Electromagnetic actuator for generating variably oriented shear waves in MR elastography," *Magnetic Resonance in Medicine: An Official Journal of the International Society for Magnetic Resonance in Medicine*, vol. 50, no. 1, pp. 220–222, 2003.

[135] J. B. Weaver, A. J. Pattison, M. D. McGarry, I. M. Perreard, J. G. Swienckowski, C. J. Eskey, S. S. Lollis, and K. D. Paulsen, "Brain mechanical property measurement using MRE with intrinsic activation," *Physics in Medicine & Biology*, vol. 57, no. 22, p. 7275, 2012.

[136] J. Guo, S. Hirsch, K. Streitberger, C. Kamphues, P. Asbach, J. Braun, and I. Sack, "Patient-activated three-dimensional multifrequency magnetic resonance elastography for high-resolution mechanical imaging of the liver and spleen," in *RöFo-Fortschritte auf dem Gebiet der Röntgenstrahlen und der bildgebenden Verfahren*, vol. 186, pp. 260–266, © Georg Thieme Verlag KG, 2014.

[137] J. Greenleaf, R. Muthupillai, P. Rossman, J. Smith, A. Manduca, and R. Ehman, "Direct visualization of strain waves by magnetic resonance elastography (mre)," in *1996 IEEE Ultrasonics Symposium. Proceedings*, vol. 1, pp. 467–472, IEEE, 1996.

[138] L. V. Hiscox, C. L. Johnson, E. Barnhill, M. D. McGarry, J. Huston 3rd, E. J. Van Beek, J. M. Starr, and N. Roberts, "Magnetic resonance elastography (MRE) of the human brain: technique, findings and clinical applications," *Physics in Medicine & Biology*, vol. 61, no. 24, p. R401, 2016.

[139] D. Klatt, C. Friedrich, Y. Korth, R. Vogt, J. Braun, and I. Sack, "Viscoelastic properties of liver measured by oscillatory rheometry and multifrequency magnetic resonance elastography," *Biorheology*, vol. 47, no. 2, pp. 133–141, 2010.

[140] S. K. Venkatesh, M. Yin, and R. L. Ehman, "Magnetic resonance elastography of liver: clinical applications," *Journal of computer assisted tomography*, vol. 37, no. 6, p. 887, 2013.

[141] S. K. Venkatesh, M. Yin, J. F. Glockner, N. Takahashi, P. A. Araoz, J. A. Talwalkar, and R. L. Ehman, "MR elastography of liver tumors: preliminary results," *American Journal of Roentgenology*, vol. 190, no. 6, pp. 1534–1540, 2008.

[142] J. Chen, H. McGregor, K. Glaser, Y. Mariappan, A. Kolipaka, and R. Ehman, "Magnetic resonance elastography in trabecular bone: preliminary results," in *Proceedings 17th Scientific Meeting, International Society for Magnetic Resonance in Medicine*, p. 847, 2009.

[143] J. Schmidt, D. Tweten, A. Badachhape, A. Reiter, R. Okamoto, J. Garbow, and P. Bayly, "Measurement of anisotropic mechanical properties in porcine brain white matter ex vivo using magnetic resonance elastography," *Journal of the mechanical behavior of biomedical materials*, vol. 79, pp. 30–37, 2018.

[144] M. McGarry, C. Johnson, B. Sutton, J. Georgiadis, E. Van Houten, A. Pattison, J. Weaver, and K. Paulsen, "Suitability of poroelastic and viscoelastic mechanical models for high and low frequency MR elastography," *Medical physics*, vol. 42, no. 2, pp. 947–957, 2015.

[145] P. R. Perriñez, F. E. Kennedy, E. E. Van Houten, J. B. Weaver, and K. D. Paulsen, "Modeling of soft poroelastic tissue in time-harmonic MR elastography," *IEEE transactions on biomedical engineering*, vol. 56, no. 3, pp. 598–608, 2008.

[146] G. E. Leclerc, L. Debernard, F. Foucart, L. Robert, K. M. Pelletier, F. Charleux, R. Ehman, M.-C. H. B. Tho, and S. F. Bensamoun, "Characterization of a hyper-viscoelastic phantom mimicking biological soft tissue using an abdominal pneumatic driver with magnetic resonance elastography (MRE)," *Journal of biomechanics*, vol. 45, no. 6, pp. 952–957, 2012.

[147] Q. Chen, S. I. Ringleb, A. Manduca, R. L. Ehman, and K.-N. An, "Differential effects of pre-tension on shear wave propagation in elastic media with different boundary conditions

as measured by magnetic resonance elastography and finite element modeling," *Journal of biomechanics*, vol. 39, no. 8, pp. 1428–1434, 2006.

[148] M. C. Murphy, J. Huston, K. J. Glaser, A. Manduca, F. B. Meyer, G. Lanzino, J. M. Morris, J. P. Felmlee, and R. L. Ehman, "Preoperative assessment of meningioma stiffness using magnetic resonance elastography," *Journal of neurosurgery*, vol. 118, no. 3, pp. 643–648, 2013.

[149] L. Liang, M. Liu, C. Martin, and W. Sun, "A deep learning approach to estimate stress distribution: a fast and accurate surrogate of finite-element analysis," *Journal of The Royal Society Interface*, vol. 15, no. 138, p. 20170844, 2018.

[150] M. C. Murphy, A. Manduca, J. D. Trzasko, K. J. Glaser, J. Huston III, and R. L. Ehman, "Artificial neural networks for stiffness estimation in magnetic resonance elastography," *Magnetic resonance in medicine*, vol. 80, no. 1, pp. 351–360, 2018.

[151] J. M. Scott, A. Arani, A. Manduca, K. P. McGee, J. D. Trzasko, J. Huston III, R. L. Ehman, and M. C. Murphy, "Artificial neural networks for magnetic resonance elastography stiffness estimation in inhomogeneous materials," *Medical Image Analysis*, vol. 63, p. 101710, 2020.

[152] C. Lanczos, *An iteration method for the solution of the eigenvalue problem of linear differential and integral operators*. United States Governm. Press Office Los Angeles, CA, 1950.

[153] T. Hastie, R. Tibshirani, and J. Friedman, "The elements of statistical learning. Springer series in statistics," Springer, 2001.

[154] C. M. Bishop, *Pattern recognition and machine learning*. springer, 2006.

[155] S. Albawi, T. A. Mohammed, and S. Al-Zawi, "Understanding of a convolutional neural network," in *2017 International Conference on Engineering and Technology (ICET)*, pp. 1–6, IEEE, 2017.

[156] N. Aloysius and M. Geetha, "A review on deep convolutional neural networks," in *2017 International Conference on Communication and Signal Processing (ICCSP)*, pp. 0588–0592, IEEE, 2017.

[157] I. Goodfellow, Y. Bengio, A. Courville, and Y. Bengio, *Deep learning*, vol. 1. MIT press Cambridge, 2016.

[158] R. Wang and M. Sarntinoranont, "Biphasic analysis of rat brain slices under creep indentation shows nonlinear tension-compression behavior," *Journal of the mechanical behavior of biomedical materials*, vol. 89, pp. 1–8, 2019.